

Håkon Frydenberg  
Magnus Pjaaka Torp

# Impact on polymer-coated pipelines

Master's thesis in Mechanical Engineering

Supervisor: Tore Børvik

June 2020

**NTNU**  
Norwegian University of Science and Technology  
Faculty of Engineering  
Department of Structural Engineering



Norwegian University of  
Science and Technology





## MASTER'S THESIS 2020

SUBJECT AREA: Computational mechanics	DATE: 04.06.2020	NO. OF PAGES: 14 + 78 + 21
--	---------------------	-------------------------------

TITLE: **Impact on polymer-coated pipelines**  
Støt mot rørledninger med isolasjonslag av polymer

BY:

Håkon Frydenberg  
Magnus Pjaaka Torp



### SUMMARY:

This master's thesis presents an experimental and numerical investigation into the structural integrity of polymer-coated subsea pipelines. The objective was to find out how a porous polyurethane-coated subsea pipeline behaves when being subjected to quasi-static impact loading. This is part of an ongoing research collaboration between SIMLab at NTNU and Equinor, where impact loads on coated subsea pipelines are of interest.

Material properties of the steel and porous polyurethane (PU) were obtained by material experiments. Uniaxial tensile tests of the steel were conducted to verify the steel quality to be of grade X65, while uniaxial compression tests were performed on PU specimens. The PU was observed to be brittle during testing. X-ray micro-computed tomography mapped a variation of the relative density in the PU coating in the radial direction of the pipeline.

A component test was conducted by quasi-static denting of two pipeline sections at 1m each with two different indenter geometries. It was observed that the PU coating absorbs 18kJ and 11kJ of the work done by the big and small indenter, respectively, prior to permanent deformation of the steel pipe. A brief comparison of PP- and PU-coated pipeline designs is conducted, where the latter absorbs less energy in the coating.

The calibration of material models was established based on experimental results and previous research carried out at NTNU. A Johnson-Cook power law was applied to the steel, while true stress versus true strain relationship for the PU coating was obtained. This relationship was modified to fit the crushable foam material model (Deshpande and Fleck) in Abaqus/Explicit and softened to represent the extensive fracturing observed during experiments.

All experiments were numerically simulated in Abaqus/Explicit to validate and verify material models. Special attention was given to the PU coating and the component test. The coating layer in the component model was divided into 4 layers with different mechanical properties depending on the relative density. No fracture criteria were applied, although fracture was seen in the coating during the experiments. The numerical simulations yielded good results. Finally, a parameter study where the boundary conditions were changed in the numerical model was conducted to see the effects on the pipeline response with more realistic boundary conditions.

RESPONSIBLE TEACHER: Tore Børvik

SUPERVISOR(S): Tore Børvik, Ole Vestrum and Martin Kristoffersen

CARRIED OUT AT: Structural Impact Laboratory (SIMLab), Department of Structural Engineering, Norwegian University of Science and Technology (NTNU)







## MASTEROPPGAVE 2020

FAGOMRÅDE: Beregningsmekanikk	DATO: 04.06.2020	ANTALL SIDER: 14 + 78 + 21
----------------------------------	---------------------	-------------------------------

TITTEL: <b>Støt på rørledninger med isolasjonslag av polymer</b> Impact on polymer-coated pipelines	
UTFØRT AV: Håkon Frydenberg Magnus Pjaaka Torp	

<p><b>SAMMENDRAG:</b></p> <p>Denne masteroppgaven inneholder en eksperimentell og numerisk undersøkelse av den mekaniske styrken til undersjøiske rørledninger med isolasjonslag av polymer. Målet med oppgaven var å finne ut hvordan undersjøiske rørledninger med porøst polyuretan responderer under kvasi-statisk last. Dette arbeidet er en del av et forskningssamarbeid mellom SIMLab på NTNU og Equinor, der støt mot isolerte rørledninger er fokus.</p> <p>Materialeegenskaper for stål og porøst polyuretan (PU) ble bestemt fra eksperimenter. Strekktester av stålet ble gjennomført for å verifisere at stålet hadde stålqualität X65. Trykkprøver ble gjennomført på PU testprøver. Under trykkprøvene ble det observert at porøst PU var et sprøtt materiale. Røntgen mikro-computertomografi viste en variasjon av relativ tetthet i radiell retning i røret.</p> <p>En komponenttest ble gjennomført ved kvasi-statisk inntrykking av to rørledninger på 1m med to forskjellige inntrykkingskniver. Det ble observert at PU-isolasjonen absorberte 18kJ og 11kJ av arbeid utført av henholdsvis stor og liten inntrykkingskniv før noe permanent deformasjon var synlig i stålrøret. En kort sammenlikning av PP- og PU-isolerte rør ble utført, der PU-isolasjonen absorberer mindre energi.</p> <p>Kalibrering av materialmodeller ble gjort basert på eksperimenter og tidligere forskning ved NTNU. En Johnson-Cook material modell ble brukt på stålet, og sann spenning mot sann tøyning ble etablert for PU-isolasjonen. For PU ble disse verdiene modifisert til å passe inn i materialmodellen crushable foam (Deshpande and Fleck) i Abaqus, samt gjort responsen mykere for å ta hensyn til brudd som ikke har blitt kalibrert.</p> <p>Alle eksperimenter ble simulert for å verifisere materialmodellene. Trykktesten av PU-isolasjonen og komponenttesten ble grundigere undersøkt. Isolasjonslaget i røret ble delt opp i 4 lag med forskjellige materialeegenskaper avhengig av relativ tetthet. Det har ikke blitt brukt noe bruddkriterie i Abaqus, selv om dette ble observert i isolasjonslagene i eksperimentene. De numeriske analysene ga gode resultater. Til slutt ble en numerisk grensetilstandsanalyse (BC) utført for å undersøke endringer i responsen ved inntrykking av røret med mer realistiske BCs.</p>
--

FAGLÆRER: Tore Børvik
VEILEDER(E): Tore Børvik, Ole Vestrum og Martin Kristoffersen
UTFØRT VED: Structural Impact Laboratory (SIMLab), Institutt for konstruksjonsteknikk, Norges teknisk-naturvitenskapelige universitet (NTNU)



## **MASTER'S THESIS 2020**

for

*Håkon Frydenberg and Magnus Pjaaka Torp*

### **Impact on polymer-coated pipelines**

#### **1. INTRODUCTION**

Subsea steel pipelines are used by the offshore industry to transport oil and gas along the seabed. To protect the steel pipes from the harsh operational environment, polymeric coating solutions are often applied as anti-corrosion and thermal insulation. In addition to threats posed by the ambient seawater environment, pipelines are also exposed to the risk of impact from fishing trawls or anchors. Thus, pipelines must also be designed to sustain possible impact events. While not primarily intended for it, the coating solutions are experienced to contribute to the structural integrity of the pipeline. However, the complex material properties of these coatings complicate their adaptation into standard numerical frameworks.

In this master's thesis, offshore steel pipes with polyurethane coating will be investigated under quasi-static impact loading. The main intention is to identify potential difference in behaviour between polyurethane and polypropylene-coated pipelines. Further, material testing, with a special focus on the coating material, will be conducted. This will be done in conjunction with X-ray micro-computed tomography (XRMCT) and advanced numerical simulations. Accurate numerical models will be an invaluable aid when predicting the mechanical response of the coated pipeline during an impact event.

#### **2. OBJECTIVES**

The main objectives of the research project are to determine how polyurethane-coated pipelines behave under quasi-static impact loading and to validate to which extent this can be predicted using computational tools.

#### **3. A SHORT DESCRIPTION OF THE RESEARCH PROJECT**

The main topics in the research project will be as follows;

1. A comprehensive literature review on impact on coated pipelines, with a special focus on the behaviour of the steel pipe and coating material, shall be conducted.
2. Material test coupons from the coating material will be tested in uniaxial compression. Before testing, X-ray micro-computed tomography (XRMCT) will be performed to reveal the relative density variation of the porous coating material.
3. Non-linear FE numerical simulations of the porous coating will be performed, and the numerical results shall be compared and discussed towards the experimental observations.
4. Parametric studies, with a special focus on realistic impact scenarios, shall be carried out.

*Supervisors:* Tore Børvik, Ole Vestrum and Martin Kristoffersen.

The thesis must be written according to current requirements and submitted to the Department of Structural Engineering, NTNU, no later than June 10<sup>th</sup>, 2020.

NTNU, January 15<sup>th</sup>, 2020

Tore Børvik  
Professor



# Acknowledgement

Our supervisors have been Professor Tore Børvik, Dr. Ole Vestrum and Dr. Martin Kristoffersen. Their good humour and enthusiasm for the research, along with guidance throughout the project have been of great importance and is much appreciated.

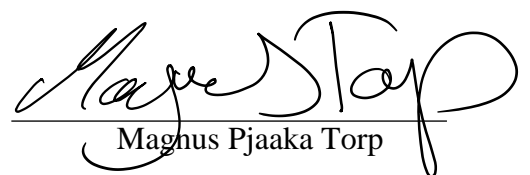
The experimental work has been carried out by the dedicated and very helpful laboratory staff at both the Department of Structural Engineering at NTNU and SINTEF. We want to give a special thanks to Tore Wiseth for his helpfulness and patience in the laboratory. Tore Kristensen at SINTEF has also contributed with valuable testing of the steel and polymer coating. We also want to thank Ole Tore Buset for his help on conducting the XRMCT scans, which has been of great help in understanding the coating material.

We wish to thank NTNU and SIMLab in collaboration with Equinor, for the opportunity to conduct the invaluable and enlightening experiments on the pipeline.

Finally, thanks to all the master students at the Department of Structural Engineering for a helpful and fun working environment.

Trondheim, June 4<sup>th</sup>, 2020

  
Håkon Frydenberg

  
Magnus Pjaaka Torp



## Abstract

This master's thesis presents an experimental and numerical investigation into the structural integrity of polymer-coated subsea pipelines. The objective was to find out how a porous polyurethane-coated subsea pipeline behaves when being subjected to quasi-static impact loading. This is part of an ongoing research collaboration between SIMLab at NTNU and Equinor, where impact loads on coated subsea pipelines are of interest.

Material properties of the steel and porous polyurethane (PU) were obtained by material experiments. Uniaxial tensile tests of the steel were conducted to verify the steel quality to be of grade X65, while uniaxial compression tests were performed on PU specimens. The PU was observed to be brittle during testing. X-ray micro-computed tomography mapped a variation of the relative density in the PU coating in the radial direction of the pipeline.

A component test was conducted by quasi-static denting of two pipeline sections at 1m each with two different indenter geometries. It was observed that the PU coating absorbs 18kJ and 11kJ of the work done by the big and small indenter, respectively, prior to permanent deformation of the steel pipe. A brief comparison of PP- and PU-coated pipeline designs is conducted, where the latter absorbs less energy in the coating.

The calibration of material models was established based on experimental results and previous research carried out at NTNU. A Johnson-Cook power law was applied to the steel, while true stress versus true strain relationship for the PU coating was obtained. This relationship was modified to fit the crushable foam material model (Deshpande and Fleck) in Abaqus/Explicit and softened to represent the extensive fracturing observed during experiments.

All experiments were numerically simulated in Abaqus/Explicit to validate and verify material models. Special attention was given to the PU coating and the component test. The coating layer in the component model was divided into 4 layers with different mechanical properties depending on the relative density. No fracture criteria were applied, although fracture was seen in the coating during the experiments. The numerical simulations yielded good results. Finally, a parameter study where the boundary conditions were changed in the numerical model was conducted to see the effects on the pipeline response with more realistic boundary conditions.





# Contents

Notation .....	xiii
<b>1 Introduction .....</b>	<b>1</b>
1.1 Background and motivation.....	1
1.2 State of the art.....	2
1.3 Objective.....	5
1.4 Scope .....	5
1.5 Outline of thesis.....	6
<b>2 Experimental setups .....</b>	<b>7</b>
2.1 Introduction .....	7
2.2 Material specimen description.....	9
2.3 X-ray micro-computed tomography setup.....	10
2.4 Steel experimental setup.....	10
2.5 Uniaxial compression setup.....	11
2.5.1 Material specimen test .....	12
2.5.2 Sandwich sample test.....	12
2.6 Quasi-static denting of pipe setup .....	12
<b>3 Experimental results .....</b>	<b>15</b>
3.1 Strain measure .....	15
3.2 X-ray micro-computed tomography results.....	16
3.3 Uniaxial tension test results .....	20
3.4 Uniaxial compression test results .....	21
3.4.1 eCorr Digital Image Correlation.....	21
3.4.2 Material specimen results .....	22
3.4.3 Sandwich sample results.....	26
3.5 Quasi-static denting of pipe results .....	28
3.5.1 The absorbed energy of the pipes .....	31
3.6 Comparing PU and PP results .....	34
<b>4 Calibration of material models.....</b>	<b>37</b>
4.1 Formulation .....	37
4.1.1 Constitutive relation of steel.....	38
4.1.2 Constitutive relation of polyurethane .....	39
4.2 Finite element analysis theory .....	41
4.3 Calibration of steel material model .....	42
4.4 Calibration of the polyurethane material model .....	44

4.4.1 Numerical model geometry .....	44
4.4.2 Polyurethane material model .....	45
4.4.3 Softening of the material model .....	47
4.4.4 Sensitivity study .....	48
<b>5 Numerical study .....</b>	<b>51</b>
5.1 Polypropylene material model .....	51
5.2 Numerical analysis of the sandwich specimen .....	52
5.3 Numerical analysis of the pipe .....	54
5.3.1 Numerical analysis with the big indenter .....	54
5.3.2 Numerical analysis with the small indenter .....	57
5.3.3 Accuracy of the numerical models .....	60
5.4 Coating partitioning study .....	61
5.5 Boundary condition study .....	62
<b>6 Discussion .....</b>	<b>67</b>
<b>7 Concluding remarks .....</b>	<b>71</b>
7.1 Conclusions .....	71
7.1.1 Investigation of the materials indicated that: .....	71
7.1.2 Experimental denting of pipe .....	72
7.1.3 Numerical denting of pipe .....	72
7.2 Recommendations for further work .....	72
<b>Bibliography .....</b>	<b>73</b>
<b>Appendix .....</b>	<b>I</b>
A. Figures .....	I
B. Measures .....	IX
C. Tables .....	XI
D. Theory .....	XII
E. Datasheets .....	XIV

# Notation

## Abbreviations

1D	One-dimensional
2D	Two-dimensional
3D	Three-dimensional
BL	Bridgman-LeRoy
BC	Boundary condition
C3D8I	Cubic 3D element, eight nodes, incompatible mode
C3D8R	Cubic 3D element, eight nodes, reduced integration
CAX4R	Linear, axisymmetric stress element, reduced integration
DF	Deshpande and Fleck
DIC	Digital Image Correlation
FEA	Finite Element Analysis
FEM	Finite Element Method
JC	Johnson-Cook
PP	Polypropylene
PU	Polyurethane
QS	Quasi-static
UC(T)	Uniaxial compression (test)
UT(T)	Uniaxial tensile (test)
XRMCT	X-ray micro-computed tomography

## Variables

$\sigma_{0.2}$	0.2% offset yield strength
$avg$	Average
$k$	Compression yield stress ratio
$\rho$	Density
$e$	Engineering strain
$s$	Engineering stress
$\sigma_{eq}$	Equivalent stress
$F$	Force
$\mu$	Friction coefficient
$h$	Height
$w_{\theta}$	Hoop width
$\sigma_H$	Hydrostatic stress
$h_0$	Initial height
$L_0$	Initial length
$u_i$	Inner displacement of the steel pipe
$D_1$	Johnson-Cook damage parameter
$L$	Length
$w_z$	Longitudinal width
$u_o$	Outer displacement of the pipe
$\dot{\lambda}$	Plastic multiplier
$\nu_p$	Plastic Poisson's ratio
$p$	Plastic strain
$\nu$	Poisson's ratio
$\alpha$	Pressure sensitivity parameter
$D_{ij}$	Rate-of-deformation tensor
$\bar{\rho}$	Relative density
$\dot{\epsilon}$	Strain-rate
$STD$	Standard deviation
$\sigma_t$	True (Cauchy) stress
$\epsilon_1$	True (logarithmic) strain
$v$	Velocity
$V$	Volume
$W$	Work
$W_{cr}$	Work per volume to fracture
$\epsilon_0$	Yield strain
$\sigma_0$	Yield stress
$E$	Young's Modulus

# Chapter 1

## Introduction

### 1.1 Background and motivation

Subsea pipelines in the offshore industry are used to transport crude oil and natural gas with high pressure and temperature over vast distances. Offshore pipelines are often protected by polymeric coatings with primarily thermal insulation and anti-corrosion intent. Although not intended for it, the coating also contributes to increasing the structural integrity and energy absorption of the pipeline [1, 2, 3]. Pipelines are exposed to accidents by dropped objects [4] and fish trawling gear as subsea installations tend to attract fish [5]. Three scenarios are illustrated in Figure 1.1. In areas with common interests, the offshore petroleum industry is not allowed to restrict nor hinder fishing activities, thus increasing the probability of accidents. Accidents can result in negative environmental effects and huge economical losses, hence the proper design of pipelines with great knowledge of their response to impact loads is necessary.

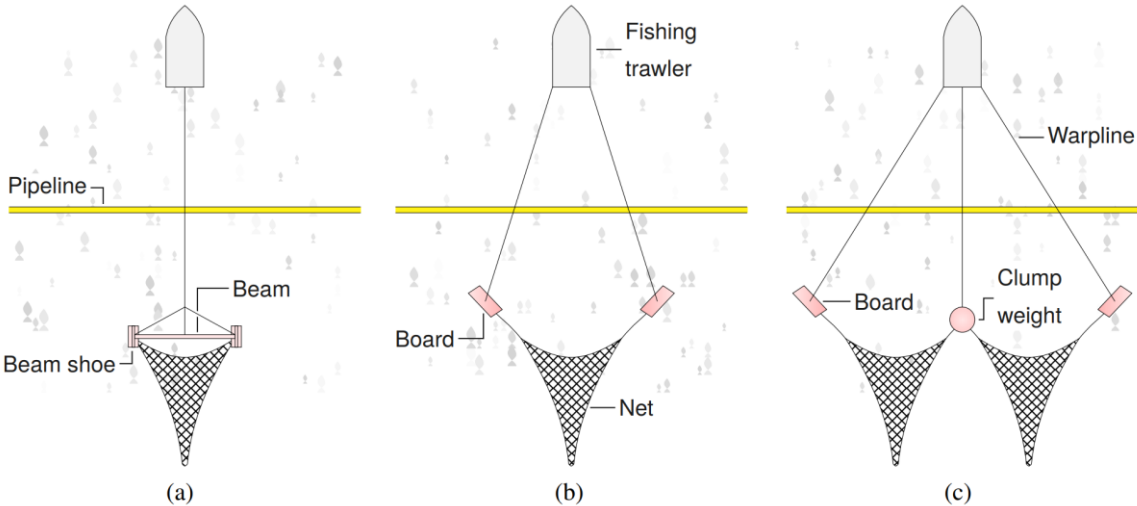


Figure 1.1: Typical fishing trawler gear crossing a pipeline [3].

DNVGL-RP-F111 [5] is a recommended practice by Det Norske Veritas Germanischer Lloyd (DNV GL) where three different interactions between trawling gear and pipelines are defined; impact, pull-over and hooking. The latter interaction scenario is a special case and one extreme incident describing this is the well-known accident that took place in November 2007 at the Kvittebjørn oil field 140km west off the coast of Norway. Here, a subsea pipeline at a water depth of 210 meters transporting gas was impacted and dragged approximately 56 meters from its initial position by an anchor. Equinor had to temporarily stop production until January 2008 [6]. During pressure testing in August 2008, a small leak from the impacted section was discovered which again halted the production. As a result of this incident, a research collaboration between Equinor and SIMLab (Structural Impact Laboratory) at NTNU was established and engaged several master's theses on NTNU regarding impact against both bare steel pipes [7, 8, 9, 10, 11, 12] and two coated steel pipelines [1, 2].

Safety has always been one of the primary focuses of the industry. Offshore pipelines are therefore overly conservative in their structural designs. This means less effective utilization of materials which is not a good solution to the environment and the cost associated with the production of these pipelines. DNV GL in references [5, 13, 14] facilitates for better design solutions and motivates to include mechanical strength from the polymer coating. A polypropylene (PP) coating's mechanical properties have been studied in recent years, and the offshore industry motivates further studies to include other polymers. In this thesis, the study of polyurethane (PU) coating will be the primary focus, along with a comparison to PP coating. To include the coating's strength, it is necessary to prove their contributions through tests and simulations.

To validate material behaviour, pipelines are produced and then tested. This is both an expensive and timely approach, so the industry and researchers are transferring more and more over to numerical modelling. Finite element analysis (FEA) enables faster design processes and dramatically reduce costs associated with experimental testing.

## 1.2 State of the art

The first pipeline in the Norwegian gas transport network was laid in 1977, and in the following years until now, this network has grown along with demand. Gas from this network covers around 25% of gas usage in the EU, and these pipelines add up to a length of 8800km [15, 16]. Globally, offshore pipelines transporting both oil and gas started earlier and add up to enormous lengths. Due to the economic costs and negative environmental effects caused by accidents, many experimental and theoretical studies have been conducted on pipeline impact. Jones et al. [17] did an extensive experimental study on the lateral impact of pressurised, fully clamped mild steel pipes in 1992, both static- and dynamic tests. This work provided a lot of data for theoretical methods of analysis and calibration of numerical finite element schemes. Jones and Birch [18] extended previous studies in 1996 with 54 new impact tests with similar conditions, and defined three failure modes; 1) inelastic deformation; 2) local failure; and 3) global failure mode, see Figure 1.2. In 2010, Jones and Birch published a new article to give a clearer insight into pipeline behaviour, and to provide more rigorous validation on numerical schemes [19].

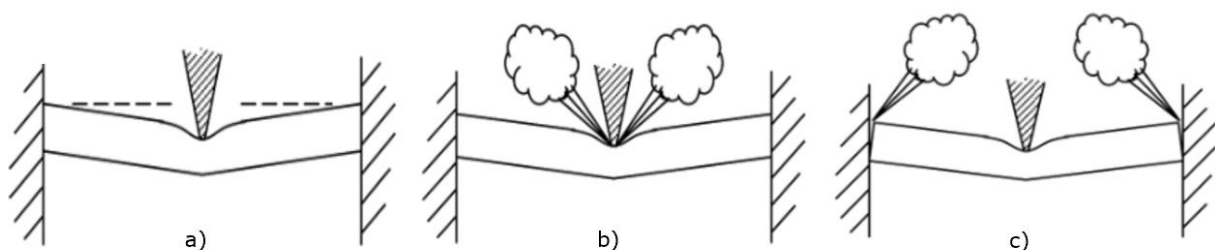


Figure 1.2: Failure modes by Jones and Birch. a) inelastic deformation, b) local failure mode, and c) global failure mode [18].

The study by Shen and Shu in 2002 [20], based on earlier theoretical analysis studies, utilises empirical formulas to estimate the length of a plastic hinge in their theoretical quasi-static analysis to predict the onset of failure for pipelines. Their results are good in comparison with experimental tests, and with the use of FEA programs, the onset of failure can be predicted. Most of the studies on anchor impact on pipes up until Manes et al. in 2012 [21], have been on the first load sequence; namely the propagation from denting until one of the failure modes

defined in [18] occurs. Manes et al. investigated the whole loading sequence as described in DNV GL recommended practices [5] that a pipeline is subjected to; impact, hooking, pullover and pipeline rebound. Simplifications had to be done in this comprehensive study to represent this complex loading sequence. First, a quasi-static three-point bending test was conducted on the pipe to represent the impact, followed by stretching the pipe back into a straight position. Huge axial forces in the pipe occurred when it was dragged out of its straight position, and the latter test represents the work done by this tension force within the pipe. Only one specimen had superficial cracks after the whole loading sequence, thus, these were considered to be of secondary importance in this particular study. The second objective of this study was to validate a numerical model to simulate the entire loading sequence. By using an anisotropic yield criterion, here “Hill” or “Yld91 by Barlat”, in combination with combined isotropic-kinematic hardening was shown to reproduce the experimental results with the best accuracy in both the bending and stretching phase.

An extensive study on seamless X65 steel pipes was conducted by Kristoffersen in his PhD. thesis in 2014 [22]. From material tests in this research, it was reasonable to assume isotropic and homogeneous material behaviour over the cross-section in the steel pipes. Kristoffersen [22] conducted both quasi-static and dynamic tests on empty and water-filled pipes. It was observed from these tests that the material was strain-rate sensitive and that fracture always occurred after subsequent stretching. The finite element simulations conducted on the experiments were in general very accurate. However, the force of the stretching phase in the experiments was overestimated in the numerical model, mainly caused by the fracture being inadequately described. Initiation of fracture happens on a smaller scale than the element size used in the finite element simulation.

A categorisation of materials having low relative densities is of interest, and in Cellular Solids, by Gibson and Ashby in 1997 [23], a material with a relative density below 0.3 is defined as a “true foam”. This limit value reflects a transition for how the pores are represented in the mass. Exceeding 0.3, the material has a solid mass surrounding and isolating pores, and a relative density less than this limit consist of struts and crisp thin walls separating the pores. With this established, Marie et al. [24] defined the term “porous” for materials exceeding the limit value. The coating used outside of steel pipelines are often materials with varying relative densities such that the terms above is adopted herein.

As part of the ongoing research program between SIMLab and Equinor, the mechanical effects by the coating is also of interest. In the master’s thesis by Holm and Røshol in 2015 [1], it was shown that coated pipelines had a significantly lower inner displacement compared to pipes without coating when subjected to load. The coating being researched herein was porous polypropylene (PP) and material models were calibrated from uniaxial compression tests (UCT) done on small coating specimens. Numerical errors occurred in their component simulations (quasi-static denting of coated pipe) due to severe element distortion and contact formulation. This occurred since the calibrated PP in their model is both thicker and weaker than the steel pipe, yielding discontinuity in material properties for the pipe model. A following master’s thesis by Hammersvik and Kulsrud in 2017 [2] investigated the coating material in more detail with the use of X-ray micro-computed tomography (XRMCT) and built up a numerical material model of small coating specimens. The obtained numerical model from the XRMCT is shown

in Figure 1.3a where the green small cubes are solid material. They were able to replicate the material tests with high accuracy with these numerical simulations. However, it should be noted that the numerical model was calibrated to be an isotropic, elastic-plastic material, which is not accurate according to the general theory about polymers [23]. Polymers are often also temperature-, pressure- and strain-rate-sensitive, and in Hammersvik and Kulsrud's thesis [2], the porous polypropylene was also calibrated to be insensitive to this.

An even more thorough study on porous polypropylene-coated steel pipes was conducted by Ole Vestrum and reported in his PhD. thesis [3]. Vestrum intended to establish a framework to build up numerical models using non-destructive analysing methods which should decrease the costs associated with physical testing. This generic modelling approach capture and include the mechanical contributions by the porous polymers during pipeline impact. Both quasi-static and dynamic experiments were conducted on two different cross-sectional sizes of coated and uncoated steel pipelines to validate Vestrum's approach. Based on the weight and velocity described in the relevant guideline DNVGL-RP-F111 [5], the maximum kinetic energy expected from impacting objects is estimated to 40.5kJ. Comparably, approximately 25kJ and 60kJ were dissipated before permanent internal indentation of the steel was recorded in Pipe S (i.e., the smallest pipeline design) and Pipe L (i.e., the largest pipeline design), respectively in Vestrum's experiments. Equivalently, to dissipate 25kJ in the uncoated Pipe S, a permanent indentation of 12% of the internal steel diameter was recorded in the experiments. The numerical simulations of quasi-static denting of pipelines with Vestrum's established generic modelling approach showed promising results, and with an implementation of a simple fracture criterion based on an equivalent strain measure, the results reproduced force versus displacement with high accuracy.

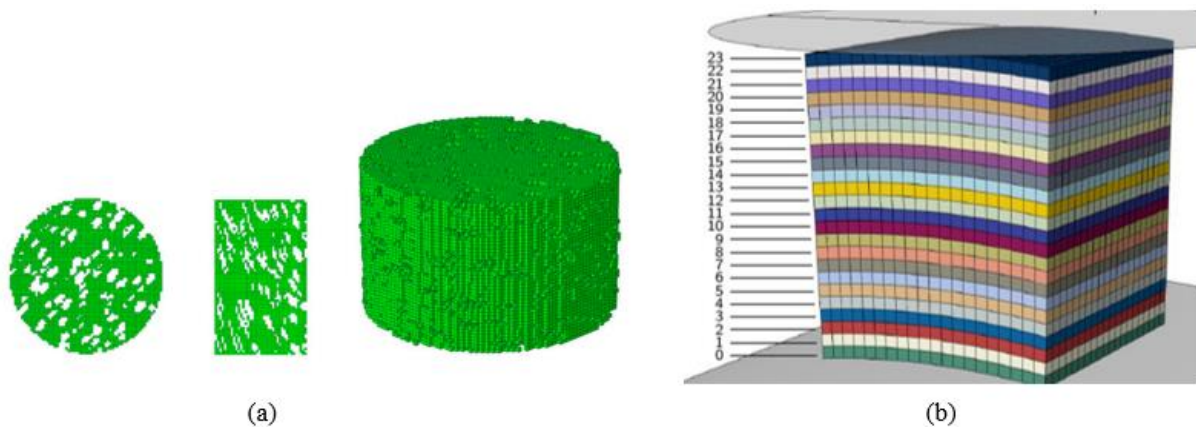


Figure 1.3: Numerical models of (a) porous polypropylene material specimen and (b) coating specimen divided into sublayers [3].

Vestrum [3] utilised Maire and Withers' [25] second method of mesh generation to obtain a numerical model of a polypropylene material specimen (similar to Hammersvik and Kulsrud [2]). This technique uses reconstructed XRMCT images of a volume to generate voxel element mesh in a finite element model program. To reduce the image size, Vestrum both downscaled and binarized the reconstructed XRMCT images before generating mesh in Abaqus. Figure 1.3a shows the numerically generated material specimen while Figure 1.3b is for the whole coating thickness divided into sublayers. The relative density was shown to vary along the thickness direction of the coating, and this variation is one of the main parameters in Vestrum's approach.



Vestrum [3] utilises this variation to section the porous polymer coating into sublayers and then run a numerical limit analysis on unit cells [26] to map the yield strength's dependence on pressure. Vestrum fitted Deshpande and Fleck's yield criterion [27] to describe the yield surface of polypropylene and expressed both the yield stress and pressure sensitivity parameter as a function of porosity. The constitutive model was validated by experimental results conducted by Vestrum [3] and the main trends in force versus displacement curves were obtained. The framework secured satisfying results and will be a good starting point for further studies.

### **1.3 Objective**

The main objective in this research project is to determine how polyurethane-coated pipelines behave under quasi-static (QS) impact loading and to validate to which extent this can be predicted using computational tools.

With the aim of detecting polyurethane's behaviour, three coated pipeline-stubs were delivered by Equinor at approximately 1m in length each, all from the same coated pipeline produced by Logstor in Denmark [28]. In practice, all these pipes are exactly alike with respect to mechanical behaviour. Thus, one of them provided specimens to conduct material testing, while the two others were quasi-statically dented. The mechanical behaviour as the experiments are performed is of interest and will be described along with the coated pipeline's ability to absorb the work done on it.

Deshpande and Fleck's [27] constitutive model will be derived for porous polyurethane from reverse engineering modelling of the experimental data obtained from uniaxial compression tests of small coating specimens. This material model will then be implemented into a numerical model to simulate the quasi-static pipeline impact using Abaqus' finite element software, and then validated with experimental data. Using the established constitutive relation, the numerical model will be extended with a new boundary condition to see if the model can predict other scenarios.

Non-destructive X-ray micro-computed tomography will be conducted before the experiments mentioned above and a mapping of the relative density of the coating is of interest. A study with the aim of mapping the coating's dependency on this relative density will be explored in a numerical study conducted on the pipeline model.

### **1.4 Scope**

Due to the extensive amount of available parameters and branches to investigate regarding impact on coated pipelines, some limitations are imposed in the present study:

- The primary functions of the polymer coating (thermal insulation and anti-corrosion) will not be investigated in this thesis.
- Hypoelastic formulation is used over hyperelastic, and only characteristics along the coating thickness is studied.
- Polymers are in general sensitive to temperature, pressure and strain-rate; however, this will be neglected in the constitutive model used.
- Numerical simulations are restricted to what is commercially available, which affects both the efficiency and accuracy.

- The coated pipeline will be assumed to be initially free from all loads, even though pipelines might be placed in deep waters with high hydrostatic pressure.
- This thesis will be limited to quasi-static experiments even though dynamic loading scenarios are more likely to occur.

## 1.5 Outline of thesis

The chapters in this thesis are arranged thematically, with the first two consisting of experimental setups and results which lay the groundwork for the following calibration of material model and numerical chapters. Another important feature is that the reader is assumed to have knowledge about material mechanics and finite element analysis (FEA). Thus, a theory chapter will not be included, however, the necessary theory will be stated and showed where needed.

Figures consisting of two parts, like a subplot including two plots in the width, will be referred to as “a” for the left figure and “b” for the right figure, where this is not explicitly stated.

**Chapter 2** elaborates on the experimental setups conducted.

**Chapter 3** processes the experimental data and finishes off by comparing the coating system investigated herein with the polypropylene coating system investigated in references [1, 2, 3].

**Chapter 4** begin with a derivation of Desphande and Fleck’s yield criterion followed by material calibration of both the steel and polyurethane materials.

**Chapter 5** utilises the calibrated material models to establish numerical coated pipeline model. After establishing an accurate baseline model, a numerical study investigating density dependency will be performed, followed by a study to see if the model is capable of being extended to other boundary conditions.

**Chapter 6** will discuss the previous finding in more general detail, along with the assumptions made throughout the thesis.

**Chapter 7** includes conclusions made from the study presented in the previous chapters, along with recommendations for further work.

**Appendix** contains figures, measures, tables and formulas along with material datasheets provided by Equinor. The main text can be read without the use of appendix – it will only provide a deeper insight.

# Chapter 2

## Experimental setups

The mechanical behaviour of polymers is complex and very dependent on strain-rate, temperature and stress triaxiality. Thus, numerical predictions are challenging under different loading scenarios, so prototype testing has therefore been the preferred method to qualify the material's application [29]. Therefore, the main mechanical properties of the polyurethane-coated steel pipe-stubs investigated herein will be established by processing the results obtained from a combination of non-destructive and destructive experiments. The former includes measuring, weighing and X-ray micro-computed tomography (XRMCT), while the latter contains uniaxial compression and tensile tests (UC(T) and UT(T)) and denting of pipe-stubs. The experiments are conducted to determine how the materials behave under quasi-static loading and how the materials interact in the pipeline design. Experimental setups along with requested output data will be described in this chapter.

### 2.1 Introduction

The steel in the pipe is manufactured by a process known as the Mannesmann effect making it seamless. For more information on the manufacturing process see reference [30]. Outside the steel lies a coating system produced by Logstor and their production process is outlined on the website given in [31]. The authors of this thesis have not been provided with the exact pipeline model provided by Logstor. However, a short description of the general application processing steps is described below, and is illustrated in Figure A.1:

1. Washing/cleaning of the steel pipeline to easier inspect it for defects.
2. The steel is heated and the anti-corrosion layer (3-LPP) is glued onto the pipe.
3. Next, polyurethane rigid (PUR) is sprayed on top of the anti-corrosion layer.
4. Followed by extrusion of high-density polyethene (HDPE) casing.
5. Finally, the coating system is protected with a polypropylene casing that is welded on top of the outermost layer. This is done since PUR is moisture sensitive (Datasheets in Appendix E).

An illustration of the resulting cross-section is depicted in Figure 2.1 with radial measurements in Table 2.1.

Table 2.1: Measured radiuses in the pipeline design.

Pipe	$r_1$ [mm]	$r_2$ [mm]	$r_3$ [mm]	$r_4$ [mm]	$r_5$ [mm]
Measurements	139.2	161.6	165.0	207.4	216.0

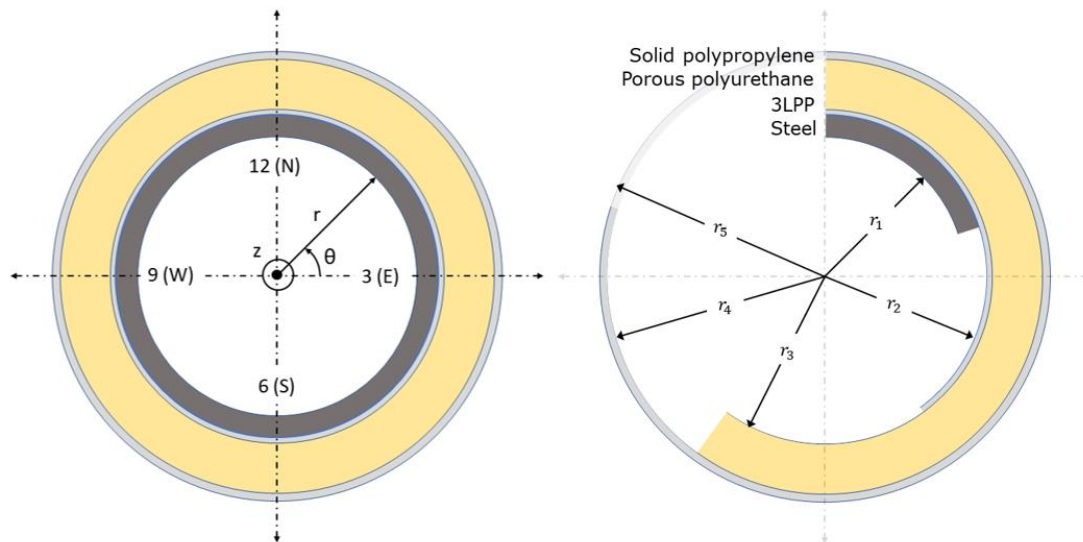


Figure 2.1: Illustration of the PU pipeline's cross-section. (a) With defined coordinates and orientations. (b) Material sections with defined radiuses.

Equinor supplied SIMLab with three pipe-stubs to perform experiments to determine the polyurethane-coated pipeline's behaviour under quasi-static impact loading. The experiment within this thesis aims to replicate impact by trawling gear. A trawling gear will have velocity prior and during impact, making this a dynamic problem. However, one of the results obtained by Vestrum in reference [3] on the polypropylene-coated pipeline is that a quasi-static test can represent the overall coated pipe's ability to absorb impact energy within a certain velocity range. It is assumed that this correlation extends to polyurethane-coated pipelines as well. Quasi-static testing is easier to perform, and the same goes for the post data processing since inertia forces can be neglected due to very low strain-rate [32]. Thus, it became evident that a QS test would be beneficial to perform in this thesis.

The three pipe-stubs were 1m long, and are hereafter referred to as *P1*, *P2* and *P3*. As the pipe-stubs are obtained from a longer pipeline section, it is assumed that the properties at a given position in the cross-section are the same throughout the longitudinal direction of the pipeline. Thus, an effort was made to align the pipe-stubs (from now referred to as "pipe(s)") to have the same orientation. There was no obvious orientation since the pipes are seamless, therefore a thorough visual inspection was carried out to define "north" (N) for all the pipes. This process is illustrated in Figure A.3 and resulting cross-section definition is seen in Figure 2.1a.

*P1* and *P2* will both be subjected to QS denting by different indenters and this will be described in Section 2.6. All the other tests are performed on different sections from *P3*, and the destructive tests (UCT and UTT) are performed QS. Three rings were machined out of *P3* with cross-section as shown in Figure 2.1, each with a depth of approximately 45mm. These rings are labelled *A*, *B* and *C*, where *A* is the first/outermost ring that were cut out, then *B* and lastly *C*. Every experiment described below is performed at NTNU's laboratory facilities in Trondheim by competent laboratory personnel.

## 2.2 Material specimen description

Three different types of specimens were taken from the rings  $A, B$  and  $C$ , and are depicted in Figure 2.2. Measuring, weighing and XRMCT had to be performed before the destructive experiments to ensure that the geometry in the numerical models is accurate. Table 2.1 contains the resulting radii obtained from a series of measures done on the rings extracted from  $P3$ . The reader is referred to Appendix B for tables and graphs of all measures and weights.

What will be referred to as “material specimens” are shown in Figure 2.2a. The material specimens are cylinder samples from the polyurethane part of the coating and are collected from the clock position 1 and 2 of the second ring ( $B$ ). As illustrated, three samples are obtained in the radial direction at both locations labelled as  $i, m$  and  $o$  for inner, middle, and outer layer, respectively, where the  $i$ -specimens are closest to the steel. Hence, the material specimens’ will be labelled  $1i, 1m, 1o, 2i, 2m$  and  $2o$ . The heights and diameters vary between  $[10.06, 12.36]$  and  $[11.62, 11.87]$  in  $[mm]$ , respectively, for the six material specimens. Geometrical measures are reported in Table 3.3 and will be used there.

Figure 2.2b illustrates a sample including all material layers and will be referred to as “sandwich”. From each of the three rings, four sandwich specimens were cut out at the clock positions 12, 3, 6 and 9. Resulting in a total of 12 specimens with an average height of 76.8mm, and an approximate width in both the hoop- and the longitudinal direction of 44.4mm. Recalling that the rings are labelled  $A, B$  and  $C$  resulting in sandwich labelling of  $12A, 12B, 12C, 3A$ , etc.

Four identical steel samples were taken from the second ring ( $B$ ) at the clock position 5 and 11, two at each location with its length in the pipe’s longitudinal direction, and labelled them  $5A, 5B, 11A$  and  $11B$ . These steel specimens were machined out as standard Split-Hopkinson tensile bar (SHTB) specimens with geometry as illustrated in Figure 2.2c and geometrical measures as given in Figure A.2.

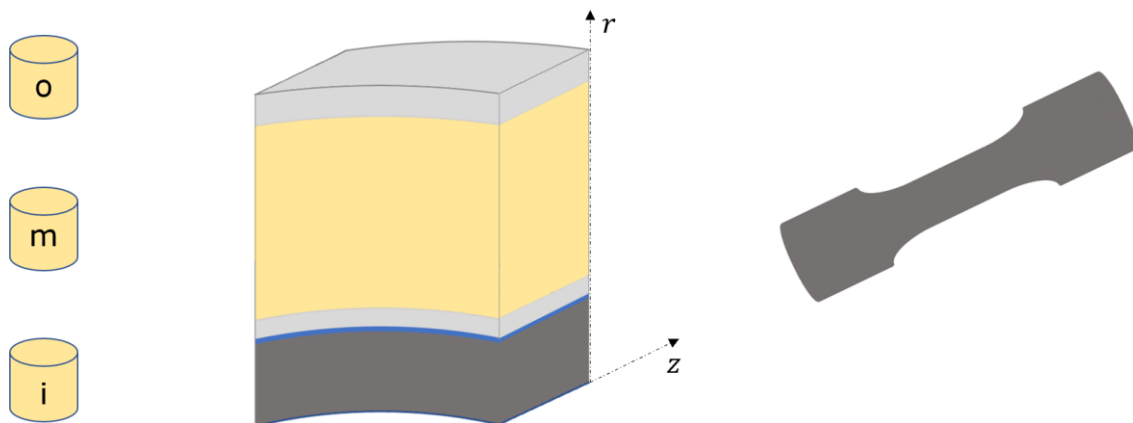


Figure 2.2: Three different material specimens: (a) PU material specimens with  $i$  - inner,  $m$  - middle and  $o$  - outer layer, (b) sandwich specimen and (c) Split-Hopkinson tension bar steel specimen.

## 2.3 X-ray micro-computed tomography setup

XRMCT is a valuable tool to characterize pore structure and density in a 3D volume by placing a material specimen between an X-ray source and a detector as illustrated in Figure 2.3. It is based on the difference between incident and transmitted X-ray radiation which creates two-dimensional greyscale projections of a body. Using advanced software algorithms, the projections can be used to reconstruct the volume of the test specimen as seen in the right part of Figure 2.3. The computed volume is represented in a three-dimensional (3D) array of cubic voxels. The volume reconstruction was conducted using the software Nikon CT Pro 3D (version 4.4.3). For more detail about the theoretical background of the imaging technique and post-processing of the acquired data, the reader is referred to, e.g., Als-Nielsen and McMorrow [33] and [34].

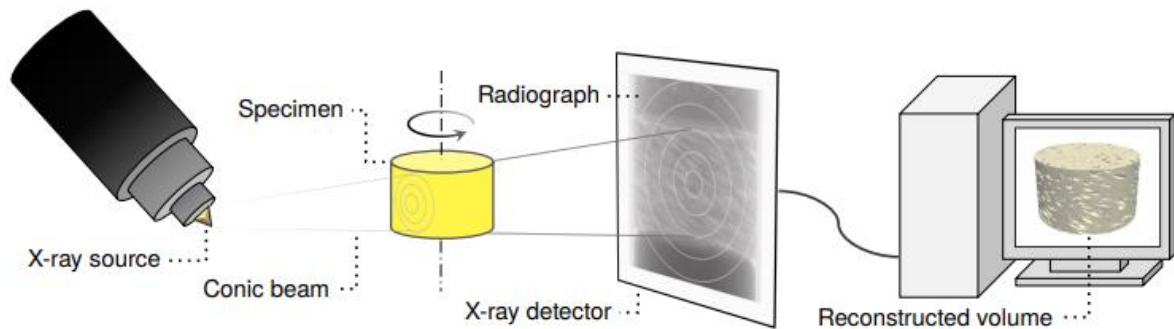


Figure 2.3: Schematic diagram of the XRMCT setup and process [3].

A total of 10 samples, all the material specimens and four of the sandwich samples, were analysed using a Nikon XT H 225 ST system. This system offers a microfocus X-ray source, high image resolution and ultrafast CT reconstruction [35]. It is a system ideally suited to a wide range of materials, such as plastic parts, small castings, and complex mechanisms. The system can analyse parts up to a maximum of 50kg with a diameter of about 50cm. The configuration used in these analyses is a 225kV wolfram (sandwich) and molybdenum (material specimen) reflection target and a panel detector of 2000pixels x 2000pixels, 200 micrometer pixel size and 16-bit pixel depth. To decrease the noise in the tomographic projections, the average of two X-ray images (each with 1s exposure time) was taken. XRMCT scanning has numerous advantages as components can be analyzed without destroying the part and is therefore a valuable tool for material and component investigation.

## 2.4 Steel experimental setup

As described in Section 1.2, Martin Kristoffersen [22] investigated a commonly used steel grade in the offshore industry known as X65. Steel grade X65 requires a minimum yield strength of 450MPa (65ksi). The pipes investigated was assumed to have the same characteristics as Kristoffersen's steel, implying same steel grade, homogenous and isotropic properties. Thus, only four samples were machined out to validate this steel grade. Denting on bare steel pipes has not been conducted in this thesis, and the reader is referred to Kristoffersen's PhD. thesis [22] for further reading on this subject.

Uniaxial tensile tests of the smooth axisymmetric steel specimens were conducted in a 30kN Zwick stretching rig with a setup as shown in Figure 2.4. The minimum diameter of the specimen is measured from two perpendicular angles by an AEROEL XLS13XY laser gauge.

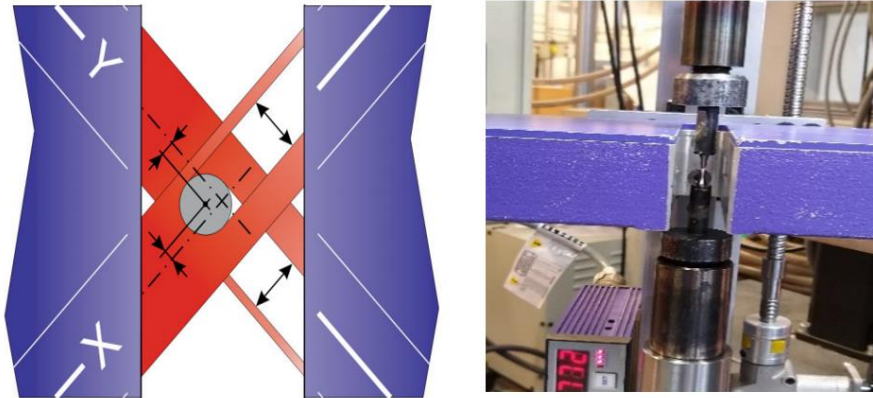


Figure 2.4: Uniaxial tensile test setup with (a) top view of the laser measuring field [36] and (b) front view of steel specimen in stretching rig.

The lasers create a beam towards the detector on the opposite side, creating a box of laser light around the cross-section of the sample. The laser gauge has a measuring field of  $13\text{mm} \times 13\text{mm}$  [36] and is mounted on a mobile frame to adjust for the location of the smallest area of the specimen continuously. Here, the area  $A$  follows the known relationship

$$A = \frac{\pi}{4} D_x D_y \quad (2.1)$$

where  $D_x$  and  $D_y$  are the diameters in two perpendicular directions as illustrated in Figure 2.4. These diameters are logged as the test is performed and synchronized with the output of the applied force and displacement.

To secure quasi-static conditions, the specimens are stretched with a constant deformation velocity of  $0.15\text{mm/min}$  until the specimen fracture. The specified velocity  $v$  is found through its known relationship with strain-rate  $\dot{\epsilon}$  and the initial gauge length  $h_0$  as

$$v = \dot{\epsilon} h_0 \quad (2.2)$$

Here, the strain-rate is specified as  $5 \cdot 10^{-4}\text{s}^{-1}$  and with an initial gauge length of  $5\text{mm}$ .

## 2.5 Uniaxial compression setup

All the PU material specimens and sandwich samples were subjected to quasi-static uniaxial compression in an INSTRON 5985 test rig with  $5\text{kN}$  and  $250\text{kN}$  load cells, respectively. In contrast to the data logged for the tensile test, only force and displacement on the load cell are logged during these compression tests. Hence, all the samples subjected to UC were sprayed with a speckle pattern facing a digital camera, Basler acA4112-20um. See test setup in Figure 2.5. The camera's output was synchronized with the machine's output at  $2\text{Hz}$ . Further, the lights were positioned to create a contrast of the specimens' edges and the background, increasing the focus of the camera towards the edges with the aim of obtaining the current area. The speckle pattern and use of contrast in the images will be described in more detail within Section 3.4.1.



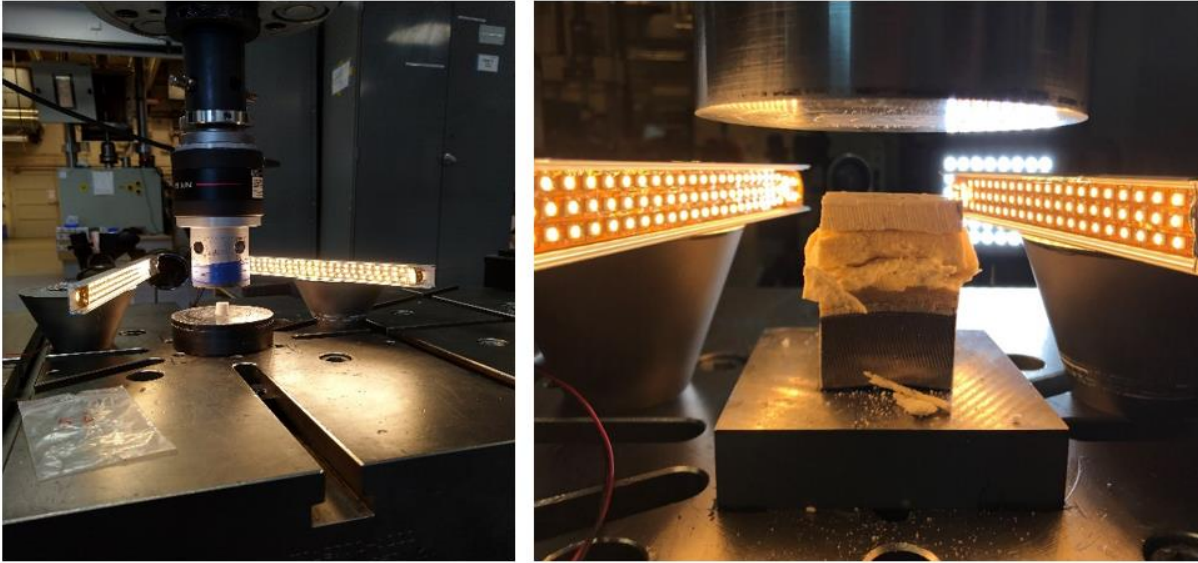


Figure 2.5: Setup of the uniaxial compression tests. (a) PU material specimen with a 5kN load cell. (b) sandwich sample with a 250kN load cell after test.

Quasi-static conditions in both test setups are valid by assigning the strain-rate as  $10^{-3} \text{ s}^{-1}$ .

### 2.5.1 Material specimen test

The machine was specified with an initial velocity of 0.6mm/min for the material specimens. Which is obtained by inserting  $\dot{\epsilon} = 10^{-3} \text{ s}^{-1}$  and  $h_0 = \min(h_{0\text{PU}}) \cong 10\text{mm}$  in Equation (2.2). A lubricant, Molykote, was applied to the top and bottom of the specimens to reduce friction between the rig and the specimen. Lower friction will lead to a more uniform deformation, and less barrelling [37].

### 2.5.2 Sandwich sample test

Datasheets (given in Appendix E) from Logstor indicates that PU is the weakest material in the sample. Thus, the strain-rate will be computed from the initial height  $h_{0\text{Sandwich}}$  of the PU in Equation 2.2 which was set to an approximate height of 40mm. Inserting this along with the defined strain-rate gives an initial velocity of the compression of 2.4mm/min. No lubrication was applied to these samples since the deformation will be concentrated in the PU part of the sample. This will be described in more detail within Section 3.4.3.

## 2.6 Quasi-static denting of pipe setup

An INSTRON testing system in the 8800-series [38] with a force capacity of 5000kN was used to perform the quasi-static denting of the two equal pipes,  $P1$  and  $P2$ . To utilise this machine, the pipes had to be placed on top of several plates, that again laid on beams to build height in the setup, see test setup in Figure 2.6. Several calculations were done to validate the capacity of the beams prior to performing the experiment. The test setup included a laser inside the pipe to measure internal deformations, and two cameras, Basler aCA2440-75um, one in each of the views shown in Figure 2.6. The force and displacement of the indenter are measured by the testing rig, and all the logged data is synchronized with a frequency of 1Hz.



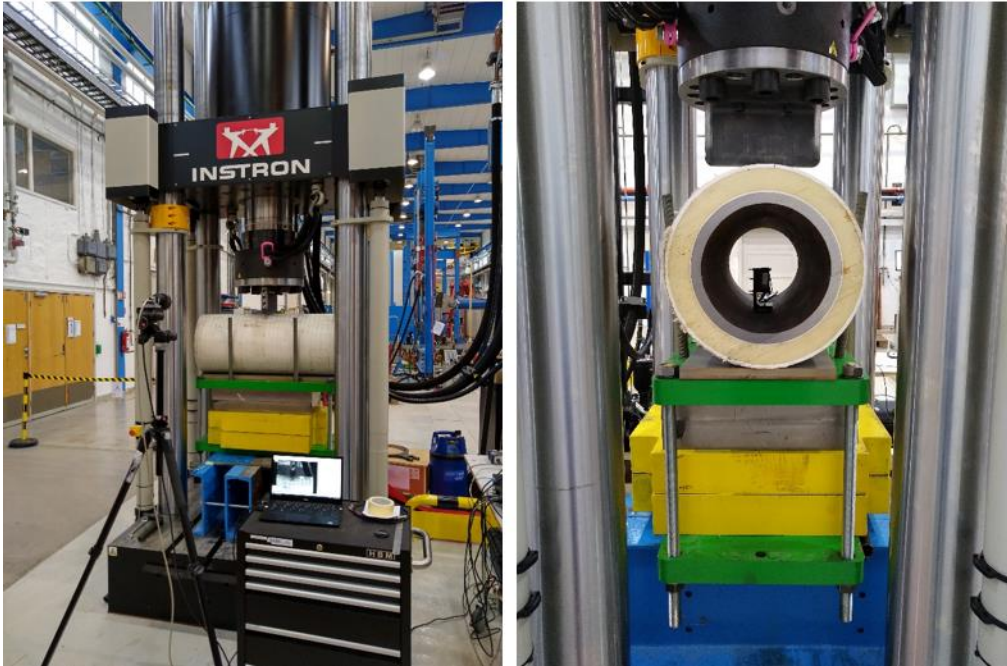


Figure 2.6: Denting of pipe with the big indenter. (a) Experimental setup with camera 1 logging the deformation in the indentation zone, and (b) is the view from camera 2, showing the laser placed inside the pipe measuring the inner indentation.

Pipe 1 and pipe 2 were dented by two different types of indenters referred to as the big and small indenter, respectively. The big indenter has a nose-radius of 25mm and is the reference case in DNV GL's recommended practice [5], while the small indenter has a nose-radius of 10mm. Sharp edges on trawling gear can occur which motivates experiments with the small indenter [5]. They are illustrated in Figure A.4 and Figure A.5 in the Appendix. The machine was prespecified with a loading/unloading program with cycles of 300kN with a loading velocity of 10mm/min to obtain quasi-static loading until a displacement of 100mm was achieved.

Defined by Jones and Birch [18] and illustrated in Figure 1.2, it was assumed that the coated pipes investigated herein will fail due to inelastic failure in the steel and the coating will crack directly below the indenter. Previous studies performed on both uncoated and coated steel pipes indicates that the pipe's deformation is very local [3, 22]. Thus, each pipe was dented twice. After the first test on each pipe, it was rotated 90° for a second test. The retest is labelled with an *R* to denote that the pipe has been rotated. The labelling *P1*, *P1R*, *P2* and *P2R* is used to distinguish the tests.



# Chapter 3

## Experimental results

Four different experimental setups were described in the previous chapter, which resulted in a total of 36 performed tests and an extensive amount of raw data. Necessary theory of strain measure and its work conjugate pair will be presented shortly, with the aim of establishing the state variables [39] along with mechanical properties for the steel and polyurethane. The measured density of polyurethane foam will be verified from processed XRMCT data.

The polyurethane-coated pipe's behaviour and ability to absorb energy will be determined towards the end of this chapter. Both the coating's and steel's ability to absorb energy, separately and combined, will be analysed. Lastly, this coating system's absorption ability will be compared to the polypropylene coating system investigated in [1, 2, 3].

### 3.1 Strain measure

Material model of the steel and polyurethane is based on uniaxial tensile and compression tests, respectively. Both tests start in a reference (initial) configuration  $C_0$  to which state variables such as strains and stresses are referred to. Initially, these variables are assumed to be zero and correspond with the initiation of the test. As the samples are either stretched or compressed, the state variables change, and material points are displaced. Lagrangian (material) coordinates  $\mathbf{X}$  are chosen to describe the deformation of any material point in the solid. Here,  $\mathbf{X}$  is the location in Cartesian coordinates for a given material point  $C_0$ . Lowercase  $\mathbf{x}$ , on the other hand, refers to the location in a current configuration  $C_n$ . During either UT or UC, the specimens configurations relate through displacement  $\mathbf{u}$

$$\mathbf{x}(\mathbf{X}, t) = \mathbf{X} + \mathbf{u}(\mathbf{X}, t) \quad (3.1)$$

where  $t$  is the time. Both tests are presented to be uniaxial which reduces this three-dimensional (3D) problem to a one-dimensional (1D) problem. Rearranging, the uniaxial displacement  $u$  can now be expressed as

$$u = L - L_0 = \Delta L \quad (3.2)$$

Here,  $L_0$  refers to the initial length/height of the specimen and  $L$  is the final length. The deformation between two particles is represented with a strain measure. First, a linear strain measure  $e$  is obtained by dividing Equation (3.2) with its initial length

$$e = \frac{u}{L_0} = \frac{\Delta L}{L_0} \quad (3.3)$$

This linear strain measure is the well-known engineering strain and is easily obtained since  $u$  is one of the given outputs from the experiments and  $L_0$  is known. However, the deformation in both PU and steel results in large strains which yields the need for another strain measure. Two typical finite strain measures are the Green and Almansi strains, where the former is finite in infinite compression while the latter is finite in infinite stretching. As the materials tested in this thesis will be subjected to large strains in both compression and stretching, a nonlinear

strain measure valid in both ranges is preferred and will be chosen. A strain measure with this ability is based on infinitesimal strain theory  $\delta\varepsilon$  and has the form like Equation (3.3), by letting  $\Delta \rightarrow \delta$  and  $L_0 \rightarrow L$ . Integrating the incremental strain from initial to final length, and the true (logarithmic) strain  $\varepsilon_1$  measure reads

$$\varepsilon_1 = \int_{L_0}^L \delta\varepsilon = \int_{L_0}^L \frac{\delta L}{L} = \ln \left[ \frac{L}{L_0} \right] \quad (3.4)$$

True (Cauchy) stress  $\sigma_t$  is work conjugate to this strain measure and is given as

$$\sigma_t = \frac{F}{A} \quad (3.5)$$

$F$  is the force applied and one of the outputs from the experiments, and  $A$  being the true area corresponding to the applied force. The true area is logged during the UT test, but not with the UC test. Obtaining the true area of the PU material specimens is described in Section 3.4.1. It should be noted that the engineering stress  $s$  which is work conjugate to the engineering strain is given as  $s = F/A_0$ . Both engineering measures are referred to the initial geometrical measures ( $L_0, A_0$ ) while the true conjugate pair uses current geometrical measures ( $L, A$ ).

Note: when utilising conventional “rules”, compression yields negative values of the force. In the same manner, as the specimens’ contract during either UC or denting, this yield conventionally negative values of the displacement as well. Thus, force versus displacement will be in the third quadrant of a graph. Both stress and strain are derived parameters of the force and displacement, respectively, yielding both with negative values as well. However, due to illustrating purposes, the absolute values will be shown in their respective graphs in the first quadrant. Hence, all graphs regarding this matter throughout this thesis will be shown in the first quadrant.

## 3.2 X-ray micro-computed tomography results

The PU coating discussed in this thesis is a porous polymer known as a cellular solid. A cellular solid is made up of an interconnected network of solid struts or plates which form the edges and faces of cells. The single most important feature of a cellular solid is its relative density  $\bar{\rho}$  which is a function of the density of the cellular material  $\rho^*$  and the density of the solid material of which the cell walls are made of  $\rho_s$ . Literature implies that  $\rho_s = 1.2 \frac{\text{g}}{\text{cm}^3}$  for solid polyurethane [23] (Appendix E). The relative density is defined as follows:

$$\bar{\rho} = \frac{\rho^*}{\rho_s} \quad (3.6)$$

The fraction of pore space in the foam is its porosity  $f_p$ , which is simply defined as

$$f_p = 1 - \bar{\rho} \quad (3.7)$$

Generally, cellular solids have relative densities lower than about 0.3, most have much less [23]. Most mechanical and thermal properties are more dependent on cell shape than cell size. If the cells are equiaxed, the properties are isotropic, but with only slightly elongated cells, the properties depend strongly on the direction [23]. Foams are three-dimensional cellular solids and can be divided into cells which are closed and open. A closed foam structure has its cells sealed off from its neighbours by membrane-like faces, while in an open structure the cells

interconnect [23]. The cell connectivity can also have a great effect on properties. The porous polyurethane coating discussed herein is a rigid foam (PUR), which implies a majority of closed cells. The amount of closed cells is stated to be approximately 93% from the manufacturer, see Datasheets. Since a porous polymer is so dependent on its relative density and cell structure, it is of great interest to investigate the pore structure closely and how the relative density varies through the thickness of the pipeline coating.

Cutting the sandwich samples yielded a lot of small steel chips around on the PU part of the sample which was hard to remove before scanning. These chips will absorb most of the energy during scanning as they have a density of approximately 26 times that of the PU material which resulted in poor scanning results. However, the scans of the smaller cylinders (material specimens) yielded good results with much more detail. Figure 3.1a-b show how a material specimen was placed inside the XRMCT machine and Figure 3.1c shows one reconstructed XRMCT image. Reconstructed images were obtained by the reconstruction software in the computer connected to the XRMCT machine. The volume is reconstructed by a series of images from bottom to top with the view as illustrated in the figure. The images come in greyscale where white and black represent solid material and gas pockets, respectively. Table C.1 and Table C.2 in the appendix show the XRMCT scans conducted and the configurations of the XRMCT system used during the analysis. To reduce space and computational demand, only 8-bit pixel depth was utilized even though the detector plate is capable of a 16-bit pixel depth.

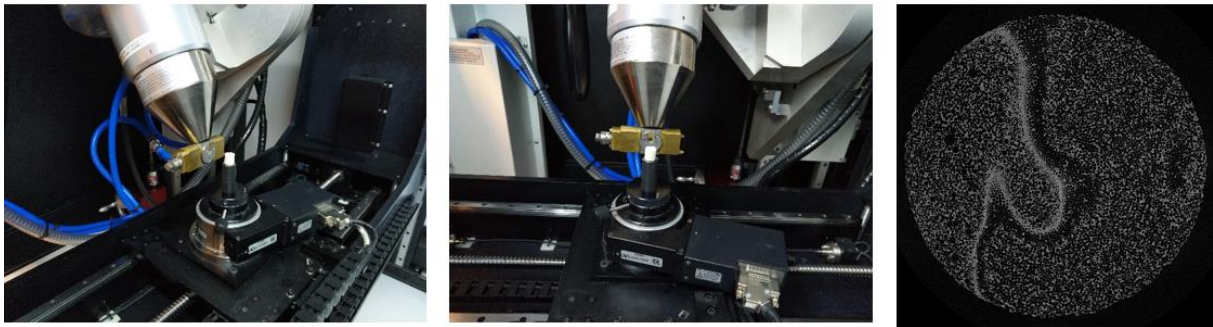


Figure 3.1: XRMCT machine with (a) side view and (b) view from back plate of source, holder and specimen. (c) Reconstructed image from an XRMCT analysis of the material specimen.

Otsu's method [40] was used to binarize the greyscale images obtained from the XRMCT. The processed scans from the XRMCT contains  $4 \cdot 10^6$  pixels (2000 pixels x 2000 pixels), each with a greyscale value of 0 to 255 where 0 is black (background) and 255 is white (material). It was necessary to binarize the pictures into black and white to enhance the difference between material and gas pockets in the material specimens. Otsu's method binarizes the data by choosing a threshold value which minimizes the within-class variance  $\sigma_W^2$  of the picture. This is calculated by iterating through the picture greyscales with different greyscale threshold values. The threshold value which gives the lowest  $\sigma_W^2$  is chosen as the threshold value for binarization. Equation (3.8) shows the within-class variance, where the sub-indexes b and f stands for background and foreground (material), respectively.  $W_b$  and  $W_f$  are the weights of the pixels in either class, while  $\sigma_b^2$  and  $\sigma_f^2$  is the variance within either class [40].

$$\sigma_W^2 = W_b \sigma_b^2 + W_f \sigma_f^2 \quad (3.8)$$

Binarized images result in only two greyscale values of 0 (non-material) or 255 (material). Figure 3.2 depicts a reconstructed XRMCT scan and its binarized image. The binarization

procedure was conducted in a modified version of the Python script presented by Vestrum in [34]. This modified script counts the number of black and white pixels in a fraction of the binarized image and makes it possible to calculate the relative density following the relationship given below.

$$\bar{\rho} = \frac{\text{Number of white pixels}}{\text{Total number of pixels}} \quad (3.9)$$

Otsu's method for the XRMCT data resulted in a threshold value of 3 or 4, depending on the image series under evaluation. Figure 3.3 shows where the specimens were extracted from and how the relative density varies in the radial direction. Figure 3.4 shows the relative density variation of specimen 2. Frame 1 represents the inner radius of the coating, while the frame number increases with increasing thickness in the radial direction.

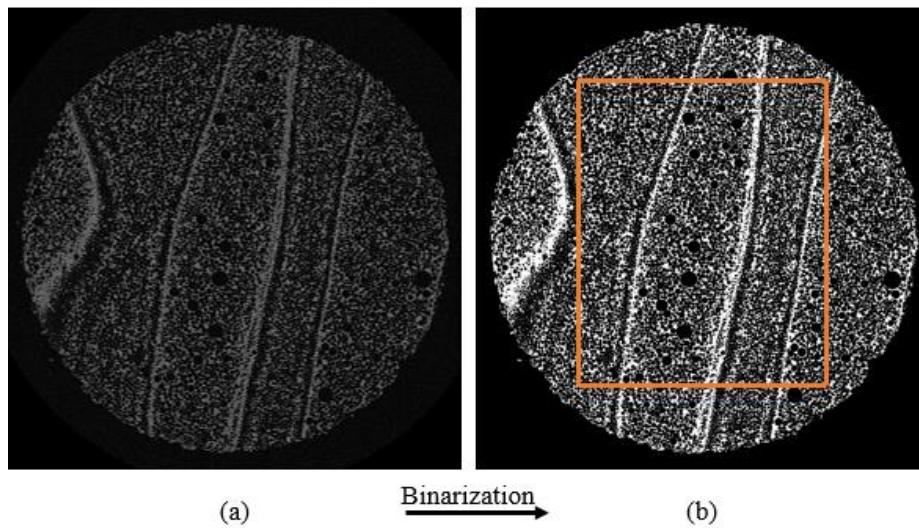


Figure 3.2: CT-image before and after binarization using Otsu's method. The orange square indicates the fraction being analysed

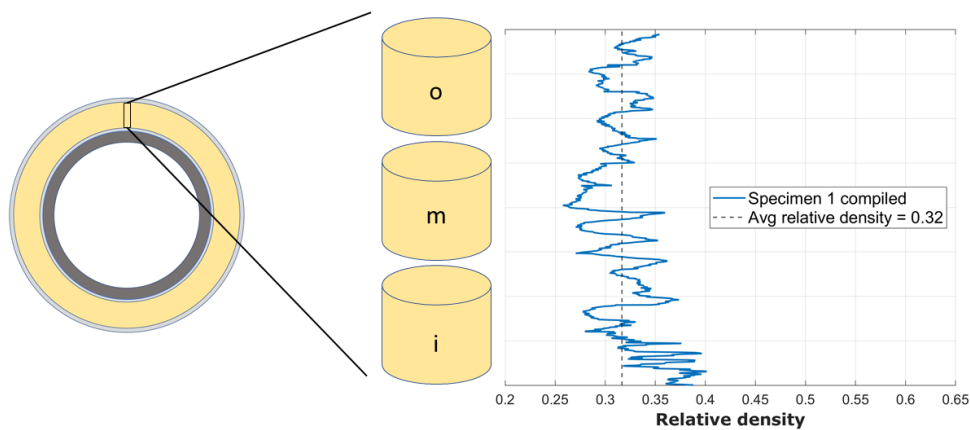


Figure 3.3: Variation of relative density throughout the radial direction of the polyurethane part of the coating.

Because of the way the specimens are cut out of the coating and adjustments that had to be made to remove noise in the initial XRMCT images for each scan, parts of the density data is lost, which will affect the results. In addition, due to lack of computational memory, the image data series had to be processed in parts by the Python script. This resulted in different threshold values for some image series. A change of threshold value for the binarization can be seen in



Figure 3.4 right after frame 2000, where the relative density drops about 0.03. This suggests that the method used to estimate the relative density lacks some accuracy and is sensitive to the choice of the threshold value. However, the relative density plot gives some information as to how the density varies through the thickness of the coating. It is observed that the relative density is somewhat uniformly distributed as it oscillates around the average value throughout the whole thickness.

The vertical stapled lines in Figure 3.4 represent the boundary between the inner, middle and outer specimens of PU in the compiled coating cylinder. A similar plot is reported in Figure A.6 for specimen 1. Since the specimens are cut out with a saw, some data is missing between these layers. This may create a gap in relative density at the boundary. Further, it is seen that the inner specimen has the highest average relative density and the middle specimen has the lowest average density. This phenomenon corresponds well with the measured values, and Table 3.1 contains the measured densities and the relative densities obtained from XRMCT. Note that the outer specimens (1*o* and 2*o*) are very close to the average density.

Following Equation (3.6), the average relative density from the measured values is  $\bar{\rho}_{\text{measure}} = 0.28$  while the average relative density from XRMCT is  $\bar{\rho}_{\text{XRMCT}} = 0.31$ . These values are above the minimum relative density as Logstor refers to in their Datasheet is 0.25, see Appendix E, but differs with 10%. Recall that relative density of 0.3 is the transition between foam and porous material [23, 24], and the polyurethane studied herein lies around this value.

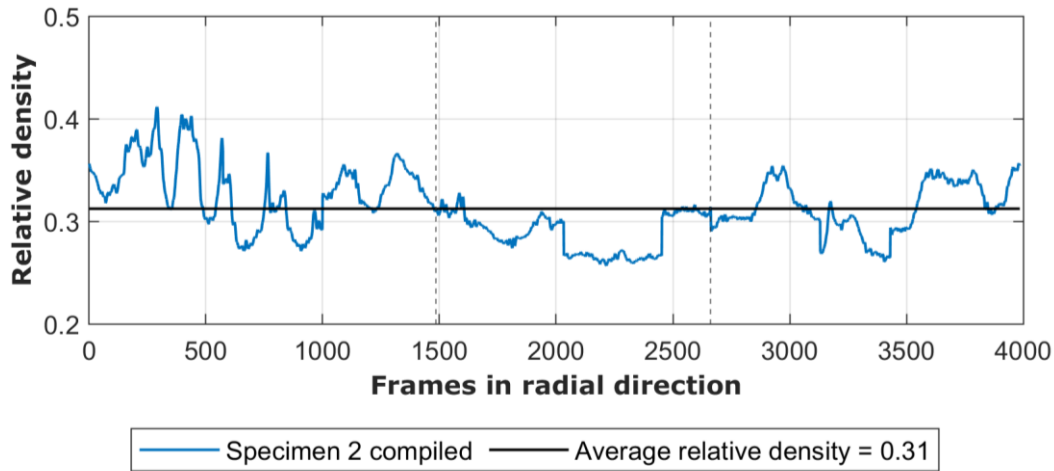


Figure 3.4: Relative density of specimen 2 when combining the inner, middle and outer layer. Frames from innermost (0) to outermost (4000) radius.

Table 3.1: Density calculated from measurements and relative density obtained from XRMCT.

		$\rho_{\text{measure}} \left[ \frac{\text{g}}{\text{cm}^3} \right]$	$\rho_{\text{avg}} \left[ \frac{\text{g}}{\text{cm}^3} \right]$	$\bar{\rho}_{\text{XRMCT}} [-]$	$\bar{\rho}_{\text{avg}} [-]$
1	<i>i</i>	0.346		0.333	
	<i>m</i>	0.317	0.330	0.298	0.317
	<i>o</i>	0.327		0.316	
2	<i>i</i>	0.373		0.331	
	<i>m</i>	0.325	0.347	0.288	0.312
	<i>o</i>	0.342		0.314	

### 3.3 Uniaxial tension test results

Seamless steel indicates that the material properties will be equal at all locations on the cross-section. Figure 3.5 contains force versus displacement (FD) plots from all four UT tests and it is seen that all coincide very well, implying homogenous material behaviour. Two perpendicular diameters were outputs from the test, and their ratio  $D_x/D_y$  is constant implying isotropic behaviour. Utilising infinitesimal strains, it is reasonable to assume a linear relationship between the stress and strains which is given as  $\sigma = E\varepsilon$  in 1D [41]. This is known as Hooke's law and materials obeying this is said to be linear elastic materials. Thus, the steel is an isotropic homogeneous linear elastic material, the same as Kristoffersen's result of the steel he investigated [22]. By inspection, it is found that the obtained FD is very similar to Kristoffersen's implying the same steel grade with the same properties. Hence, no further testing on the steel is conducted. Young's modulus  $E$  and Poisson's ratio  $\nu$  can be taken from Kristoffersen as  $E = 208$  GPa and  $\nu = 0.3$  [22].

Inserting the diameters obtained from the test into Equation (2.1), results in the current area  $A$ . This data can be used to establish the true stress through Equation (3.5) and true strain by

$$\varepsilon_1 = \ln \left[ \frac{A_0}{A} \right] \quad (3.10)$$

Here Equation (3.10) follows by employing isochoric conditions in Equation (3.4). Isochoric conditions are valid when there are no volumetric changes ( $V = V_0$ ) as the material deforms. This will be discussed in more detail in the next section.

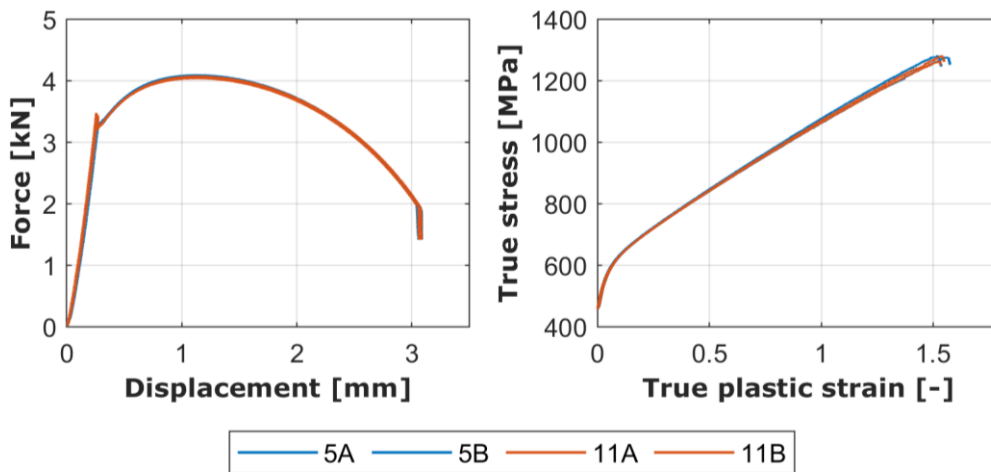


Figure 3.5: Combined force versus displacement and true stress versus true plastic strain for all the UT tests. Defined legends in Section 2.2.

From the provided Young's modulus and Poisson's ratio, the elastic domain of the steel is described by Hooke's law [41, 42]. The yield stress  $\sigma_{0.2}$  is defined as the stress that will result in a plastic strain of 0.2%, the so-called 0.2% offset yield strength. The average yield stress of the specimens was found to be 459.25MPa, which is above the requirement of being X65 steel grade. Figure 3.5b shows true stress versus true plastic strain plotted from yield to fracture.

Important material data can be found from the experimental data. The material has (based on the average of the four uniaxial tension tests) an ultimate tensile strength  $s_{\max}$  of 569MPa, where the engineering strain  $e(s_{\max})$  reaches 0.154. The true stress at failure,  $\sigma_f$  reaches a value of



1276MPa, at which the true failure strain is 1.549.  $W_{cr}$ , which is the “work per volume” to failure or simply the area under the true stress versus true strain curve, has a value of 1463Nmm/mm<sup>3</sup>. The reader is referred to Appendix D and [43] for more information on the extended Cockcroft-Latham criterion and its plastic dissipation at failure  $W_{cr}$ . The data is presented in Table 3.2 for all four tensile specimens. Two measures are defined in the two lower rows, namely *avg* representing the average in each column, while *STD* is the standard deviation in the same column, and is defined in Appendix D. A low spread is observed in all parameters.

Table 3.2: Material data from the processed uniaxial steel tension tests.

ID	$A_0$ [mm <sup>2</sup> ]	$\sigma_{0.2}$ [MPa]	$s_{max}$ [MPa]	$e(s_{max})[-]$	$\sigma_f$ [MPa]	$\epsilon_f[-]$	$W_{cr}$ [ $\frac{Nmm}{mm^3}$ ]
5A	7.1679	456	570	0.1467	1276	1.574	1481
5B	7.1679	465	570	0.1575	1281	1.533	1455
11A	7.1442	462	566	0.1588	1264	1.541	1446
11B	7.1300	454	571	0.1531	1281	1.547	1470
<i>avg</i>	7.1525	459	569	0.1540	1276	1.549	1463
<i>STD</i>	0.016	4.4	1.7	0.0047	6.9	0.015	13.47

### 3.4 Uniaxial compression test results

As written in the previous chapter, the area is not included as one of the outputs in the conducted UC tests, but is needed to utilise the equations derived in Section 3.1. In Section 3.2 it was found that the polyurethane foam contains many pores in different sizes through the coating thickness. These pores contribute extensively to the initial volume  $V_0$  of the material specimen and sandwich sample. The assumption of isochoric condition is not valid when deforming porous materials. Contraction of porous solids includes the collapse of the cells, and due to this, a porous material’s volume changes when being compressed [23],  $V \neq V_0$ . This being a known phenomenon, a camera was included in the test setup to capture the width of the sample during UCT, as mentioned in Section 2.5. It was also assumed that the compressed samples will deform symmetrically which resulted in only one camera facing the test. Post observations on the material specimens implied that this was a valid assumption, and the area in Equation (2.1) is obtained by letting  $D_x = D_y = D$ . However, the diameter is not an output of the camera, images are. The images are analysed in eCorr Digital Image Correlation (DIC) [44] software developed at NTNU and will be elaborated on. Note that this analysis procedure was only conducted on the material specimens and not on the sandwich samples due to extensive cracking. Neither are the state variables of primary interest for the sandwich samples.

#### 3.4.1 eCorr Digital Image Correlation

Stated in Section 2.5, the material specimens were painted with a speckle pattern (greyscale pattern) facing the camera that focuses on the edges. eCorr DIC is a software that tracks the movement in the sequence of images using the greyscale pattern on the specimen and assumes conservation of optical flow. For more information on eCorr and its assumptions, the reader is referred to [44]. The software offers edge tracing and was initially intended to obtain the area during deformation. However, this tracking method was not applicable due to the cracking of the material. When the specimen cracked, the main assumption of conservation of optical flow was no longer obtained in the interesting regions. As the images are very blurry in the middle

of the specimens, as can be seen in Figure 3.6, no mesh could be assigned to track the movement. Fortunately, eCorr offers subset DIC and will be described in the following.

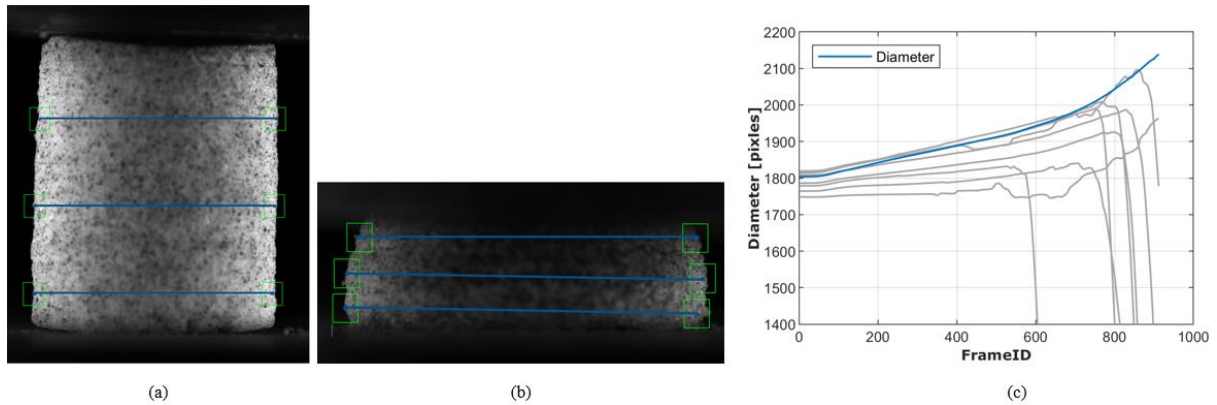


Figure 3.6: Illustration of subset DIC with resulting diameter vectors. (a) Assigned subset-pairs with vectors in the reference image, (b) is the final image illustrating contraction in the specimen's height and elongation in the vectors. (c) Plot of a vector selection obtained from a subset DIC analysis.

Figure 3.6 illustrates the procedure of utilising subset DIC. It should be noted that this figure is only for illustrating purposes, and several more subsets along each edge were assigned to obtain higher accuracy. A subset is defined as a point in the initial image with a specified square surrounding it symmetrically, see Figure 3.6a-b. The DIC analysis of a subset corresponds to the information inside of the square. Hence, by assigning a bigger square the analysis search in a bigger region yielding higher accuracy at the cost of increased computational time. The area of the squares used in this analysis was set to 70pixels x 70pixels, a trade-off between computational time and accuracy. Even though Figure 3.6b is the last frame in the sequence, it could represent any in between. The requested output from subset DIC analysis was to obtain a vector connecting two subsets on the opposite side of each other, as seen in Figure 3.6a-b. For each image (Frame), the vector's length is extracted, and the resulting vectors from analyzing material specimen 1*i* is shown in Figure 3.6c. Similar results are obtained for the other specimens as well. FrameID 0 and approximately 900 along the x-axis correspond to the reference image and last deformation image, respectively. A vector's length  $vec$  is given in [pixels] and need to be converted to [mm]. A converting ratio  $r_c$  is easily obtained since the initial diameters  $d_0$  were measured,  $r_c = \frac{d_0}{vec_0} \left( = \left[ \frac{\text{mm}}{\text{pixels}} \right] \right)$ . Initial diameters are reported in Table 3.3. Substitute  $D = r_c vec$  in Equation (2.1) to obtain the true area.

Not all subset-pairs yielded accurate diameters for different reasons. The main one is due to cracking of the specimen during compression which destroys the conservation of optical flow inside a subset. Thus, the subset-pair describing the true diameter had to be chosen carefully, and is illustrated as the blue line labelled "Diameter" in Figure 3.6c for specimen 1*i*.

### 3.4.2 Material specimen results

Typically [23], porous polymers are known to have three distinct regions when being compressed, which can be seen in a stress versus strain plot. First, a linear increase defines the first region until the graph starts moving somewhat horizontally in its next region, the plateau. These regions are distinct at the material's yielding point. Lastly, the transition over to the region known as densification. Densification in a foamed material is when all the pores are fully compressed, and the material starts to behave more similar to a solid material [23]. These

regions can be seen in Figure 3.8. However, it was a goal to compress the specimens far into the last region of densification. Through some hand calculations, it was found that a 5kN load cell was suitable for this purpose.

The tests were performed until approximately 4.5kN corresponding to ~74% compressed of each specimen's height. A sequence going from 0% (initial) to 71% (final) deformation of specimen 1*i* is illustrated in Figure 3.7. Minor barrelling effects are seen, but this will be neglected in the following. All specimens started to fracture around the yielding point and the fracturing increased throughout the experiment. Fracturing phenomenon will be described in more detail in the following section.

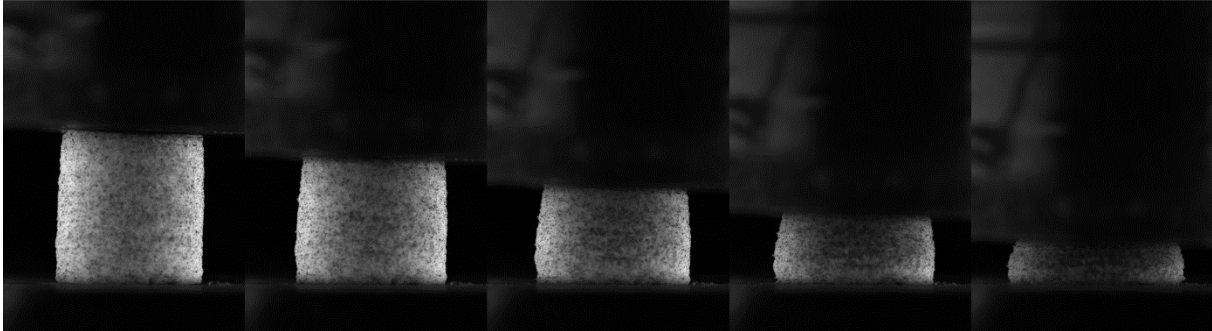


*Figure 3.7: Deformation timeline of material specimen 1*i* ranging from initial to final state of compression.*

Prior to using the relationship between force and stress given in Equation (3.5), the raw force data obtained from the experiments must be modified. The grey line in Figure 3.8a is the raw data plotted for specimen 1*i*. The graph has an s-shape in the elastic region which contradicts the assumption of linear elastic material (infinitesimal theory). Thus, the s-shape is not accurate, so the force and displacement obtained from the experiments must be modified to be linear in the whole elastic region and adjusted to start in origin. The blue line in the Figure 3.8 is the modified force versus displacement for specimen 1*i*. With the modified force and displacement, along with corresponding true area obtained from the DIC in the previous section, true stress versus true strain can now be calculated by Equations (3.4) and (3.5). The result is seen in Figure 3.8b with the same legends. Note: the start of the s-form is due to height differences of the specimens yielding that the machine will log displacement before it will compress the specimens. Also, the first contact between the load cell and the specimen will imply some contraction in the machine, which gives rise to a small increase in load prior to the linear increase of material until yielding.

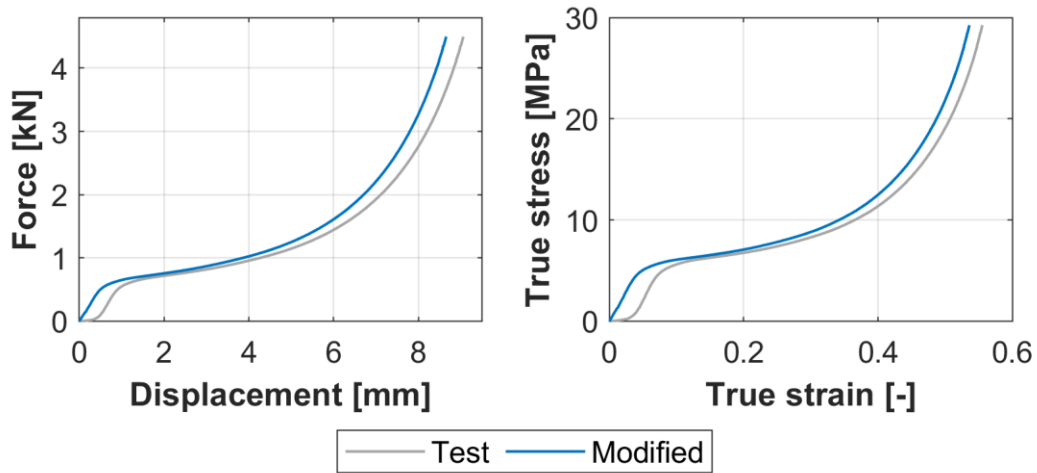


Figure 3.8: Two plots for material specimen 1i where (a) is force versus displacement, and (b) is true stress versus true strain. The grey line is experimental data, and the blue line is modified.

The same procedure was conducted for all the six specimens and Figure 3.9 and Figure 3.10 depicts the combined FD and true stress versus true strain graphs, respectively. Observations in the displayed force versus displacement indicate the same trend for all specimens when being subjected to uniaxial compression. The last transition from the plateau to the densification seems to differ extensively from specimen to specimen, but this is only partly true since there is a significant height difference in each specimen. The heights of the specimens vary with 20%, see two left columns in Table 3.3, which results in different timing for densification since the densification depends on %-strain of a corresponding specimen. Thus, 1o is seen to densify first of the specimens. Another important feature is the density difference in the specimens which has been enlightened previously in this chapter.

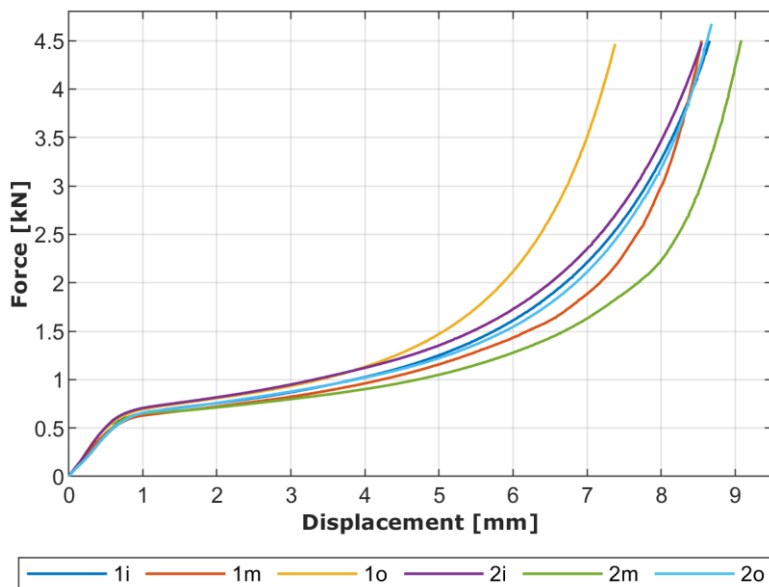


Figure 3.9: Force versus displacement for the material specimens.

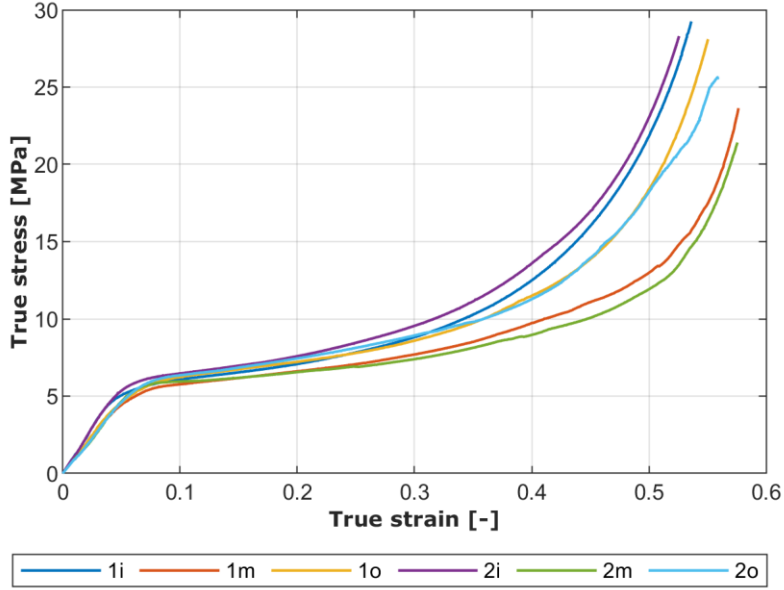


Figure 3.10: True stress versus true strain for all six material specimens.

Table 3.3 contains measured geometrical parameters, material properties as yield stress  $\sigma_0$ , yield strain  $\varepsilon_0$  and Young's modulus  $E$  for all six specimens along with how much each specimen was compressed at the final stage. The lower two rows include the average and standard deviation measurements, similar for the steel. In the table below it is observed that the spread is more varying, with the highest standard deviation for the Young's modulus of 12.5% and the lowest spread for the yield stress of 2.3%.

Table 3.3: PU material specimens' properties and dimensions.

ID	$h_0$ [mm]	$d_0$ [mm]	$\sigma_0$ [MPa]	$\varepsilon_0$ [-]	$E$ [MPa]	Compressed [%]
1i	12.2	11.78	5.0	0.049	125.1	71.0
1m	10.97	11.81	5.1	0.066	92.6	78.0
1o	10.06	11.82	5.4	0.066	98.3	73.3
2i	12.36	11.87	5.3	0.050	118.4	69.2
2m	11.68	11.73	5.4	0.062	94.0	77.7
2o	11.6	11.62	5.5	0.065	94.0	74.7
avg	11.48	11.77	5.3	0.060	103.7	74.0
STD	0.78	0.08	0.12	0.007	13.0	3.2

Yield stress and corresponding yield strain was obtained by inspection and correspond well with 0.2% offset yield strength. Even though the test is not designed to capture the elasticity modulus, it can be observed that the values found correlates well with the literature [23]. The average measurements stated in Table 3.3 corresponds well with values given in the datasheets provided by Equinor, see Datasheets. BASF [45], which is the world's largest chemical concern, has conducted the experiments to establish the values provided within the datasheets.

A discrepancy in the parameters can be observed from these measurements and might indicate poor results. However, this can be explained by the density variation as is seen in Table 3.1. Observe that the pair-grouping in the true stress versus true strain graph in Figure 3.10 corresponds with specimens location in radial thickness. Meaning that specimens 1i and 2i fits well together, 1m and 2m, and same goes for 1o and 2o. The properties within the grouping

are pretty similar which can be observed by a closer inspection of Table 3.3. This result indicates how important the density is for polyurethane foam’s mechanical properties.

### 3.4.3 Sandwich sample results

Uniaxial compression tests of the sandwich specimens were performed to investigate how the different layers of the coating interact, and most importantly, how the full thickness of porous PU behaves under compression loading. Limitations in available load cells resulted in the use of one with 250kN capacity.

All samples were subjected to yielding during the experiment, but to different displacements. Most of them were compressed until approximately 40kN, and some were stopped before. The samples which were stopped prior to total fracturing were initially supposed to be scanned in XRMCT to capture other properties of the porous polymer. This was not carried out due to unfortunate global events in the year 2020 and will not be discussed any further. Some of the samples fractured during compression so that material pieces cracked off, which is visible in Figure 2.6b. Five specimens, 12A, 12B, 3C, 6C and 9C, are chosen to represent all the tests. Once again, the number represents the clock position while A, B and C represent which of the three rings the sample is collected from.

Force versus displacement for the selected five samples is illustrated in Figure 3.11. All the samples follow the same trend and the differences can be explained by the size variation, see Table 3.4, along with some defects on the samples. Some of the samples had pieces fractured off prior to the testing due to the rough saw used to cut out the samples. However, in the plastic domain the specimens behave differently due to local fractures. A sudden drop in the force can be observed at multiple locations, and this corresponds to extensive cracking in the sample. Visual deformation during the compression tests for the selection of samples can be seen in Figure 3.12.

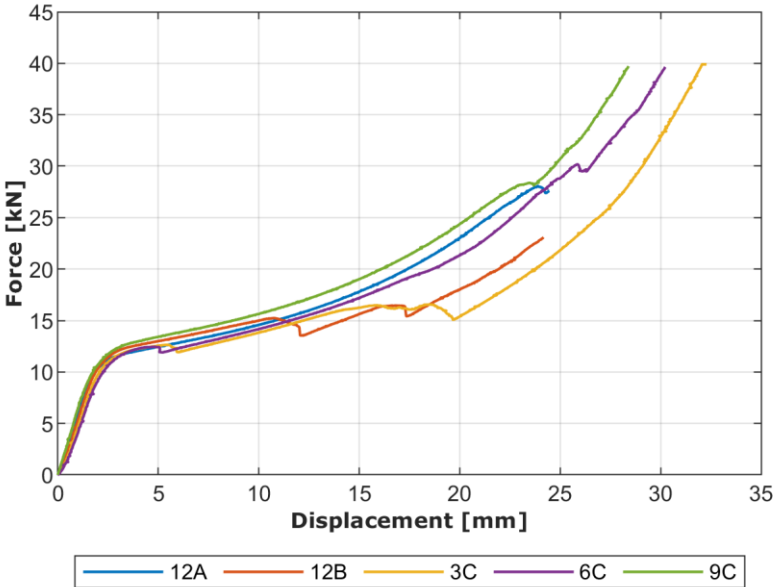


Figure 3.11: Force versus displacement for the selected five sandwich samples.



Table 3.4: Measured dimensions of the five selected sandwich samples.

ID	3C	6C	9C	12A	12B
$h_0$ [mm]	76.9	78.2	77.1	75.6	76.5
$w_z$ [mm]*	44.2	46.7	46.6	44.9	46.2
$w_\theta$ [mm]*	43.4	44.0	44.4	42.7	44.1

\*  $w_z$  is the width in the longitudinal direction, while  $w_\theta$  is the width in the hoop direction.

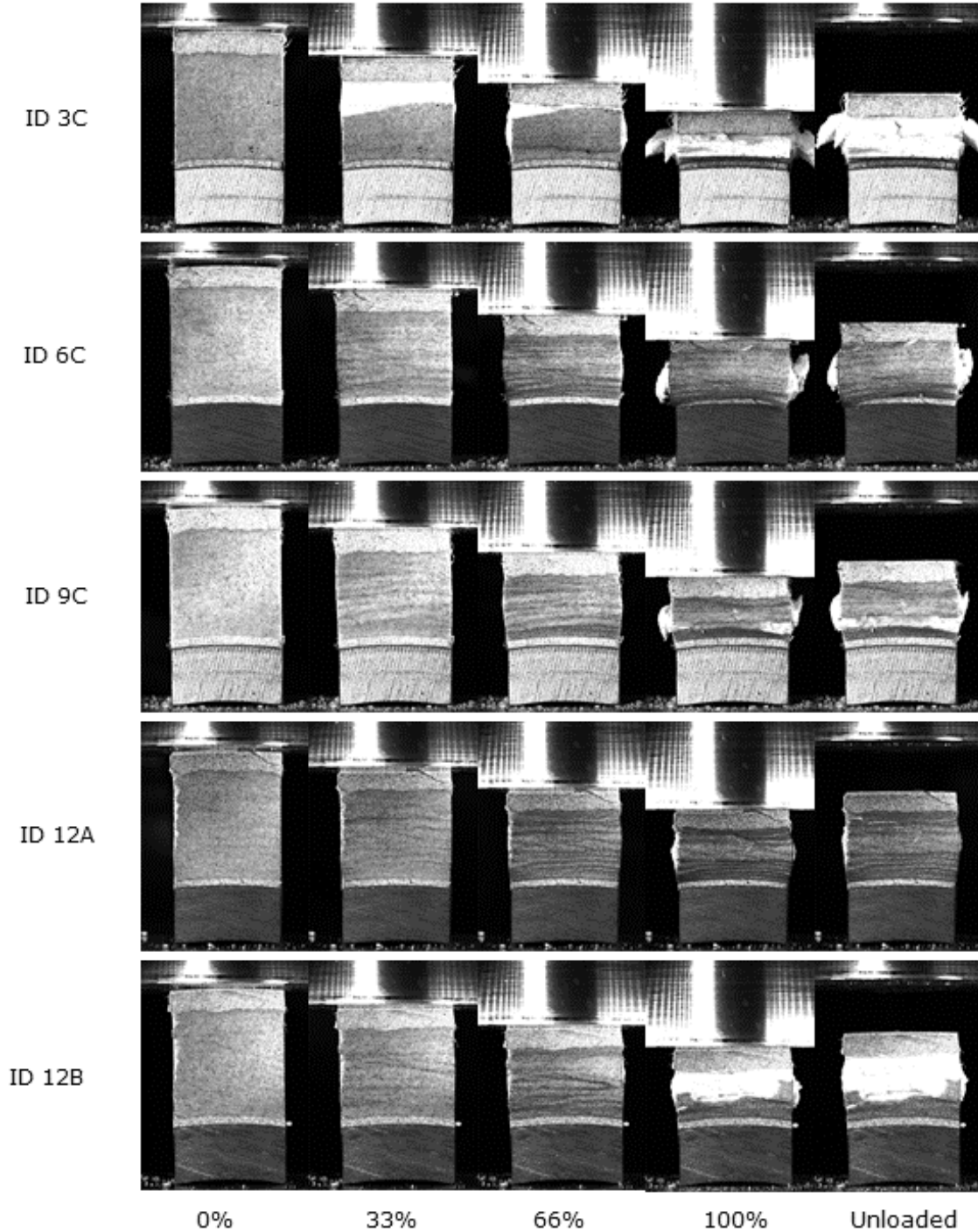


Figure 3.12: Deformation timeline of the selected five sandwich specimens. The images show displacement in % of total displacement for the respective specimen.

Note that Figure 3.12 shows deformation of the samples relative to the current sample's total deformation which can vary between the specimens. Where the samples are extremely bright, i.e. when 3C is unloaded, the sample has fully opened due to cracking. This indicates how brittle the PU foam is and how much it cracked during testing.

Similar to the material specimens, the sandwich samples also started to fracture around the yielding point. The fracturing was much more significant in this experiment due to high barrelling effect in the PU part of the specimen since almost all contraction occurred in this region. Recalling that the specimens initially were cubic, the corners will experience high strains and crack more easily compared to the cylinder specimens. As a result of the barrelling, the material cracked up and material pieces broke off. On the same side, this effect can be explained by the rise of friction in contacting regions between the sandwich sample and machine since no lubrication was applied.

Post observation of compressed sandwich samples indicated that the protective outer polypropylene layer was no longer attached to the sample. This phenomenon was also observed during the denting of the pipe and will be described here, and it is visible in Figure 3.16. Although this is an important property of the interaction between the layers, it will not be accounted for in the numerical model due to complexity and the lack of necessary properties.

### 3.5 Quasi-static denting of pipe results

As specified in DNV GL's recommended practice [5], an operating pipeline must be shut down if the permanent outer deformation of the steel exceeds 5% of the external diameter of the steel. Including both elastic and plastic deformation, this yields approximately 21mm outer deformation of the steel for both pipes. As the steel is assumed to contract negligible during deformation beneath the indenter, it is fair to look at the internal deformation,  $u_i^{\dagger}$  which is defined in Figure 3.13. Since this displacement is one of the outputs recorded during testing, the experiments were conducted until at least  $u_i^{\dagger} > 21\text{mm}$  for all tests. The internal deformation is measured by a laser for the experiments, thus  $u_i = u_i^{\dagger}$ . Outer displacement is defined as  $u_o$ , while  $u_i^{\flat}$  is the bottom inner displacement due to fracturing of the coating system close to the rigid support. The latter displacement is needed to describe how much the coating gets crushed during the test.s

The force versus displacement from the experiments can be seen in Figure 3.14 and Figure 3.15, with the big and small indenter, respectively. Both figures consist of two subplots where the upper is force versus outer deformation, while the lower is force versus inner displacement. The difference between the big and small indenter is significant when it cuts through the coating before the indenter hits the steel pipe. The smaller indenter will engage a smaller area of the coating and thus penetrate the coating with less force. After contact with the steel, the behaviour is very similar. The pipe is compressed between the indenter and a rigid support along the longitudinal direction of the pipe. This deforms the coating system on the bottom of the pipe which can be seen in Figure 3.16a-c. This is not a realistic scenario as the seabed is usually not rigid [3], and impact from trawl gear will probably hit a pipeline span with no support on the opposite side. The boundary condition of the pipe will be described in more detail in Section 5.5.



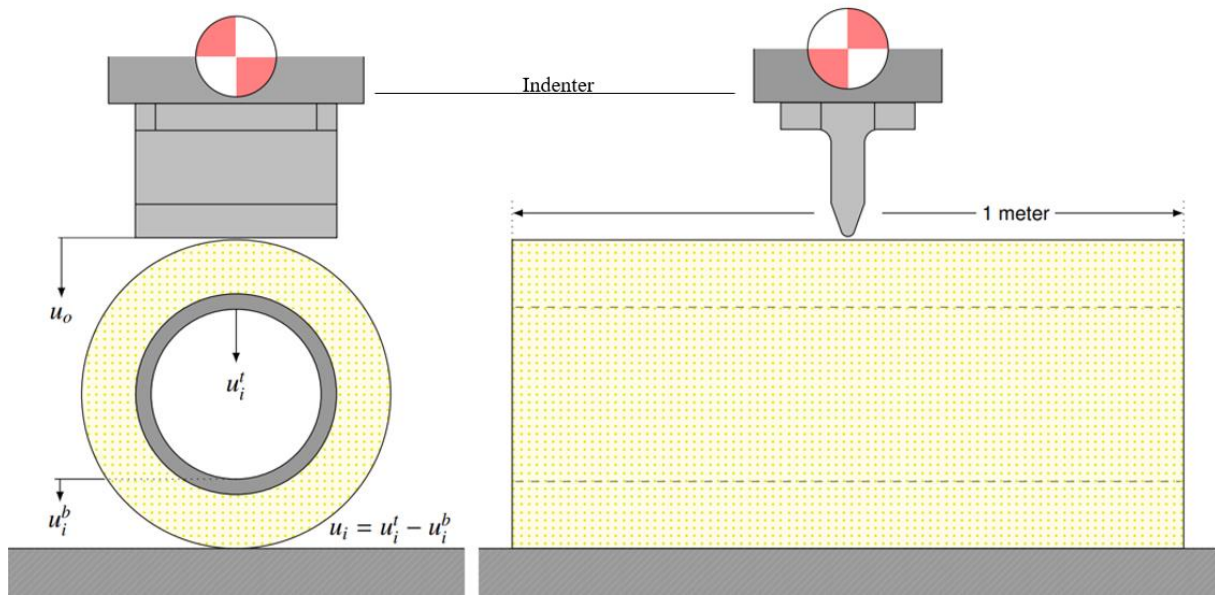


Figure 3.13: Schematic illustration of pipe being dented [3].

The retest with both indenters shows an almost identical response with respect to force versus outer displacement to the initial test, even though the coating system cracked during the first test. It should be observed that the internal stiffness is reduced on both retests, see force versus inner displacement in the two following figures. However, all four tests show valid response with the same trends when subjected to quasi-static load cycles.

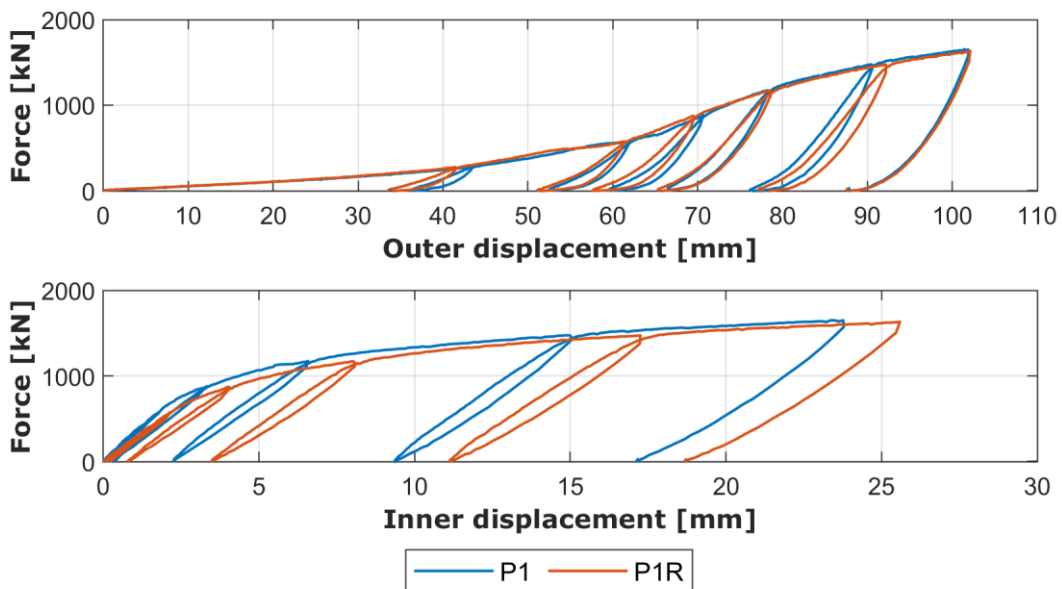


Figure 3.14: Force versus displacement for the big indenter. Upper: outer displacement and lower: inner displacement.

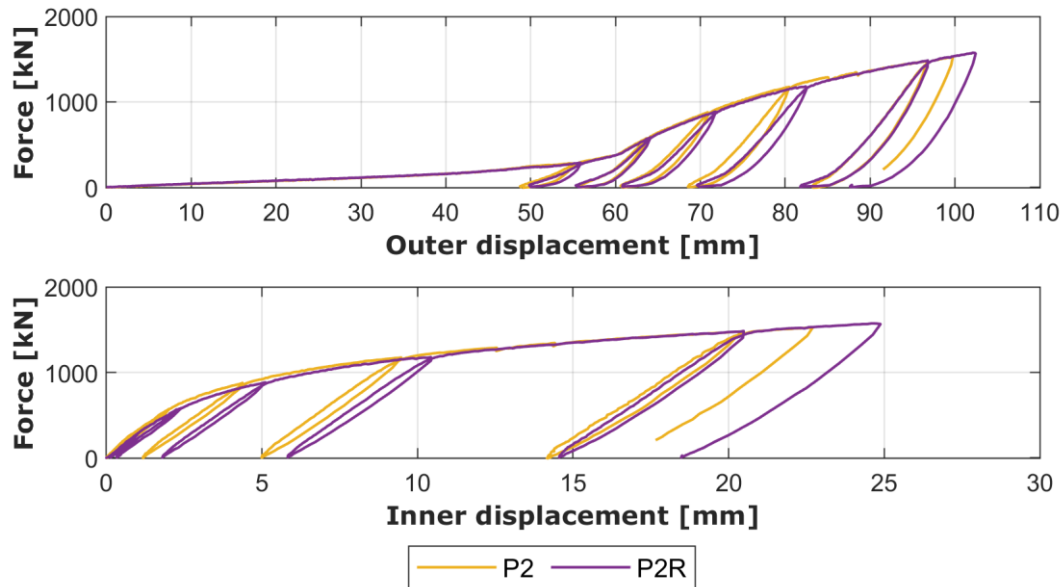


Figure 3.15: Force versus displacement for the small indenter. Upper: outer displacement and lower: inner displacement.

Several important observations were made both during and after the tests were carried out, and the main ones will be described following the force versus displacement with small indenter, Figure 3.15. Noise was heard early and throughout the experiment and was assumed to be cracking in the PU part of the coating system in the indentation zone. When the outer displacement starts reaching 50mm, the protective outer layer (PP) is subjected to extreme strains in the indentation zone and allegedly cracks open. This can be seen in Figure 3.16d-f. The coating system being crushed at its bottom half towards the plate, Figure 3.16a-b, is the next major incident which results in low slope in the force when  $u_o$  is  $\epsilon[55\text{mm}, 60\text{mm}]$ . Up until this point,  $u_o \leq 60\text{mm}$ , almost all deformation has been in the indentation zone and some at the opposite side towards the rigid support. For the rest of outer displacement ( $u_o$  is  $\epsilon[60\text{mm}, \sim 100\text{mm}]$ ), the deformation is somewhat 50/50 distributed to the steel and crushing of coating towards the rigid support. The indentation zone is extremely local and can be seen in Figure 3.16d-f. This local indentation zone yields similar trends for the pipes being subjected to the big and small indenter. As the big indenter's local zone is much bigger, it does not cut as easily in the protective layer compared to the smaller indenter, thus the crushing on the opposite side is seen earlier and the stiffness is increased prior to engaging the steel.

Similarities to uniaxial compression of the sandwich samples are seen with respect to only observing crushing in the PU part of the coating system. The interaction between the PU layer and towards both its inner and outer PP layer is seen to no longer be attached at several places, as seen in Figure 3.16a-c after being quasi-statically dented.

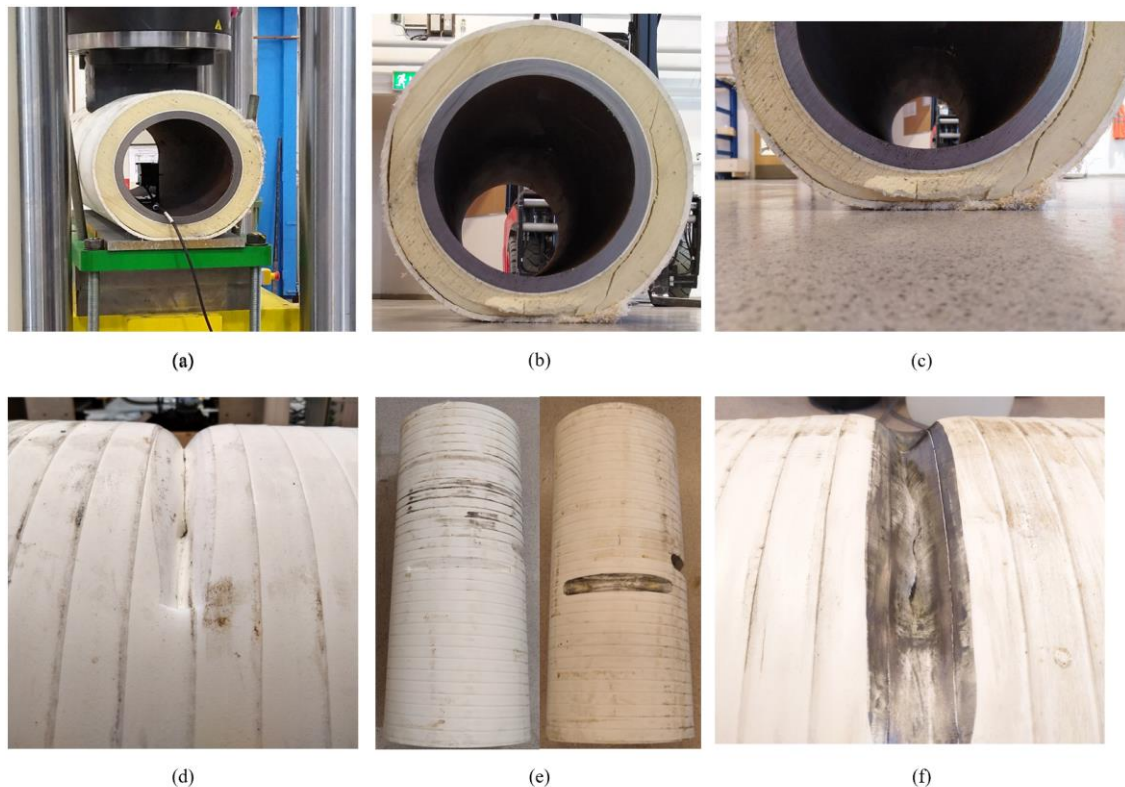


Figure 3.16: (a) First test of P1, (b) and (c) showing the cracks in the PU layer after denting. (d) Indentation zone by the small indenter. (e) Top view of both indentation zones, small indenter on the left side, and (f) Indentation zone by the big indenter.

### 3.5.1 The absorbed energy of the pipes

The quasi-static denting of the pipes provided data for force, outer displacement, and inner displacement directly underneath the indenter as described previously. Work done on the pipe by the indenter can be calculated from this set of data and will be referred to as the absorbed energy of the pipe. It is of interest to find the amount of energy necessary to create a permanent dent of the steel, and how much of this energy that is absorbed by the coating and steel, separately.

Since the quasi-static denting was performed in cycles of approximately 300kN, it was necessary to combine the cycles into one continuous curve to calculate the work i.e. the area under the force versus displacement curve. This is done by creating a straight line between the top of each cycle and connecting it to the next cycle, where it is likely the curve would have continued without sectioning into load cycles.

The adjustment for P1 can be seen in Figure 3.17, and from this result, it is possible to numerically integrate the curve to find the work done by the indenter. Here, MATLAB's trapezoidal method has been used to calculate the area defined by the continuous graph and x-axis [46]. This area corresponds to the work done on the pipe, and the total absorbed energy (blue) computed for P1 is presented in Figure 3.18. It is here assumed that the entire deformation in the steel is localized beneath the indenter, so that the integral of the force versus inner displacement is approximately the energy absorbed by the steel pipe. Using these simplifications, the energy can be separated into energy absorbed by the steel (yellow) and the

polymer coating (red). At the end of the compression, the steel and PU coating has absorbed almost the same amount of energy as can be seen in Figure 3.18.

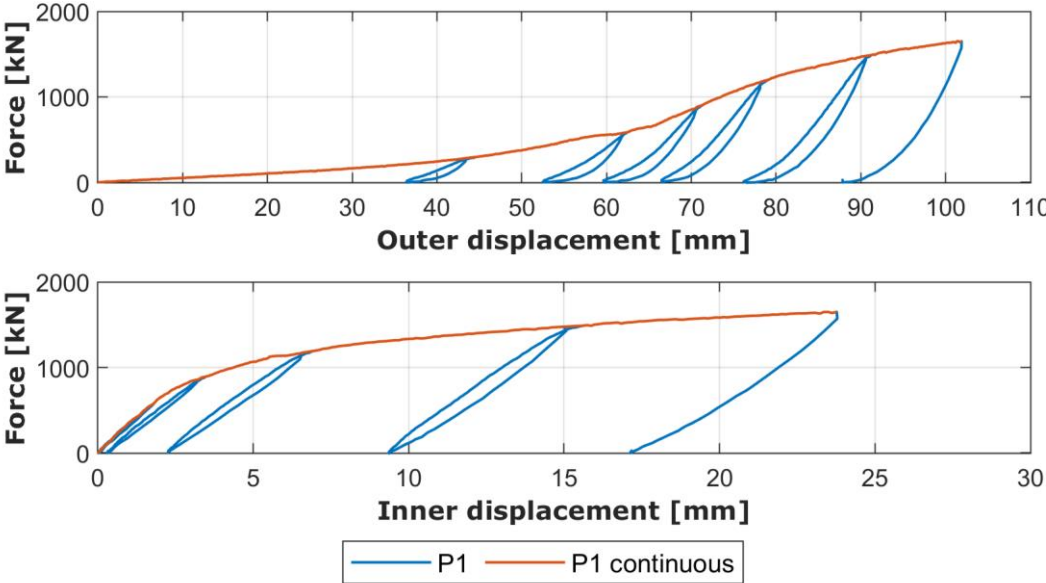


Figure 3.17: Force versus displacement for P1 made continuous across the load cycles. Upper being outer displacement and lower being inner displacement.

As mentioned previously, it is here assumed that the outer displacement of the steel pipe is equal to the inner displacement of the steel pipe since neglectable contraction will occur in the steel in the indentation zone. From the recommended practice [5] the allowable permanent deformation of the outer diameter of the steel pipe must be smaller than 5%, resulting in a maximum permanent dent depth of 16.2mm. The force needed to permanently dent the steel 16.2mm is found to be 1635.4kN for P1. This is found at the intersection point between the force versus inner displacement curve and its linear elastic curve starting with zero force at  $x = 16.2\text{mm}$ , see Figure 3.19. The found force corresponds to a unique point in the force versus outer displacement plot as well, thus the total, coating and steel’s work can be calculated. The same method is utilised to calculate the energy needed to create a permanent dent size of 0.07% of the steel’s outer diameter, which can be approximated as the energy absorbed by the polymer

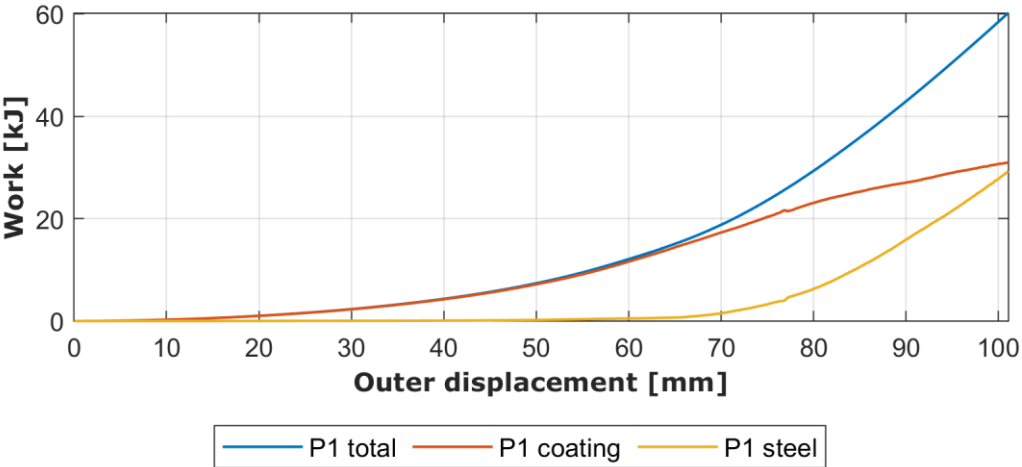


Figure 3.18: Work done by the indenter on P1 separated into contributions from coating and steel.

coating before any permanent damage is done to the steel pipe. 0.07% is chosen since this is the same value used by Vestrum [3] to calculate work done by the indenter prior to permanent damage to the steel pipe.

By inspecting the force versus inner displacement curve, the elastic deformation is noticeable from the cycles as the pipe is unloaded. After unloading, the change of inner displacement of the pipe is measured to be 4.33mm, 5.62mm and 6.65mm for cycle 4, 5 and 6, respectively. This implies that the elastic stiffness is lowered as the experiment is performed due to decreased contribution from the coating towards the rigid support. This is also seen when calculating the slopes and is accounted for in the figure below.

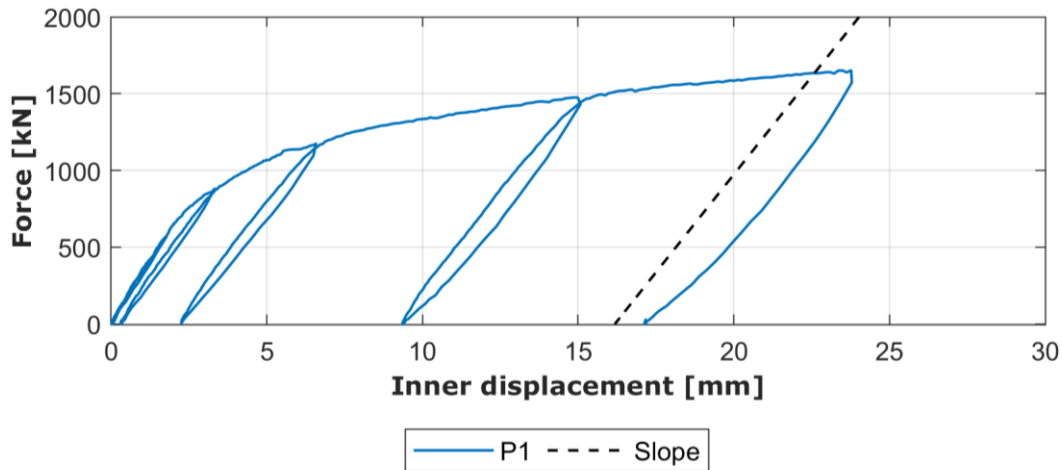


Figure 3.19: The estimation of the force needed to permanently dent the pipe 5% of outer steel diameter.

Table 3.5 shows measurements for the four component tests, including max force  $F_{\max}$ , max inner and outer displacement  $u_{i\max}$ ,  $u_{o\max}$  in the left three columns. Following two columns includes the total work  $W_{0.07\%}$  and  $W_{5\%}$  done on the pipe to obtain permanent inner displacement of 0.07% and 5% of the steel's outer diameter, respectively. The last column is the maximum total work  $W_{\max}$  done on the pipe corresponding to  $F_{\max}$ .

Table 3.5: Force, displacements and work measurements for denting of pipe tests.

Test	$F_{\max}$ [kN]	$u_{i\max}$ [mm]	$u_{o\max}$ [mm]	$W_{0.07\%}$ [kJ]	$W_{5\%}$ [kJ]	$W_{\max}$ [kJ]
P1	1651	23.8	101.9	18.2	58.7	61.5
P1R	1634	25.6	102.1	15.2	57.2	62.2
P2	1528	22.7	99.8	11.0	50.1	51.1
P2R	1575	24.6	102.1	9.7	49.5	54.1

Total work done on the coated pipes with permanent deformation of 5% of the steel's outer diameter  $W_{5\%}$  are in approximately 59kJ for the big indenter and 50kJ for the small indenter. Since the estimated maximum kinetic energy expected from impacting objects is about 40.5kJ [5], the pipeline design investigated in this thesis is capable of withstanding this impact load without causing an indentation above 5% of outer steel diameter. For the case of P1, the permanent deformation at  $W = 40.5\text{kJ}$  is 4.1% of the outer steel diameter.

Prior to permanent deformation  $W_{0.07\%}$  indicates that the coating absorbs 41.2% and 25.6% of the maximum expected energy of 40.5kJ for the big and small indenter, respectively. In Figure

3.16 it was observed that the small indenter engaged a much smaller area compared to the big indenter and as a result, this is seen in the different capacities to absorb energy. With respect to the coating's ability  $W_{0.07\%}$ , the pipe subjected to the small indenter absorbs 38% less compared to the pipe subjected to the big indenter. Another important feature is to observe the reduced capacity in the retest of both pipes. The absorbed energy done by the coating prior to permanent deformation for the retests is reduced with 16.5% and 11.8% for the big and small indenter, respectively. *P1R* has reduced capacity compared to *P2R* since *P1* is more globally damaged than *P2* due to different indenter sizes. Comparing the reduced capacity at  $W_{5\%}$ , the difference is minor since the steel contributes significantly in the total absorbed energy.

### 3.6 Comparing PU and PP results

Polyurethane-coated steel pipes have in this thesis been quasi-statically compressed to investigate how it behaves during quasi-static loading and the amount of work required to plastically deform the steel pipe to a max allowable dent size. Vestrum [3] performed the same experiments to polypropylene-coated pipelines in addition to dynamic experiments to estimate the severity of impact loads to the polymer-coated pipeline. Impact loads are associated with kinetic energy transferred from the impacting object to the pipeline. The impact time is often so short that the energy transferred is absorbed as local deformations. The amount of energy transferred to the pipe coating generally depend on the shape of the impacting object, the pipe diameter and span, and the impact direction. The consequences of impact loads can be severe both environmentally and economically. An impact load can cause permanent denting which could prevent operations of internal inspection vehicles. A dent can also cause a collapse in the pipeline, but this failure mode should only occur during phases of external overpressure, which may apply during installation or loss of internal pressure. A dent can also create a stress concentration in the impacted area which could lead to fracture by fatigue [5]. The most severe result of an impact load, however, is fracture of the steel pipeline which could cause enormous environmental pollution.

Earlier work [1, 2, 3] has investigated the effect of impact loads towards polypropylene-coated pipelines manufactured by Shawcor [47], while this thesis has investigated polyurethane-coated pipelines manufactured by Logstor [31]. The two coating materials have different material properties, in addition to the difference in the porosity of the coating which is significant. The relative density of the coating materials varies in the thickness direction of the coating, which affects the mechanical properties. However, the average mechanical properties of the coatings are presented in Table 3.6 (Table 5.1 in [1]). The relative density in the polypropylene coating varies from 1 to 0.7 [34], while the polyurethane coating has a lower relative density of approximately 0.28. This significant difference in porosity can be seen as the PU has a more significant plateau region in its stress versus strain curve. The elastic parameters  $E$ ,  $\sigma_0$  are much higher for the porous PP compared to PU and the result of this is seen in the coated pipeline's ability to absorb energy, which will be described at the end of this section.



Table 3.6: Selected material properties of PU and PP [1].

Material	$\rho_{\text{measure}} \left[ \frac{\text{g}}{\text{cm}^3} \right]$	$E$ [MPa]	$\sigma_0$ [MPa]
Polyurethane	0.336	104	5.3
Polypropylene	0.730	401	6.8

XRMCT results from the polypropylene and polyurethane coating show the variation of relative density in the materials. Figure 3.4 shows the variation of relative density in the thickness direction of the polyurethane coating. Compared to the XRMCT results for the polypropylene coating from Vestrum [34], the PU coating shows a more “constant” relative density in the interval 0.26 – 0.36 throughout the thickness, while PP exhibits a more defined curved density distribution as displayed in Figure 3.20, from 1 in the innermost and outermost layers to roughly 0.7 in the mid layer.

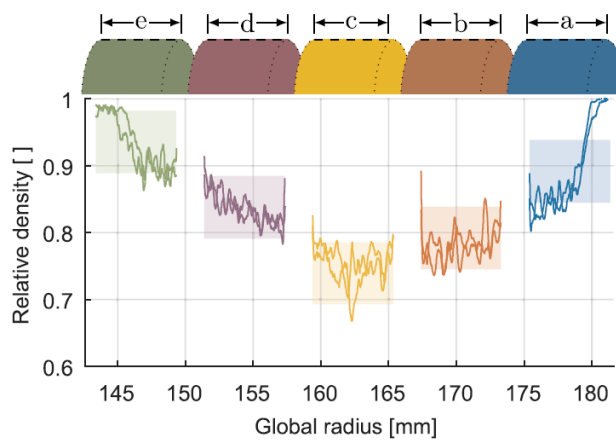


Figure 3.20: Relative density over the thickness of the polypropylene coating investigated by Vestrum in [34].

The difference in the distribution of gas pockets in the coating can be seen in Figure 3.21. Where the polypropylene has fewer, but larger gas pockets, the polyurethane coating has small, but significantly more gas pockets. Some straight lines are noticeable in the PU material specimen. This might be caused by the manufacturing process where the PU coating is sprayed on the steel pipeline. This creates a visible boundary between material and non-material and may affect the mechanical properties of the PU coating, which is not visible for the PP coating.

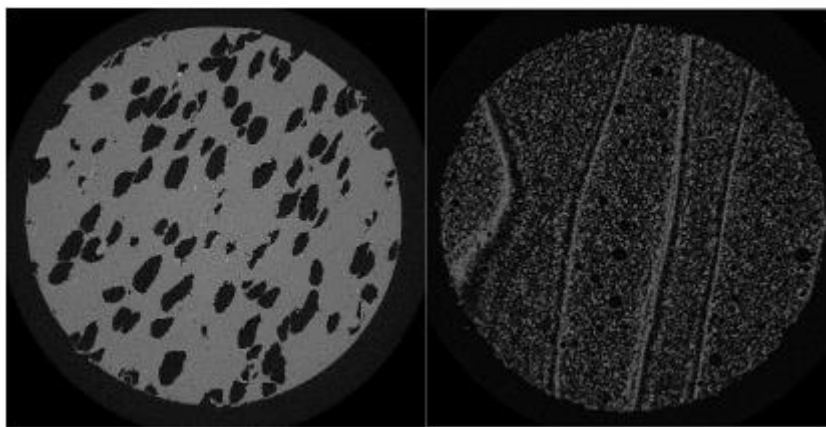


Figure 3.21: (a) Mid cross-section PP [Figure 4.8 in [2]], and (b) is the cross-section of PU, both acquired from XRMCT.

The geometry of the polypropylene-coated pipelines and the polyurethane-coated pipelines are different both in terms of the steel and polymer coating thickness and radius. This affects the

results when comparing the component tests. Figure 3.22 shows the geometry of the PP-coated pipelines tested by Vestrum [3]. The PP-coated pipeline designs consist of a combination of solid and porous PP, while the PU-coated pipeline design consists of a combination of porous PU and an inner and outer layer of solid PP. During the component test of the PU pipeline, the outer PP layer was eventually separated from the PU coating as can be seen in Figure 3.16. This behaviour was not seen in the PP-coated pipelines. The component tests of the PU-coated pipelines were conducted with a similar quasi-static experimental setup as Vestrum [3], with principally identical boundary conditions. Vestrum [3] only used one indenter for the setups, which is the same as referred to as the small indenter in this thesis.

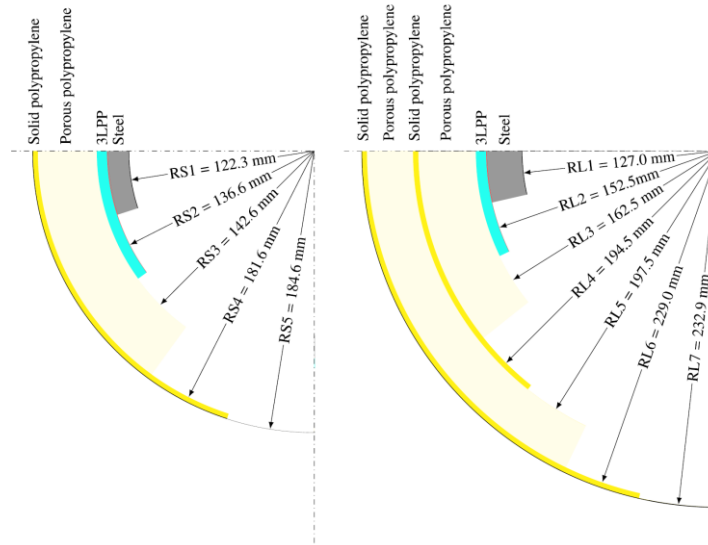


Figure 3.22: Geometry of the PP pipeline designs tested by Vestrum [3] (a) is Pipe S and (b) is pipe L.

At a permanent dent depth below 0.07%, the PP pipeline designs reach work values of around 25kJ and 60kJ for the small and large PP pipeline designs, respectively [3]. In comparison, the PU pipeline design reaches a work value of about 11kJ with the same indenter. The thickness of the polymer coating of the PU pipeline is about 54mm, which lies between the two PP pipeline coating thicknesses of 48.0mm and 80.4mm. Still, the PU pipeline design reaches considerably lower work values than the smallest PP coating. Before any permanent internal deformation is seen, the PP coating absorbs significantly more energy than the PU coating. This is expected as the PU coating is much more porous than the PP coating. For the pipeline design as a whole, the small and large PP pipelines reach work values around 43kJ and 116kJ, respectively, at permanent dent depth of 5% [3]. In comparison, the PU pipeline reaches work values of approximately 46kJ at a permanent dent depth of 5% of the inner steel diameter. Note that 5% of the inner steel diameter has been used here to compare the results by Vestrum [3] to the PU pipeline design, which was measured in dent depth of inner steel diameter. Table 3.5 shows values for 5% of the outer steel diameter.



# Chapter 4

## Calibration of material models

Constitutive models will be calibrated from the state variables, stress and strain. Steel and porous polyurethane behave very differently when subjected to loading, which motivates two different material models. The models' theory will be presented in the following section with an extra effort of deducing Deshpande and Fleck's (DF) yield criterion [27]. A selection of important aspects with finite element analysis (FEA) will be introduced prior to calibrating constitutive models in the numerical material models of the UT and UC tests.

### 4.1 Formulation

Definitions, formulations and general expressions given in lecture notes in [41, 42, 43], combined with the article [27] by Deshpande and Fleck (DF) will be utilised in the following formulation. Einstein's tensor notation will be adopted herein, and the reader is referred to [41] for details. Lamé constants  $\mu$  and  $\lambda$ , Kronecker delta  $\delta_{ij}$ , other well-known definitions and mathematical operations used in this subchapter is defined in Appendix D.

The hypoelastic-plasticity formulation may be adapted since the materials (steel and PU) studied herein are assumed isotropic. Further, observations from the experimental results implies small elastic strains, while the plastic strains and rotations may be finite. Additive decomposition of the rate-of-deformation tensor  $D_{ij}$  is adopted as

$$D_{ij} = D_{ij}^e + D_{ij}^p \quad (4.1)$$

where  $D_{ij}^e$  and  $D_{ij}^p$  are the elastic and plastic parts, respectively. The elastic part is defined in terms of the elastic constants: Poisson's ratio  $\nu$  and Young's modulus  $E$ , and Jaumann stress rate  $\sigma_{ij}^{\Delta J}$  (defined in Appendix D) of the Cauchy stress tensor  $\sigma_{ij}$ , viz.

$$D_{ij}^e = \frac{1 + \nu}{E} \sigma_{ij}^{\Delta J} - \frac{\nu}{E} \text{tr}(\sigma_{ij}^{\Delta J}) I_{ij} \quad (4.2)$$

$I_{ij}$  is the second-order unit tensor. Applying associated flow rule, the plastic rate-of-deformation tensor is defined with the plastic multiplier ( $0 \leq \dot{\lambda}$ ) and yield function  $f$  as

$$D_{ij}^p = \dot{\lambda} \frac{\partial f}{\partial \sigma_{ij}} \quad (4.3)$$

where the adopted form of yield function  $f$  is given as

$$f(\sigma_{ij}, R) = \Phi(\sigma_{ij}) - \sigma_Y(R) \quad (4.4)$$

In this thesis, the materials are assumed to be pressure- and temperature insensitive which reduces the flow stress (yield stress)  $\sigma_Y$  of the material to only be dependent on the initial yield stress  $\sigma_0$  and hardening variable  $R$ . Herein,  $R$  is the isotropic hardening variable which is dependent on the equivalent plastic strain  $p$ . The generic function  $\Phi$  will in the following be defined equal to the equivalent stress  $\sigma_{eq}$ ,  $\Phi \equiv \sigma_{eq}$ . When Equation (4.4) is less than zero ( $f <$

0), the material is said to be in the elastic domain, and when  $f = 0$  the material is said to yield.  $f = 0$  defines the yield surface and  $f > 0$  is admissible [41]. Thus, the material's yield criterion is given as  $f = 0$ . In Kuhn-Tucker form, the plastic loading/unloading is formulated as

$$f \leq 0, \quad 0 \leq \dot{\lambda}, \quad \dot{\lambda}f = 0 \quad (4.5)$$

with a consistency condition viz.

$$\dot{\lambda}\dot{f} = 0 \quad (4.6)$$

The equivalent stress can be expressed equal to the flow stress by solving Equation (4.4) ( $f = 0$ )

$$\sigma_{\text{eq}} = \sigma_Y \quad (4.7)$$

First, the steel will be fitted with a Bridgman-LeRoy (BL) correction [48] of the true stress obtained from the experiment. The flow stress will be estimated using the original Johnson-Cook (JC) constitutive model [43]. Lastly, a derivation to obtain Deshpande and Fleck's equivalent stress [27] to be used as a constitutive model for the polyurethane foam.

#### 4.1.1 Constitutive relation of steel

When the load in the tensile test reaches its maximum i.e. when  $dF = 0$ , necking will occur in the specimen which introduces a complex triaxial stress state. This phenomenon gives radial and transverse stresses which will increase the value of the longitudinal stress required to cause plastic flow [43]. Thus, the true stress needs to be corrected for these effects. Bridgman-LeRoy correction can be used to obtain the equivalent stress  $\sigma_{\text{eq}}^{\text{BL}}$  after necking. Equation (4.8) shows how the equivalent stress can be obtained.  $\varepsilon_1^{\text{p}}$  is the true plastic strain and  $\varepsilon_{\text{lu}}^{\text{p}}$  is the true plastic strain at the necking point.

$$\sigma_{\text{eq}}^{\text{BL}} = \frac{\sigma_t}{\left(1 + \frac{2R}{a}\right) \ln \left[1 + \frac{a}{2R}\right]} \quad (4.8)$$

where

$$\frac{a}{R} = 1.1(\varepsilon_1^{\text{p}} - \varepsilon_{\text{lu}}^{\text{p}}) \quad (4.9)$$

The assumptions made for the steel is isotropic material behaviour, isochoric plastic deformations, yielding independent of hydrostatic pressure and quasi-static or dynamic loading [43]. Thus, the rate-dependent  $J_2$  flow theory is adopted, yielding von Mises equivalent stress  $\sigma_{\text{eq}}^{\text{vM}}$  to be [41, 42]

$$\sigma_{\text{eq}}^{\text{vM}}(\sigma_{ij}) = \sqrt{3J_2} = \sqrt{\frac{3}{2} \sigma'_{ij} \sigma'_{ij}} \quad (4.10)$$

and the deviatoric part of the Cauchy stress tensor is defined as  $\sigma'_{ij} = \sigma_{ij} - \frac{1}{3} \sigma_{kk} \delta_{ij}$ . It can be shown that  $\dot{p} = \dot{\lambda}$  in  $J_2$  flow theory [41], associated flow rule (Equation (4.3)) and equivalence in plastic power (i.e.  $\sigma_{ij} D_{ij}^{\text{p}} = \sigma_{\text{eq}} \dot{\lambda}$ ) are used. Here, the conjugate to the equivalent stress is the equivalent plastic strain-rate  $\dot{p}$  [3]. A plasticity model based on the same assumptions is the well-known Johnson-Cook material model. For further reading about JC plasticity, the reader is referred to [43]. The motivation for establishing the flow stress using JC is because this model

is implemented in Abaqus. The JC plasticity model without temperature and strain-rate dependence is presented in Equation (4.11) with its customary form. Since the uniaxial tension tests were performed quasi-static it is assumed no strain-rate dependence and no adiabatic effects were present.

$$\sigma_Y = A + Bp^n \quad (4.11)$$

In Equation (4.11)  $A = \sigma_0$  and a power law  $Bp^n$  has been used for the work-hardening term  $R(p)$ . ( $A, B, n$ ) are material parameters and  $0 \leq p$ , where  $p$  is equivalent plastic strain.

#### 4.1.2 Constitutive relation of polyurethane

Deshpande and Fleck proposed two phenomenological isotropic constitutive models for the plastic behaviour of aluminum foams [27]. Their initial model assumes that the yield function  $f$  is independent of the third stress invariant  $J_3$  and that the yield function is even with respect to the mean stress  $\sigma_m$ .  $J_3$  is defined in Appendix D. This material model has been approved for different cellular materials. Deshpande and Fleck verified it for ductile PVC foam in [49], and Vestrum obtained good results on porous PP by modifying this model to be pressure sensitive related to the porosity level [3]. The derivation of Deshpande and Fleck's equivalent stress is motivated since this model is also included in Abaqus.

With the assumption of isotropic elastic material, the generalized Hooke's law may be given as in Equation (4.12). See [41] on how to establish this expression.

$$\sigma_{ij} = K\varepsilon_v\delta_{ij} + 2G\varepsilon'_{ij} \quad (4.12)$$

Where  $K = \lambda + \frac{2}{3}\mu$  and known as the bulk modulus, while  $G = \mu$  and is the shear modulus. The volumetric strain is introduced as  $\varepsilon_v = \varepsilon_{kk}$ , and the strain tensor  $\varepsilon'_{ij}$  (defined in Appendix D) has been used. By rearranging the stress tensor  $\sigma'_{ij}$  stated earlier and introducing hydrostatic stress  $\sigma_H = \frac{1}{3}\sigma_{kk}$  ( $= \sigma_m$ ) we obtain the following

$$\sigma'_{ij} = 2G\varepsilon'_{ij} \quad \wedge \quad \sigma_H = K\varepsilon_v \quad (4.13)$$

Formulating the strain-energy function  $U_0$  to be dependent on the strain  $\varepsilon_{ij}$  such that  $\sigma_{ij} = \frac{\partial U_0}{\partial \varepsilon_{ij}}$ , the material is said to be hyperelastic. It can be shown that the 4<sup>th</sup> order tensor of elastic constants  $C_{ijkl}$  (defined in Appendix D) is both minor and major symmetric with the assumptions made [41], and the strain-energy function can be expressed as

$$U_0 = \frac{1}{2}C_{ijkl}\varepsilon_{ij}\varepsilon_{kl} = \frac{1}{2}\sigma_{ij}\varepsilon_{ij} \quad (4.14)$$

Inserting Equation (4.12) into Equation (4.14) to obtain

$$U_0 = G\varepsilon'_{ij}\varepsilon'_{ij} + \frac{1}{2}K\varepsilon_v^2 \quad (4.15)$$

Rearranging Equations (4.13) with respect to  $\varepsilon'_{ij}$  and  $\varepsilon_v$ , and then inserting this into Equation (4.15) to obtain the strain-energy function in terms of the stress

$$U_0 = \frac{1}{4G}\sigma'_{ij}\sigma'_{ij} + \frac{1}{2K}\sigma_H^2 \quad (4.16)$$

Now define a critical value of the strain-energy function  $U_0^c$  which correspond to the material yielding. Thus, yielding occurs when

$$U_0^c(= U_0) = \frac{1}{4G} \sigma'_{ij} \sigma'_{ij} + \frac{1}{2K} \sigma_H^2 \quad (4.17)$$

Recalling von Mises equivalent stress given in Equation (4.10), the square can be found in Equation (4.17) by multiplying it with a factor of  $6G$

$$6GU_0^c = \frac{3}{2} \sigma'_{ij} \sigma'_{ij} + \frac{3G}{K} \sigma_H^2 = \sigma_{\text{eq}}^{\text{VM}^2} + \alpha^2 \sigma_H^2 \quad (4.18)$$

where the parameter  $\alpha^2$  will be commented at the end of this derivation, and is defined as

$$\alpha^2 = \frac{3G}{K} = \frac{9(1-2\nu)}{2(1+\nu)} \quad (4.19)$$

Rearrange Equation (4.18) to express the critical value of the strain-energy function as

$$U_0^c = \frac{1}{6G} \left( \sigma_{\text{eq}}^{\text{VM}^2} + \alpha^2 \sigma_H^2 \right) \quad (4.20)$$

Need to find another expression for  $U_0^c$ . Consider a state of uniaxial compression, since this is the state the PU material specimens will be subjected to. In this state, the only non-zero stress is  $\sigma = \sigma_{11} < 0$ , and the deviatoric and hydrostatic stresses are

$$\sigma'_{11} = \frac{2}{3} \sigma_{11} \quad , \quad \sigma'_{22} = \frac{1}{3} \sigma_{11} = \sigma'_{33} \quad , \quad \sigma_H = \frac{1}{3} \sigma_{11} \quad (4.21)$$

In 1D state of stress, the strain-energy function in Equation (4.14) reduces to

$$U_0 = \frac{1}{2} \sigma_{11} \varepsilon_{11} = \frac{1}{2E} \sigma^2 \quad (4.22)$$

The equivalent stress is  $\sigma_{\text{eq}} = \sigma$ , and at plastic yielding where  $f = 0$ , the stress state is equal to the yield stress, such that this yields the critical value of the strain-energy function

$$U_0^c = \frac{1}{2E} \sigma_{\text{eq}}^2 \quad (4.23)$$

Now, insert for  $G$  in Equation (4.20), insert the result into Equation (4.23) and rearrange to be expressed in terms of  $\sigma_{\text{eq}}^2$

$$\sigma_{\text{eq}}^2 = \frac{2(1+\nu)}{3} \left( \sigma_{\text{eq}}^{\text{VM}^2} + \alpha^2 \sigma_H^2 \right) \quad (4.24)$$

Use that  $\alpha = \alpha(\nu)$  to express Equation (4.24) in with only three different parameters

$$\sigma_{\text{eq}}^2 = \frac{1}{\left(1 + \left(\frac{\alpha}{3}\right)^2\right)} \left( \sigma_{\text{eq}}^{\text{VM}^2} + \alpha^2 \sigma_H^2 \right) \quad (4.25)$$

Taking the square root of the last expression to obtain a function for the equivalent stress

$$\sigma_{\text{eq}}^{\text{DF}} \equiv \sigma_{\text{eq}} = \frac{1}{\sqrt{\left(1 + \left(\frac{\alpha}{3}\right)^2\right)}} \sqrt{\left( \sigma_{\text{eq}}^{\text{VM}^2} + \alpha^2 \sigma_H^2 \right)} \quad (4.26)$$

This is identical to the expression proposed by Deshpande and Fleck in [27]. The pressure sensitivity parameter  $\alpha$  defines the shape of the yield surface, and evaluated in its limit ( $\alpha^2(\nu = 0.5) = 0$ ) Equation (4.26) reduces to von Mises' equivalent stress  $\sigma_{\text{eq}} = \sigma_{\text{eq}}^{\text{VM}}$ . The derivation of Deshpande and Fleck's yield criterion is based on the total strain-energy function and generalized Hooke's law. This yield criterion differs from von Mises' by including the hydrostatic stress term with a pressure sensitive parameter. This extra term accounts for the volumetric change when a porous material is subjected to compression and the cells collapse. The reader is referred to [43] for more details on the von Mises criterion and phenomenon necking.

## 4.2 Finite element analysis theory

It has been a massive increase in the use of computer software to perform finite element analysis and this growth is continuing. Abaqus/Explicit (Abaqus) has been used in this thesis and it is a finite element method (FEM) software, meaning that a continuous problem is being discretised into elements, and solved using numerical schemes. Proper element and numerical scheme selection are just two of multiple important factors to consider when performing FEA. A selection of important features regarding the numerical modelling in Abaqus will be elaborated upon in the following. The reader is referred to Abaqus' guide [50] for more information in numerical modelling and [39] regarding (non)linear FEM theory.

Since the experiments were conducted quasi-statically, a dynamic simulation is required [39]. As the nature of the performed experiments being material failure and contact problems, it motivates an explicit scheme. Abaqus/Explicit offers only the penalty method as the contact formulation with two different algorithms. The contact between the coating layers have not been of focus in this thesis, hence, a general contact algorithm has been chosen with option "all with self". Including both normal and tangential behaviour allowing for separation after contact. The latter using an isotropic penalty formulation with varying friction coefficient  $\mu$  for each numerical model.

Central difference method (CMD) which is the chosen explicit scheme herein is only conditionally stable which is the primary disadvantage with an explicit scheme. The stability limit is solved for the critical time step  $\Delta t_{\text{cr}}$  in terms of the highest natural frequency  $\omega_{\text{max}}$  and the damping ratio  $\xi$ , see reference [39]. However, for linear elastic material and  $\nu = 0$  this relation may read

$$\Delta t_{\text{cr}} \leq \min \left( L_e \sqrt{\frac{\rho}{E}} \right) \quad e = 1, 2, \dots, n \quad (4.27)$$

where  $L_e$  is the element length,  $n$  is the number of elements,  $\rho$  and  $E$  still being density and Young's modulus, respectively. Inertia effects are neglectable in the quasi-static test as mentioned in Section 2.1 [32] which allows for an introduction of mass scaling with great care to increase the stable time increment. A fixed mass scaling for all materials have been used such that the density has been increased by a factor of  $10^9$  which is the factor going from  $[\text{ton}/\text{mm}^3]$  to  $[\text{g}/\text{cm}^3]$ . Utilising mass scaling it is extremely important to check that the kinetic energy is only a tiny fraction of the internal energy [43]. These two energies are not the only ones that has to be checked when performing a nonlinear dynamic problem solved with an explicit

scheme [39, 43]. Possible numerical instabilities might occur yielding artificial energies in the system. Thus, an energy balance check must be performed after each simulation for all time increments. See reference [43] for expression. The latter check has been performed and validated throughout this thesis and will not be commented further. While the former energy check will be discussed in the following numerical models within this chapter and the next.

Element distortion will arise as a problem when simulating both components mainly due to shape distortion and hourglass instabilities. Mesh density is an important factor in the numerical component models due to discontinuity in material properties between the coating and steel layer [39]. The remedy for this issue will be described in Section 5.3.1. Hourglass instabilities are shortcomings when utilising reduced integrated elements [39], and this will be described in more detail in Section 5.3.2 with its remedy. More information regarding element distortion and its remedies can be read about in [39].

Numerical work requires computational power, and often the accuracy will be reduced to lower computational time. All simulations conducted in this thesis have been run with four processors at a computer cluster provided by NTNU named Snurre with the aim of optimizing computational power to obtain higher accurate numerical results.

### 4.3 Calibration of steel material model

Obtaining the Johnson-Cook material model for the steel follows the framework established explicitly in Section 4.1.1, and is motivated since the JC material model is implemented in Abaqus. First, the true stress is Bridgman-LeRoy corrected following Equation (4.8), and the result is seen in Figure 4.1a where the blue line corresponds to the Bridgman-LeRoy equivalent stress versus plastic strain. Next is to fit the JC plasticity model in Equation (4.11) to the established  $\sigma_{eq}^{BL}$  using the nonlinear curve fitting function in MATLAB, *lsqcurvefit*, by the least squares method. The average of the curve fittings of the four specimens resulted in the plot shown in Figure 4.1b, while the model constants are presented in Table 4.1.

Table 4.1: Material constants used for the calibrated steel.

$\rho$ [ton/mm <sup>3</sup> ]	$E$ [MPa]	$\nu$ [-]	$A$ [MPa]	$B$ [MPa]	$n$ [-]
$7.85 \cdot 10^{-9}$	208000	0.3	459.25	424.24	0.4012

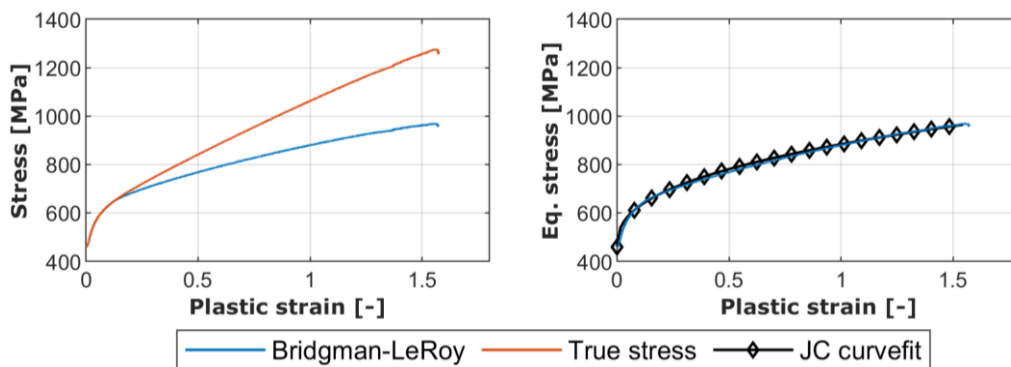


Figure 4.1: (a) Bridgman-Leroy correction and (b) the Johnson-Cook curve fit of the former.

A simulation of the uniaxial tensile test was conducted in Abaqus to validate the material model for the steel. The material constants from Table 4.1 were used and the specimen was modelled using linear, reduced integration axisymmetric stress elements (CAX4R). In the gauge region of the specimen, the size of the elements is 0.036mm x 0.071mm. Loading was modelled as a prescribed velocity of 5000mm/s to the top of the specimen while the bottom of the specimen was fixed. To avoid artificial stress waves caused by a discontinuous or sudden change of velocity when using explicit analysis [43], the load is applied with a smooth step as amplitude when the simulation starts. The modelling of the part and mesh is presented in Figure 4.2. No fracture criterion has been established for the steel since there is no fracture present for the steel in the component experiments conducted. Also, no mass scaling was utilised in this model.

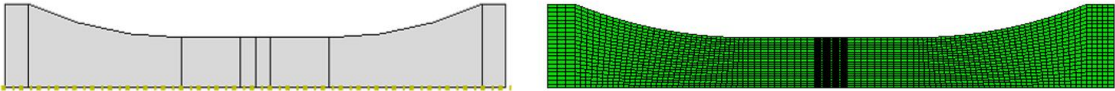


Figure 4.2: Uniaxial tensile specimen in Abaqus with its (a) partitioning and (b) mesh.

Results of the simulation to validate the JC material model is shown in Figure 4.3. Minor discrepancies are seen in both edges of the plot which often motivates for the modified version of JC material model [43]. Nevertheless, the accuracy of the simulation is good, hence the JC material model is satisfactory for the use within this thesis. Note that the simulation here is conducted with axisymmetric elements as a simplification while the component simulation will be conducted with 3D elements. This could give some difference in the accuracy of the JC material model when applied to different element types.

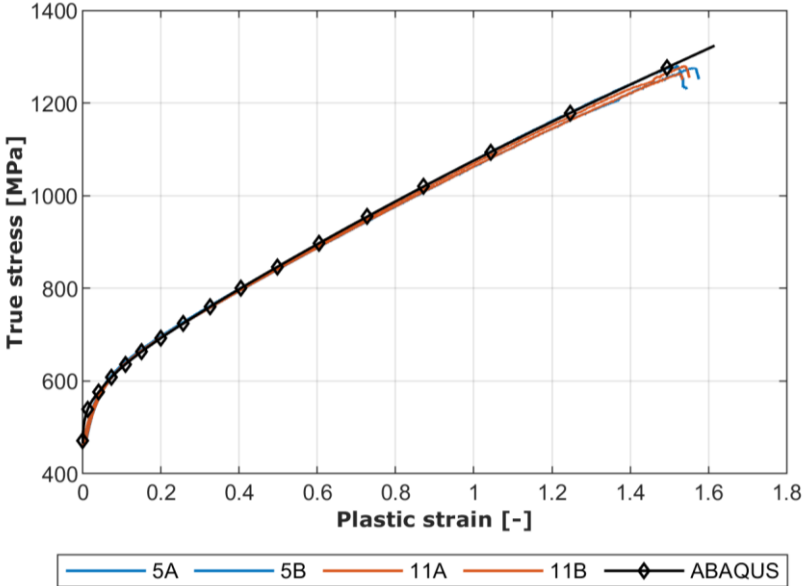


Figure 4.3: Simulation conducted in Abaqus to validate the JC material model compared to the experimental results.

## 4.4 Calibration of the polyurethane material model

A constitutive model will be calibrated to specimen *1i* by reverse engineer modelling, and the same procedure will then be used for *1m* and *1o*. By utilising the pair-grouping observed in true stress versus true strain plot in Figure 3.10 for the material specimens, it is adequate to only calibrate for the specimens *1i*, *1m* and *1o*. An average of the reported  $\rho$  and  $E$  in Table 3.1 and Table 3.3, respectively, within the grouping will be implemented in the numerical material models. The average values used for specimen *1i* is reported in Table 4.2, whereas the others are reported in Table A.1 and Table A.2.

As a measure of an accurate numerical model, it should replicate force versus displacement from the experiment while the parameters chosen shall also give physical meaning. Such that the deformation is similar with respect to end compression and final diameter. Hence, requested field outputs were evenly spaced with 100 intervals and had to include displacements and force.

### 4.4.1 Numerical model geometry

All material specimens were modelled as a 3D deformable solid with geometrical measures given in Table 3.3. For convenience, geometrical measures used in the numerical model of specimen *1i* is given in columns to the far right in Table 4.2. The specimen was then assembled along with two analytically rigid plates. Recalling that the material specimens were lubricated, resulting in low friction coefficient, initially  $\mu = 0.01$ . The lower plate was assigned as fully fixed in space and the upper plate is only free to translate in the specimen's height direction. The upper plate was assigned with a prescribed velocity to simulate the load cell, see Figure 4.4. After multiple simulations and by carefully comparing kinetic energy and internal energy, the velocity's magnitude was set to 0.05mm/s and corresponding step time to 200s. The velocity had to be low to ensure close to no kinetic energies due to the excessive mass scaling. The velocity was also implemented with a ramp function to avoid inertia effects, similar to the steel simulation.

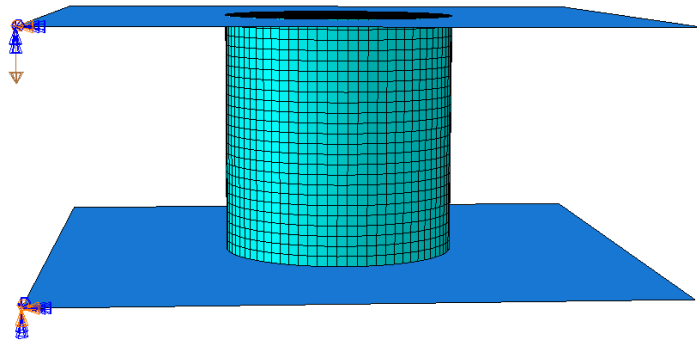


Figure 4.4: Assembly of the numerical material model including boundary condition, prescribed velocity and meshed part.

Since the end goal is to obtain good results from the numerical simulation of the pipe, much of the same settings should be implemented when calibrating a material model. Previous master's thesis [1] and Part 4 in Vestrum's PhD. thesis [3] indicated that distorted elements are a problem when simulating denting of a coated pipeline. Knowing this as a challenge, Abaqus/Explicit only offers distortion control on brick elements when they are linear interpolated. Thus, the same element type *C3D8R* was chosen with reduced integration, and an approximate global element size of 0.5mm. Stresses and strains are most accurate in its integration point, and



reduced integrated elements are better for isochoric elements compared to fully integrated elements [39]. This results in 14 640 elements in the initial model. Reduced integration increases the computational efficiency but may introduce hourglass modes through twelve spurious zero energy modes. For more information regarding the latter case, the reader is referred to [39]. However, element types will be described in more detail in Section 5.2.2.

#### 4.4.2 Polyurethane material model

The PU material model was assigned the mass scaled measured density ( $\rho_{\text{measure}}$ ) and the averaged elastic parameters ( $E$ ,  $\nu$ ) as elastic material behaviour. Crushable Foam material behaviour was assigned to describe the plastic behaviour. This behaviour uses Deshpande and Fleck model, and hardening was set to isotropic. This model has compression yield stress ratio  $k$  and plastic Poisson's ratio  $\nu_p$  as inputs, and the latter is explained in the following.

Gibson and Ashby [23] reported the Poisson's ratio of polyurethane to be approximately  $\nu_{\text{PU solid}} = 1/3$ , and by linear scaling the plastic Poisson's ratio with its density, it is obtained to be  $\nu_p = 0.12$ . This scaling was used by Vestrum in [3]. Further, the elastic Poisson's ratio  $\nu$  is assumed zero.

It was not conducted hydrostatic compression tests, which  $k$  depends on. Abaqus by default assumes nonassociated flow rule and uses  $\beta$  as the shape parameter. However, associated flow rule was assumed when deriving Deshpande and Fleck yield criterion implying that  $\beta = \alpha$  in Abaqus and  $k$  may be determined by

$$k = \sqrt{3(1 - 2\nu_p)} \quad (4.28)$$

Abaqus uses this value to define the shape of the yield ellipse [51], and  $\alpha$  is calculated using Equation (4.19). All properties described above can be found in columns 4 – 9 in Table 4.2. Note that  $\nu_p = 0.5$  corresponds to  $k = \alpha = 0$  and incompressible plastic flow is obtained.

Foam hardening was selected to include stress versus strain relation as material behaviour for crushable foams. In the derivation of Deshpande and Fleck's yield criterion, it was considered a state of uniaxial compression which implied that the stress is equal to the equivalent stress  $\sigma = \sigma_{\text{eq}}^{\text{DF}}$ . Thus, the obtained stress versus strain in Section 3.4.2 shall be implemented in its tabulated form as input in Abaqus with a small modification. Abaqus require that the values start with yield stress as found, but zero plastic strain, which implies that the strain vector needs to be adjusted for this. Yielding parameters ( $\sigma_0$ ,  $\varepsilon_0$ ) for specimen 1i is reported in columns 2 and 3 in Table 4.2.

Table 4.2: Material and geometrical properties assigned in Abaqus for specimen 1i.

<i>ID</i>	$\sigma_0$ [MPa]	$\varepsilon_0$ [–]	$E$ [MPa]	$\nu_p$ [–]	$k$ [–]	$\alpha$ [–]	$\nu$ [–]	$\rho_{\text{measure}}$ [ $\frac{\text{ton}}{\text{mm}^3}$ ]	$h_0$ [mm]	$d_0$ [mm]
1i	5.0	0.049	121.7	0.12	1.51	1.75	0	0.360	12.36	11.78

\* $\rho_{\text{measure}}$  is scaled with  $10^9$  as factor.

It should be noted that the tabulated values obtained from the experiments include deformation up to an average of 74% of the initial height, see Table 3.3, and that the coating is compressed way more during denting of pipe below the indenter. This implies that extrapolation of the

tabulated values is necessary when simulating denting of pipe. However, Abaqus extrapolates the stress versus strain relationship based on the last slope computed from the inserted data [51].

Results of two Abaqus models assigned with the values from Table 4.2 are shown in Figure 4.5 along with experimental data from 1i (blue line). The grey line was modelled to be perfect plastic (no hardening), while the black line (initial PU model) includes the whole plastic equivalent stress versus equivalent plastic strain in the tabulated form directly obtained from the experiment. The tabulated form (equivalent plastic stress versus plastic strain) is illustrated in Figure 4.6b as the blue line. Searching for accurate force versus displacement result, a sensitivity study was conducted on the initial PU model.

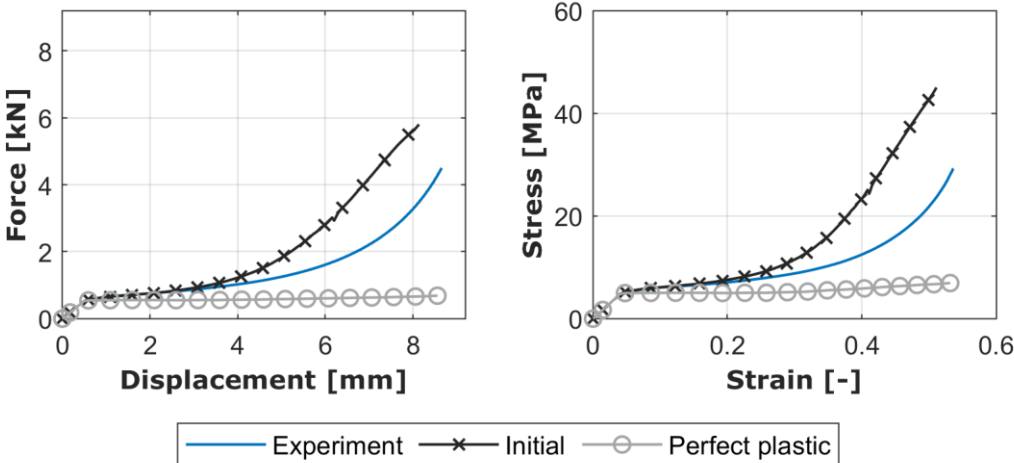


Figure 4.5: Initial material model simulations of material specimen 1i. (a) Force versus displacement and (b) stress versus strain.

The material specimens fractured during the physical experiment as described in Section 2.5, and this phenomenon is not included in the initial PU model. This is the main factor which can explain why the initial PU model densifies before what is observed in the experiments. This implies that the initial PU model should either include fracture and erosion of elements or the material should soften. These two factors being the most obvious, other parameters must also be verified such as the pressure sensitive parameter  $\alpha$  defining the yield surface in DF criterion. Geometrically, the initial PU model accurately replicated the diameter’s evolution and deformation mode.

#### 4.4.3 Softening of the material model

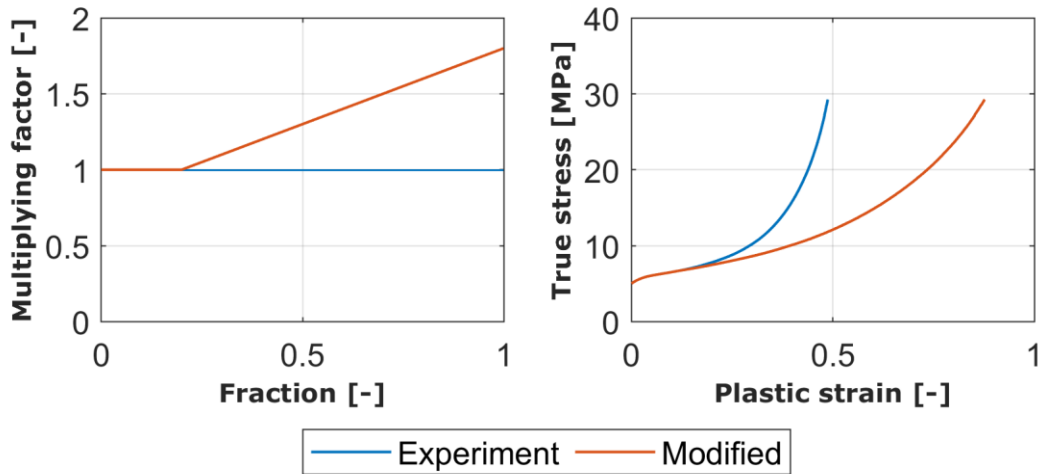


Figure 4.6: (a) Hardening function and (b) modified equivalent plastic stress versus plastic strain for specimen 1i.

The intention of introducing softening in the material is to replicate the fracturing that occurred during testing, and this showed promising results early. Assigning lower stress to higher strain was the chosen method herein, illustrated in Figure 4.6b. In this figure, the blue line is as described above (data from the experiment and inserted as the foam hardening in the initial PU model) while the red line is the softened equivalent plastic stress versus plastic strain. This softened stress versus strain relationship is obtained by multiplying the experimental plastic strain  $p_{PU}$  with a multiplying function  $f_{FP}$ . This multiplying function is based on observations made in Figure 4.5, and reads

$$f_{FP}(\bar{x}) = \begin{cases} 1, & 0 \leq \bar{x} \leq 0.2 \\ \bar{x} + 0.8, & 0.2 < \bar{x} \leq 1 \end{cases} \quad (4.29)$$

here  $\bar{x}$  is a normalised length function with range  $[0,1]$ . The initial PU simulation accurately reproduced the first 20% of the experiment. Thus, the multiplying function is constant for the first 20% followed by a linear softening until fully deformed. Figure 4.6 depicts the corresponding multiplying functions and the stress versus strain relationship, where the stress is unchanged and the modified plastic strain  $p_{PU}^{mod}$  is given as

$$p_{PU}^{mod} = f_{FP} p_{PU} \quad (4.30)$$

Baseline model for the inner PU layer is obtained by keeping the values in Table 4.2 unchanged and by inserting the modified stress-strain relationship into Abaqus' foam hardening. The resulting force versus displacement and stress versus strain is illustrated in Figure 4.7 along with experimental result for both inner specimens, 1i and 2i. Some minor errors are observed for the last  $\sim 3 - 5\%$  which can be explained since a rather simple softening function was derived. It should be observed that this material model has a lower slope in the densification region. Recalling that Abaqus extrapolate the last slope in a foam hardening model, it is clearly seen in Figure 4.6b that the modified hardening has a lower slope compared to the initial. However, this material model represents the material behaviour satisfactorily for the purpose of this thesis. Baseline models for both the middle and outer PU layers were obtained by the exact same procedure and can be seen in Figure A.7 and Figure A.8. Both with satisfactory results and similar tendency as for the inner layer.

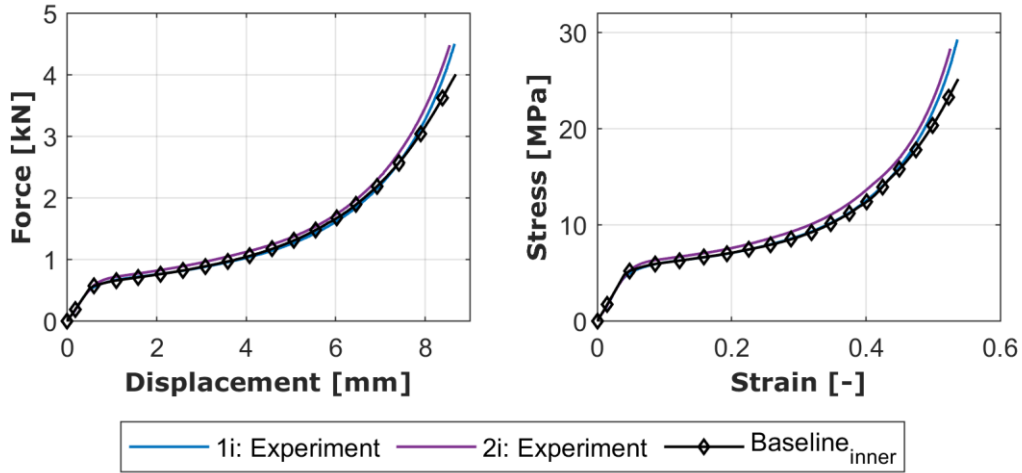


Figure 4.7: Baseline for inner PU layer. (a) Force versus displacement and (b) stress versus strain.

Deformation of the baseline numerical model is illustrated in Figure 4.8, in a similar fashion as specimen 1*i* illustrated in Figure 3.8. In the figure below, the deformation is more symmetric than what was observed from physical testing. However, the evolution of the diameter is well represented by the simulations. Colour legend follows the stress distribution in the specimen as it is deformed. Red corresponds to 50MPa which is approximately 10 times of the polyurethane’s yield stress, and it is observed that some elements are subjected to severe stress.

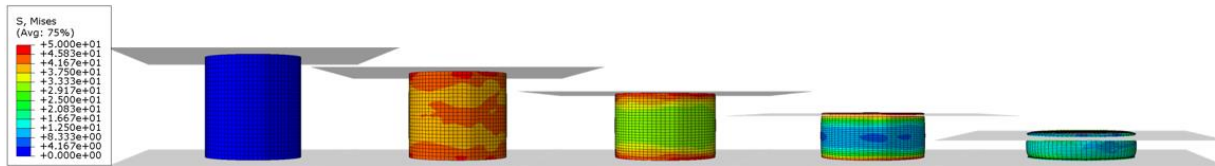


Figure 4.8: Deformation of the numerical baseline model for the inner PU layer.

#### 4.4.4 Sensitivity study

Other parameters were studied simultaneously as the softening study, and all studies were carried out with the initial model as the basis. Thus, the effect of each parameter was observable. In retrospective, many of these studies should have been carried out on the baseline model to optimize this model. However, these studies did not yield more accurate deformation mode, as will be elaborated shortly in the following.

Table 4.3 sums up the parameters tested with corresponding realistic values. Resulting force versus displacement and stress versus strain graphs are shown in Figure A.9, Figure A.10, Figure A.11 and Figure A.12 in the Appendix.

Table 4.3: Four sensitivity studies.

	$\nu_p$ [-]	$\mu$ [-]	Mesh size [mm]	$D_1$
1	0	0	0.3	0.15
2	0.2	0.001	1	0.5
3	0.3	0.1	2	0.8
4	0.5	0.5	—	—

### **Plastic Poisson's ratio, $\nu_p$**

Initially, this study kept the assumption of associated plastic flow, meaning that the parameters ( $\alpha$ ,  $k$ ) are obtained from Equations (4.19) and (4.28), respectively. Main effects were seen in the force versus displacement plot and in the evolution of the diameter. Considering both the slope in the densification region and diameter evolution all the trials yielded poorer trends.

Secondly, it was conducted a study where nonassociated plastic flow rule was applied. Similar to the observation made above, this did not give any better trends.

### **Friction coefficient, $\mu$**

This study did not yield any noteworthy difference with respect to force versus displacement nor stress versus strain. Thus, the assigned friction coefficient was kept as is.

### **Mesh size**

Allegedly, coarser mesh might seem to reproduce both force versus displacement and stress versus strain better than the initial PU model. By a closer inspection in both plots when increasing element size (making it coarser), it was observed that coarser mesh tends to reproduce the densification region poorer. Geometrical deformation was also seen to differ more from the physical test specimens as the mesh became coarser. The major effect of different mesh sizes was seen in the simulation time, since the element size is directly represented to obtain stable time increment, see Equation (4.27). However, as the simulation time for both the initial- and baseline model was efficient, there was no need to increase mesh size to reduce computational time.

It should be noted that in the numerical component models in the following chapter use coarser mesh than in the baseline model established in this section to increase the computational efficiency. From this mesh study, it is fair to assume that the material model will stay satisfactory when increasing mesh size in the following, larger numerical models.

### **Fracture, $D_1$**

Introducing a calibrated fracture criterion in the numerical model would have yielded good results in a similar fashion as the introduction of material softening. Utilising already implemented criteria in Abaqus, the Johnson-Cook damage was chosen with a focus on only one parameter  $D_1$ . This parameter is a measure for equivalent strain, and when an element reaches the assigned value it erodes. Erosion of element is Abaqus' way of representing fracture, and the reader is referred to [39] for more information, and [42] on Johnson-Cook damage. By inspection of Figure 4.5, it can be seen that when the equivalent strain is approximately 0.15 the initial PU model becomes too stiff. Thus,  $D_1 = 0.15$  was tried in one simulation which yielded that almost all elements eroded, and the simulation yielded poor results.  $D_1 = 0.5$  reported much better results, but still far off compared to material softening. No experiments were conducted with the aim of establishing fracture properties of the polyurethane since this was out of scope. Also, due to already accurately obtained results by implementing material softening, no more effort in calibrating fracture was performed.



# Chapter 5

## Numerical study

With established constitutive models for both the steel and polyurethane, both the Sandwich and pipe model can be made. First, the material models will be verified in the former numerical model. Then it will be implemented into the pipe model with the aim to optimize the model. Lastly, a numerical boundary condition study will be performed on the pipe trying to simulate a more realistic impact loading scenario.

Illustrated in Figure 2.1, the pipe consists of four layers with dimensions given in Table 2.1, and Figure B.1 depicts the measured dimensions. The polyurethane layer dominates the coating system with 80%, while the rest is distributed to inner and outer solid polypropylene layers. The outer layer contributes with 15.8% of the total coating thickness. Geometrically, the polypropylene layers contribute significantly, and in the response of the system. Thus, a material model for polypropylene must be included in both numerical component models.

### 5.1 Polypropylene material model

Due to extensive material testing on polypropylene by earlier theses [1, 2, 3] it was concluded that no further testing on this material was necessary. Recalling that the outer PP layer fractured during denting of pipe, and that this phenomenon will not be included in the numerical simulations. An easy material formulation was chosen for solid PP, as elastic-perfectly plastic with von Mises yield criterion (pressure insensitive). See reference [41] for information on this material model. Utilising this formulation, only four material parameters are needed  $\rho$ ,  $E$ ,  $\nu$  and  $\sigma_0$ . From the three theses referred to above, a range of values were reported. However, the values were not far off to each other, and a numerical study performed herein showed that no observable difference could be seen. Hence, the values reported in Table 5.1 is obtained from Hammersvik and Kulsrud (Table 5.1 in [2]) calibration, and are the used values in both component models herein. There may be differences in the manufacturing process of the polypropylene materials in the Shawcor and Logstor pipeline designs, which can alter the mechanical properties of the solid polypropylene. The density for polypropylene reported in the table below obtained from Hammersvik and Kulsrud, is the same as the one reported in the datasheet, see Appendix E.

*Table 5.1: Mechanical properties of solid polypropylene according to [2].*

$\rho$ [ton/mm <sup>3</sup> ]	$E$ [MPa]	$\nu$ [-]	$\sigma_0$ [MPa]
0.9	1300	0.30	28

\*Recall that the density is multiplied with a factor of 10<sup>9</sup>.

The material model and parameter for steel and polyurethane are reported in Table 4.1 and Table 4.2, respectively. Note that the density that is reported for the steel is also multiplied by the same factor of  $10^9$  before inserting it into component models.

## 5.2 Numerical analysis of the sandwich specimen

All twelve sandwich samples were measured prior to the test and are reported in Table B.3 and Table B.4. The numerical model is an extruded 3D deformable solid with average measures from all samples. The height is equal to the average thickness of 76.8mm including all layers with an average ground area of 44.5mm x 44.5mm. An assumption has been made in this numerical model as the physical sample has curvature as seen in Figure 2.2b, while this is neglected in the numerical model since it is minor, and the volume is almost equal. In addition, the partitioning maintains the measured layering and the PU layer is divided into three equal parts to represent the inner, middle, and outer layer. The numerically assembled model is visualized in Figure 5.1a and its corresponding mesh in Figure 5.1b.

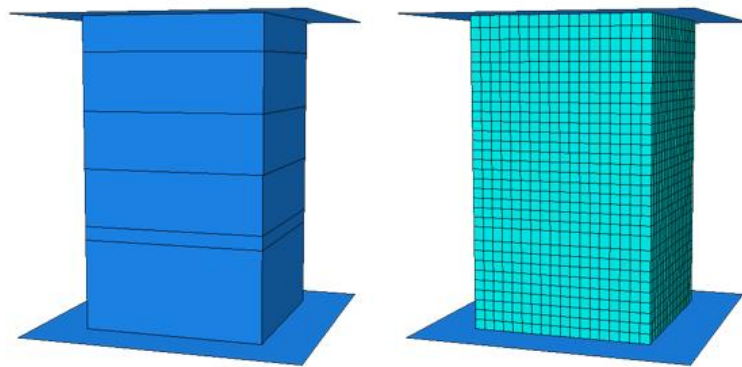


Figure 5.1: Numerical model of the sandwich sample where (a) is the assembly including two rigid plates and the partitioned sample. (b) Assembly with assigned mesh.

The rigid plates are assembled in a similar fashion as for the PU material model, but with a different friction coefficient and prescribed velocity. No lubrication was applied to the sandwich samples prior to testing implying much higher friction between the plate and sample. Several simulations found that the choice of friction coefficient had minor effects, and with respect to deformation, the friction was chosen as  $\mu = 0.8$ . By careful inspection of the kinetic energy against internal energy, the velocity's magnitude was assigned with a ramp function (10% of step time) up to 0.08mm/s for a step time of 350s. Same element type as for the material specimen model (*C3D8R*) was assigned with a bigger global element size of 1.5mm (45 000 elements) to obtain an effective simulation with accurate result.

Assigning the partitioned sections with the respective material model and values, the resulting force versus displacement of this simulation is shown as the black line in Figure 5.2. The overall tendency is well represented by the simulation, comparing it to the other two lines which are the experimental results. The first part in the elastic region is well replicated by the simulation, but a minor discrepancy is seen in the last part. This discrepancy in the elastic domain corresponds to when the PU parts begins to curve and not only compress in the height direction. The plateau is a bit too stiff replicated by the simulation, and it seems to differ extensively from approximately 22mm displacement in the densification region. However, this difference is



mostly due to fracturing in the physical test which correlates with observations made in Section 3.4.3.

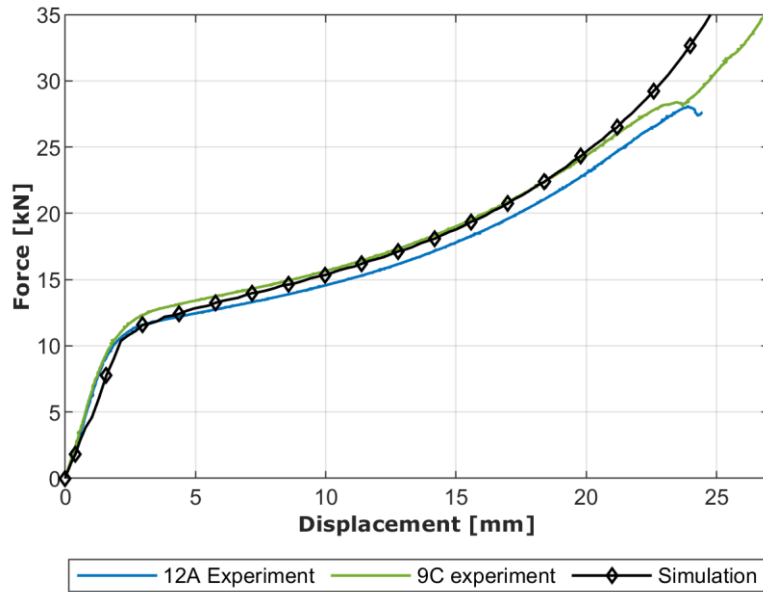


Figure 5.2: Force versus displacement plot of the numerical simulation along with two experimental results.

The deformation is also seen to happen in the polyurethane part of the numerical model, see Figure 5.3. A plastic equivalent strain legend is included to map the distribution of strains when the sandwich model is being deformed. Blue indicates no equivalent plastic strain; thus, it is noticed that next to no strains are neither observed in the polypropylene parts nor the steel section. While red indicates severe strains. More barrelling is observed in the numerical model even though the plastic Poisson's ratio in the PU layer is lower than Gibson and Ashby presented in [23]. However, this can be explained by the fracturing that occurred during the experiments.

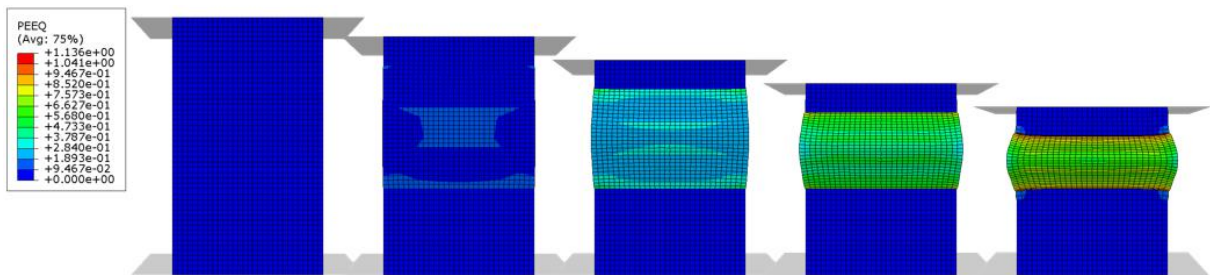


Figure 5.3: Deformation of the sandwich model ranging from initial to final deformation. Colour legend is the plastic equivalent strain.

Recalling from Section 3.5 that the coating part of the sandwich specimen was almost fully compressed in the indentation zone when the pipe was dented. This motivated to run a few simulations where the coating part of the numerical sandwich model was supposed to be almost fully compressed. A few of mesh sizes were tried, and all simulations yielded the same result of being aborted due to distorted elements. The distorted elements were mainly the corner elements in the contacting region between PU and inner- and outer PP layer. As there are no such corner elements in the pipe model this will not be the main problem. However, other elements located in the same contacting region were also seen to become distorted, and this will

raise a problem when simulating the pipe. Fortunately, a remedy was found and will be described in the following.

### 5.3 Numerical analysis of the pipe

The numerical model of the pipe will be similar to all the former models. It will use the extruded 3D deformable brick element as for the sandwich and material specimen models, and it will utilise symmetry to reduce the computational time like was done for the steel simulation. Both the sandwich and material specimen models had relatively short computational time (~half-hour to an hour) indicating that the model did not need to be reduced. The numerical model of the pipe (and indenters) only consist of 1/4, and is clearly illustrated in Figure 5.4. The only difference in the numerical models of the two denting scenarios with different indenters is which indenter that is included in the assembly model.

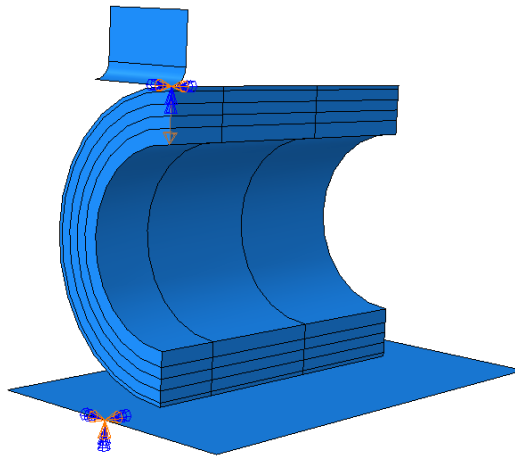


Figure 5.4: Assembly of the numerical pipe model.

The search of an accurate numerical model started with an extensive study with the big indenter, since it was assumed that the model would then be accurate with the small indenter as well. Both indenters will be modelled as analytical rigids, like the plate below the pipe. This is a good representation of the experimental setup displayed in Section 2.6.

#### 5.3.1 Numerical analysis with the big indenter

The numerical simulations performed by Holm and Røshol on the PP-coated pipe yielded severe element distortion and the simulation aborted as described in Section 1.2 [1]. This was found to be a problem in the pipe simulations herein as well. However, it was early observed that by excluding the inner PP layer and reducing the outer PP layer, the simulations completed. Thus, the partitioning of the pipe consists of one layer less than the sandwich model, and now the outer PP layer contributes with 11% of the coating from initially 15.8%. It was observed from early simulations that this partitioning was a great remedy, and that this reduction was of minor importance for the responses' stiffness. The numerical thicknesses are reported in Table 5.2 from innermost to outermost layer. Each layer is assigned the respective material properties as established previously with no changes. All other geometrical measures are kept equal such as the pipe's length, and inner- and outer radius. By only modelling 1/4 of the pipe, the resulting length is  $AD = 500mm$ . Figure 5.5 illustrates both the (a) partitioned and (b) meshed

part with defined coordinates. The pipe is sectioned at  $A$ ,  $B$ ,  $C$  and  $D$ , where  $A$  is the indentation zone and  $D$  being the end.

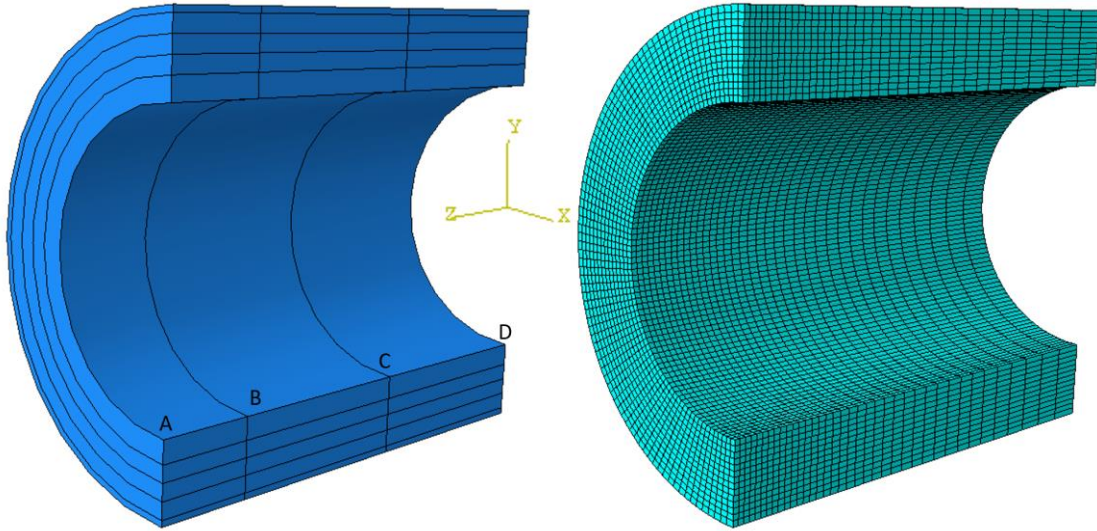


Figure 5.5: (a) Partitioning and (b) mesh of the pipe model in Abaqus.

All elements in the indentation zone got fully compressed and it became evident that the use of extremely fine mesh resulted in element distortion and the simulation aborted. As a remedy between accurate, effective and completion of simulations, it resulted in an element size of approximately 5mm in the radial direction. Bias meshing was utilised in the longitudinal direction of the pipe ranging from, 6 – 9, 9 – 18 and 18 – 36 for  $AB$ ,  $BC$  and  $CD$ , respectively, making the mesh finest at  $A$ . In the hoop direction, the sections  $A$ ,  $B$ ,  $C$  and  $D$  were assigned an element length (in hoop direction) of 8mm, 8mm, 12mm and 18mm, respectively. A total of 44 030 elements were assigned to the pipe model. The same element type ( $C3D8R$ ) with specified distortion control length ratio 0.1 and enhanced hourglass control like the numerical model presented by Vestrum in Part 4 in [3].

Table 5.2: Sectioning measures of the pipe component in Abaqus.

Layer	$t_{\text{steel}}$	$t_{\text{PU}_{\text{inner}}}$	$t_{\text{PU}_{\text{middle}}}$	$t_{\text{PU}_{\text{outer}}}$	$t_{\text{PP}_{\text{outer}}}$	$L_{AB}$	$L_{BC}$	$L_{CD}$
[mm]	22.4	16.1	16.2	16.1	6	100	200	200

Extra boundary conditions must be assigned to the pipe as symmetry is utilised. With respect to the coordinates in Figure 5.5 ( $z$ -direction being longitudinal) the indenter will only move in the  $y$ -direction. This implies boundary conditions  $XS\text{YMM}$  and  $ZS\text{YMM}$  (defined in Appendix D) to the two cross-sections defined by  $yz$ -plane and  $xy$ -plane, respectively.

The contact algorithm used is the same as the previous models, and the assigned friction coefficient was set to  $\mu = 0.2$ . A variety of values were simulated with neglectable differences. Besides geometry, the main difference with this model compared to the others is the total displacement the indenter will be displaced during the simulation. Compared to the sandwich model, this simulation will also engage the steel section which has approximately 26 times the density of polyurethane. When the steel is engaged, the indenter has a high velocity which results in artificial stress waves in this section. It was therefore observed that when the steel became engaged in the simulation the kinetic energy increased to 4 – 5% of the internal energy, which is not valid since mass scaling has been utilised. This increase was also observed in the

force versus displacement plot as the force increased rapidly. Thus, the magnitude of the indenter’s velocity varies with a ramp function for the first 300s of the simulations from 0 – 0.16 – 0.024 [mm/s], where the last assigned velocity is kept constant for 3100s. This ensures that the kinetic energy always is below 0.1% of the internal energy in the system.

The black line marked with X in Figure 5.6 is the resulting force versus outer- and inner displacement. This model has PP properties assigned to the outermost layer and the response until ~60mm outer displacement is extremely accurate. However, the response from here is too stiff. As both the steel and polyurethane materials have been calibrated herein, it was assumed that the assigned PP properties might be the problem. Also, observations done in Section 3.5 found that the outer PP layer fractured and opened in the indentation zone during the test which is not captured by this numerical model. This motivated a simulation where the outer PP layer was assigned with the calibrated outer PU material instead and can be seen in the same figure with O-marker. The complete opposite PU response is captured by this model. Until the steel is engaged (~60mm) the model has too low stiffness but follows perfectly from this point and throughout the analysis. Only considering force versus inner displacement, the latter simulation fits very well to the experimental result. Note that the pipe’s cross-section is exactly the same, and the only difference is which material properties that are assigned to the outermost layer.

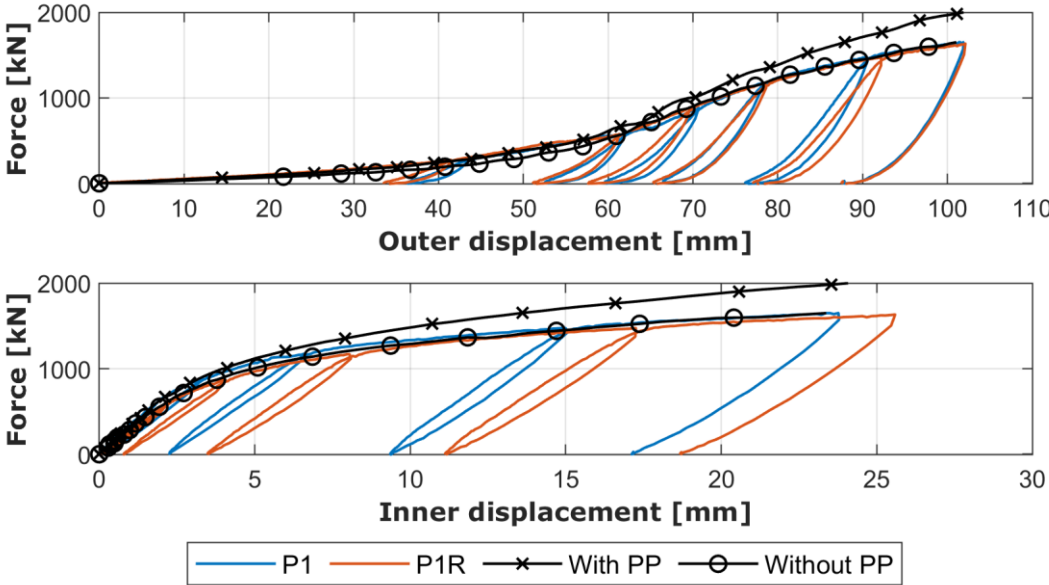


Figure 5.6: Pipe simulations with two different assigned materials to the outermost layer along with experimental data. X-marker has PP properties and O-marker has PU outer properties assigned to the outer layer.

Using a mirror function in Abaqus makes the visualization of deformation easier. In Figure 5.7 both symmetry planes are mirrored and the last internal and external deformation of the pipe is visualized with von Mises stress as legend ranging from 0MPa (blue)–650MPa (red). The colour legend will follow in the next deformed pipe figures. Like the experiment, it is observed that the deformation is very local around the indenter and extremely global due to crushing of the coating on the opposite side towards the rigid plate. The coating elements in between the indenter and steel is fully compressed and stretched in the longitudinal direction to maintain compatible modes [39]. Compatible modes will be described in the following section.



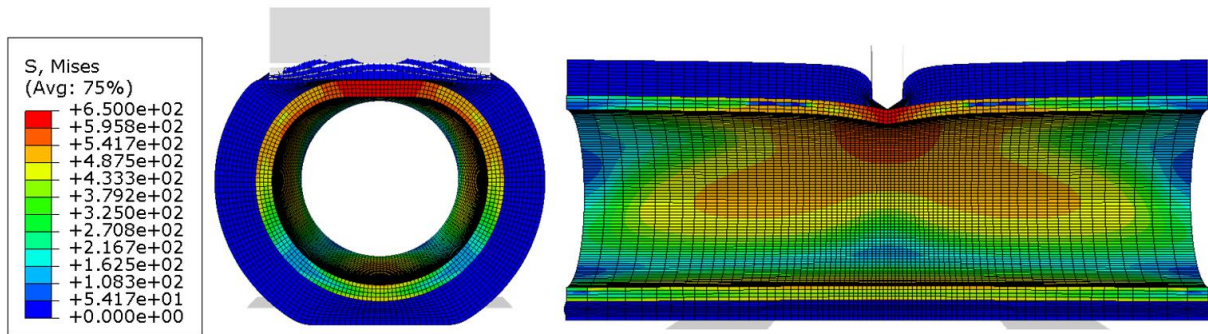


Figure 5.7: Deformation from the pipe simulation utilising mirror function in Abaqus.

Until an outer deformation of about 60mm, approximately all deformation happens in the coating, thus the properties of polypropylene contribute significantly, while the rest of the outer deformation is somewhat 50/50 distributed to the coating and steel, as mentioned in Section 3.5. The latter deformation happens in the bottom part of the PU making it flat towards its rigid support. This along with the fracturing of the outer PP layer implies that the contribution of the PP layer for the last 40mm displacement may be neglected. Combining the two simulations at 60mm, where the PP is included in the first simulation and PU is assigned to the outer layer in the latter, force versus displacement yields excellent results and is illustrated in Figure 5.8 as a black line with diamond-marker. It should be noted that 60mm is half of both simulations due to the different velocities throughout the analysis.

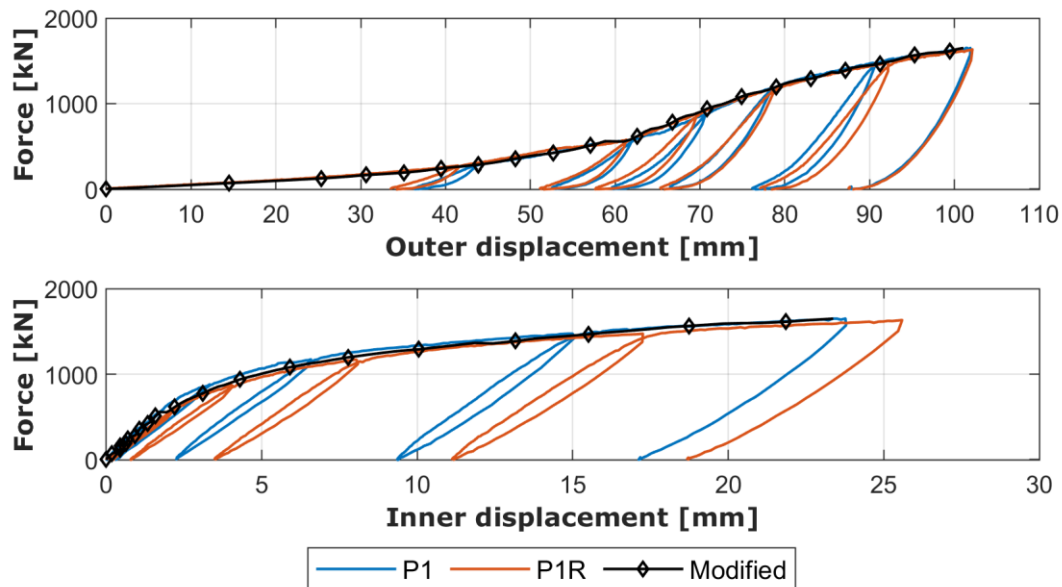


Figure 5.8: Force versus displacement for the simulation along with the experimental data.

### 5.3.2 Numerical analysis with the small indenter

The numerical pipe simulation with the small indenter is seen to have the same trend when inspecting geometrical deformation and the resulting force versus outer- and inner displacement with the remedy described above. Thus, the pipe model is kept unchanged and in the assembly module in Abaqus, the small indenter is enabled while the big indenter is disabled. The resulting force versus outer displacement is shown in Figure 5.9, and the markers indicate the same as above.

X-marker has PP properties assigned to the outermost sectioned layer in the model while O-marker has PU outer properties for this layer. Similar to the observations made for the big indenter is that the simulation excluding PP properties is initially too soft until the steel section is engaged. In contrast, the last half of the simulations with small indenter are both overly stiff and does not replicate the physical response accurately. A remedy will be presented shortly, but first, another important observation must be made. In the displacement range [30 – 55][mm] in Figure 5.9 for the simulation including PP properties has too soft stiffness compared to experimental results. In the numerical simulation, the deformation in this range is very local to only be in the indentation zone, while in the experiment the response is more global and includes the stiffness from the pipe region facing the rigid support. Different mesh sizes were tried without any promising result of the total response and distorted elements were more frequently observed.

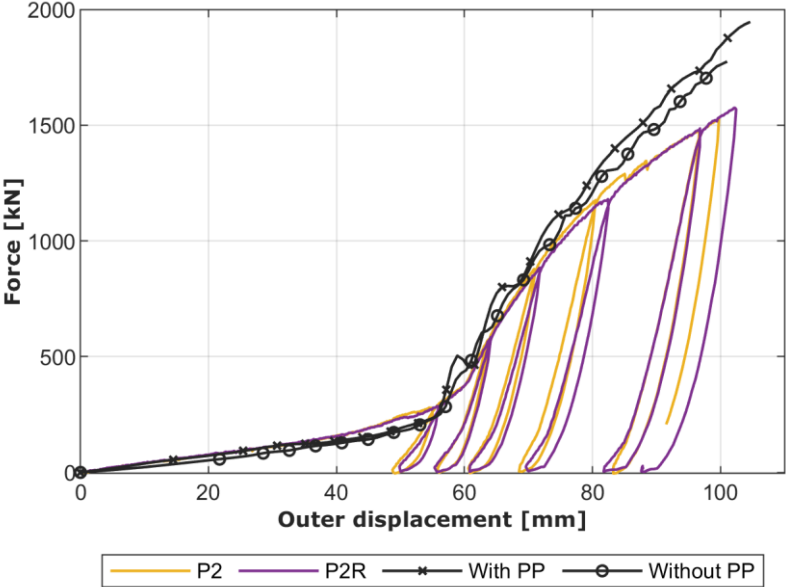


Figure 5.9: Force versus outer displacement for small indenter. X-marker includes PP properties while O-marker includes PU outer properties for the outermost section layer in the model.

As the material models are seen to fit well for the sandwich and big indenter simulations, another reason for the overly stiff response of denting of pipe with small indenter was investigated. The main difference in the deformation mode between the small and big indenter is the size of the indentation zone, and a closeup for the numerical simulation with the small indenter is shown in Figure 5.10. For the quarter pipe simulation, only two rows of elements in the longitudinal direction are seen to be fully affected by the small indenter, and the most affected row is seen to deform extremely throughout the simulation. Element rows close to being directly below the indenter are seen to be subjected to bending, and a curvature mode would be beneficial to replicate the true deformation. Since neither finer nor coarser mesh helped on the other main problem, which is distortion, the choice of element type became obvious since reduced integrated linear interpolated elements do not replicate bending.

It can be observed that the deformation of the elements is linear. A better deformation mode will be to use elements that include bending. Due to computational effectiveness and minimizing file size, quadratic elements were not applied, but the bending effect of an element

was wanted. Thus, the improved *C3D8I*-element was applied for all elements in the *AB*-region shown in Figure 5.5 while the rest were kept unchanged as *C3D8R*-elements. The *I* refers to incompatible mode, and removes shear locking and reduces volumetric locking by augmenting the compatible displacement field with incompatible displacement modes [39]. These incompatible modes describe constant curvature for linear interpolated elements making them able to bend, but are only exact when  $\nu = 0$  [39]. These elements violate the continuity condition, but the augmented displacement modes in *C3D8I*-element passes the patch test and will represent the bending mode fairly well [39].

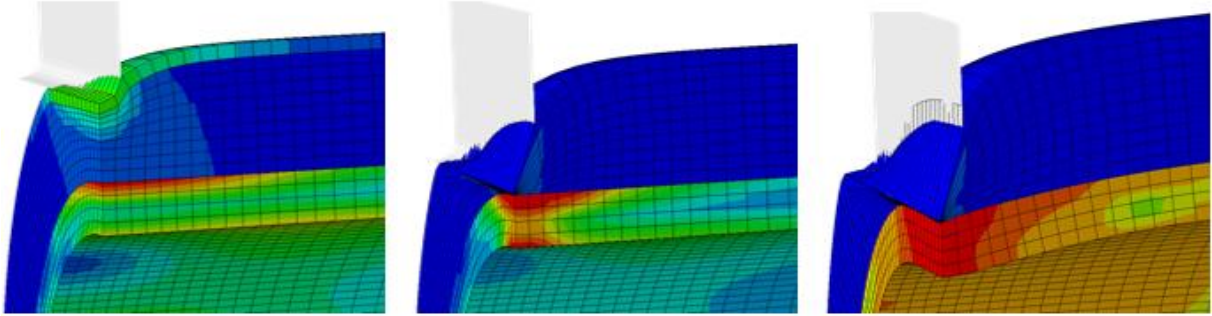


Figure 5.10: Closeup on the indentation zone for the small indenter simulation.

Force versus outer- and inner displacement including the incompatible mode remedy is illustrated in Figure 5.11, and the result is very accurate. Comparing the force versus outer displacement in the below figure with Figure 5.9, the region up until approximately 55mm is equal, while the rest differs. The difference can be explained by the shortcoming when utilising reduced integrated elements as the displacements become wrong when hourglass modes occur [39]. Hourglass modes, as mentioned in Section 4.4, can be read about in reference [39].

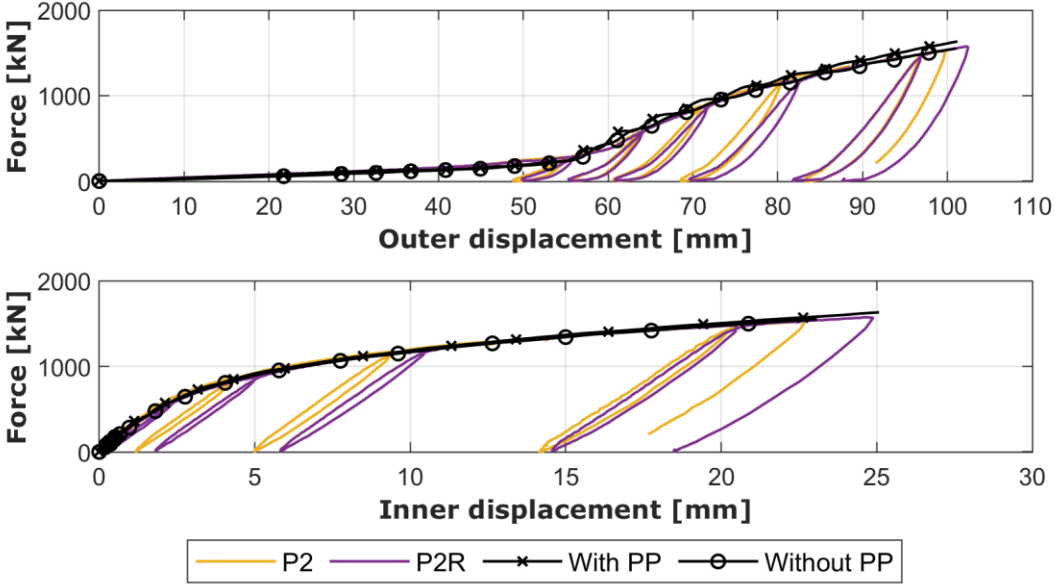


Figure 5.11: Force versus displacement with the small indenter. Both simulations (black lines) includes incompatible modes in the indentation zone. X-marker includes PP properties, while O-marker has PP replaced with PU outer properties for the outermost layer.

The numerical deformation becomes smoother and replicates bending better with assigned incompatible elements, both in the contacting coating region and the elements representing steel material. This is hard to observe, but the numerical deformations are illustrated in Figure A.13 in the Appendix in the same manner as Figure 5.10. Thus, from 55mm outer displacement, the modified numerical models replicate the experimental data much more accurately.

Combining the two simulations presented in Figure 5.11 in the same manner as presented in Figure 5.8 yield very accurate results for the whole displacement range with the small indenter as well. The combined result for the small indenter with incompatible modes is shown in Figure A.14.

The remedy presented for the small indenter was also included in the simulations with the big indenter as some of the elements are subjected to bending here as well. The simulation including PP properties for the outer layer showed improved numerical deformation and the force versus displacement became much more accurate in the last half of the simulation. This model will be referred to as the baseline model (incompatible mode and PP properties). No effects were seen in the numerical model excluding PP properties, and the reason for not being affected is unclear. Force versus outer- and inner displacement including incompatible modes with the big indenter is illustrated in Figure A.15. It should be noted that the combination of incompatible modes simulations with two different material properties for the outermost layer yields the same result as presented in Figure 5.8.

Only changing element type for 20% of the geometry, which correspond to ~38% of all elements due to bias meshing, increases the average computational time with a factor of 2.7, up to approximately 8 hours simulation time. The result file (Abaqus' .odb file) becomes twice the size. This indicates how much more computational time would be needed if quadratic interpolated elements had been utilised.

### **5.3.3 Accuracy of the numerical models**

Fracture has been excluded in the numerical models throughout this thesis. As a remedy, the PU material layers have been softened as described in Section 4.4.3. The fractured outermost layer has been replicated by combining two different simulations with PP and PU outer material properties assigned to the outermost layer. Thus, the first half of the simulation includes PP properties, while the last half excludes PP properties in the outermost layer of the coating. The same procedure has been performed in the numerical denting of the pipe simulations with both indenters. Resulting force versus outer- and inner displacement have been very accurate, similar to how the pipe has been deformed experimentally. This motivates another validation of the numerical models.

The pipes' ability to absorb energy was established in Section 3.5 by creating continuous functions of force versus outer- and inner displacement. Figure 5.12 includes the absorbed energies from the big indenter simulations, as well as its respective experiment (*P1*). By inspection, the absorbed energy distribution between coating and steel in the simulation is very accurate to the experiment. The same trend is seen for the small indenter simulation and is reported in Figure A.16.



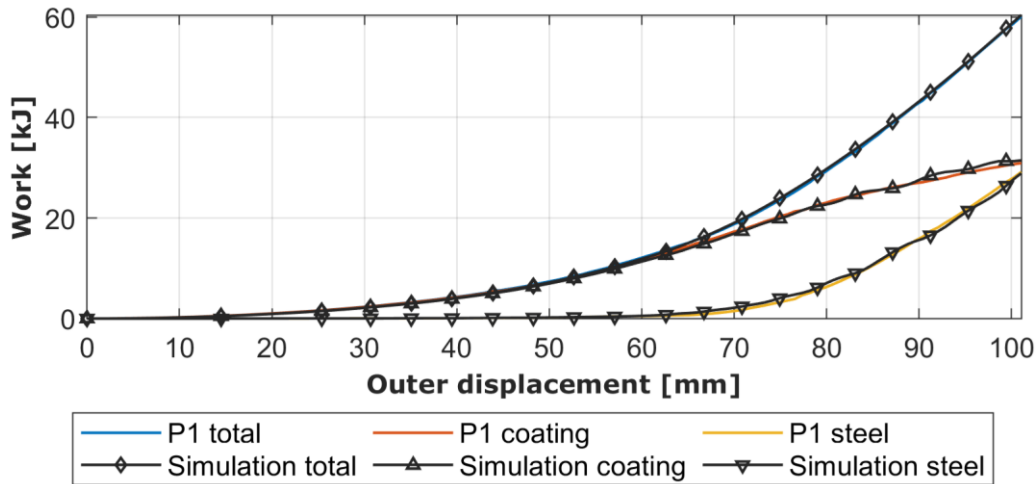


Figure 5.12: (Big indenter) Combined work plot of the P1 experiment and simulation.

Figure 5.13 depicts the numerical result superimposed on the denting of the pipe experiment. The deformation corresponds well with deformations seen in the experiment.

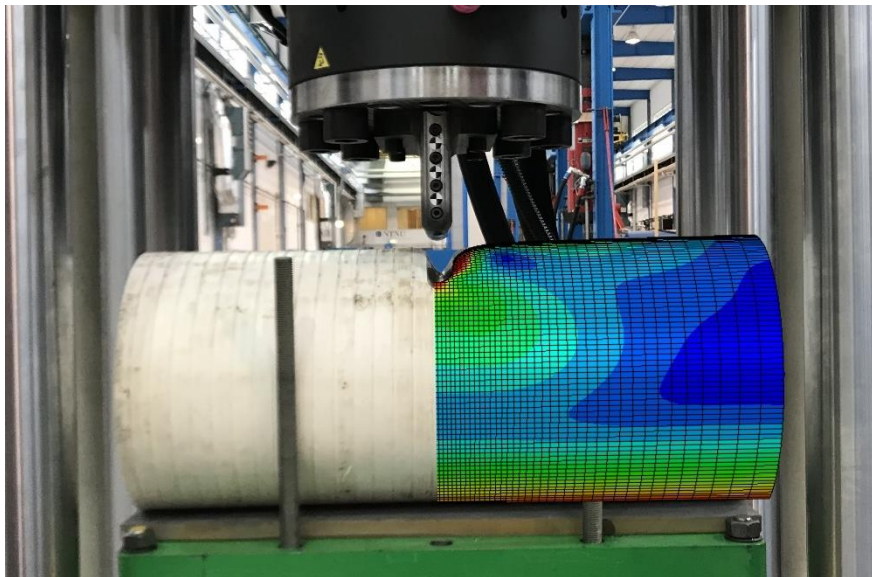


Figure 5.13: Pipe after being quasi-statically dented, both experimentally and numerically.

## 5.4 Coating partitioning study

With accurate numerical component models established, two interesting studies will be conducted only with the numerical model including the big indenter. The first study will explore the effect of density variation found with XRMCT and described in Section 3.2, by assigning the numerical PU parts with different material properties. The PU part is divided into three sections as illustrated in Figure 5.5, each section initially assigned with its respective material model established in Section 4.4. Three models will be made, where all the three PU sections will be assigned with only one material model, i.e. only PU inner, PU middle or PU outer material model. The steel and PP sections are unchanged along with all other features as mesh, loading, etc. The resulting force versus outer displacement plot is shown in Figure 5.14 along with the experimental results from P1 (dashed blue line) and baseline simulation (black line, including incompatible modes and PP properties).

In Figure 5.14, it is evident that the variation in density has a great impact on the response. As found in Section 3.2, the inner PU specimen (yellow line) had the highest density and in the below graph it is seen that this yield an overly stiff response, while the middle PU specimen (red line) had the lowest density and thus the softest response. It is seen that this model is too soft until ~60mm, and then follow the experimental result's trend. It was found earlier that the outer PU specimen (green line) had an average density of the two former and coincide well with the baseline model. However, it is observed that all three coating simulations have some numerical noise in the displacement range of ~[60mm,65mm]. The reason for this is unclear since no kinetic energy was observed (as was one problem when establishing a basis for the numerical model). This implies that the most accurate numerical model is obtained by assigning all three different material models as was done in the baseline simulation.

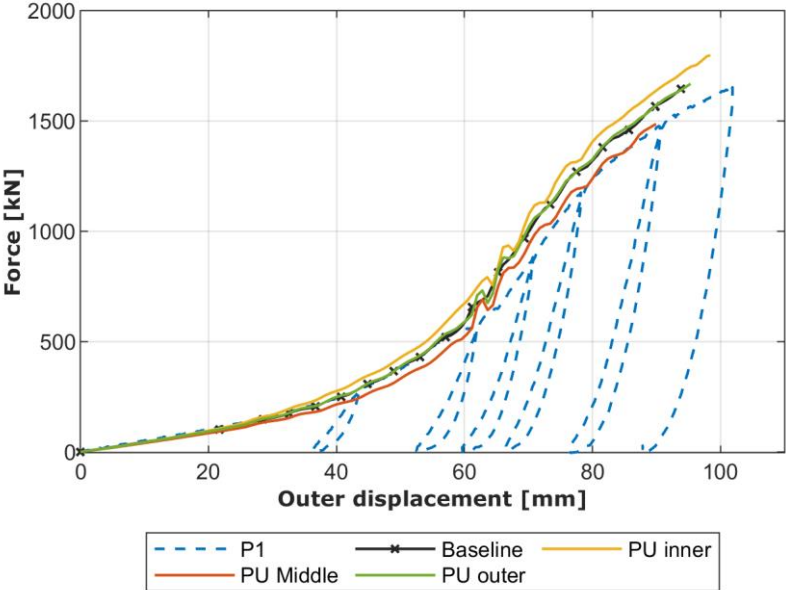


Figure 5.14: Force versus outer displacement for the coating study. The experimental result, baseline simulation and three coating simulations.

All simulations, including the baseline model, aborted towards the end due to extensive distortion in one element. It is seen that the density plays an important role for when the simulation is aborted as well. This was one of the observations made by Holm and Røshol [1] and commented in Section 1.2 herein. The high-density variation between the steel and coating material played a significant part in how far the simulations were performed. However, the coating simulations performed here were conducted far enough to see the main trends by changing the PU material model in the numerical pipe model. Force versus inner displacement plot for the completed coating study is reported in Figure A.17.

### 5.5 Boundary condition study

The last numerical study performed in this thesis will explore the numerical model's possibility to provide an estimate on the force versus outer- and inner displacement with different boundary conditions. This study is motivated by capturing more realistic denting accidents occurring at deep sea. Pipelines are not supported by a rigid seabed, but rather axial forces within the pipe itself [3, 5]. Thus, the rigid plate in the assembly module in Abaqus is disabled and a fully fixed

boundary condition (BC) is established at the end, see Figure 5.15. The end is defined by the cross-sectional xy-plane at the opposite pipe-side of the indenter, i.e. at  $F$  in Figure 5.15. The study will be performed on three different pipe lengths with the big indenter only. The initial pipe span is 1m, the second is 2m, and the third is 4m, recall that only one quarter of the pipe is modelled. All pipes can be seen in Figure 5.15 where  $AD$  is the initial length and  $AF$  is the longer pipes. For the initial pipe, the only changes have been removing of the rigid plate (baseline boundary condition) and adding a fully fixed BC at the end. This boundary condition is easily implemented in Abaqus as it is referred to in the BC modulus as encastre, defined in Appendix D.

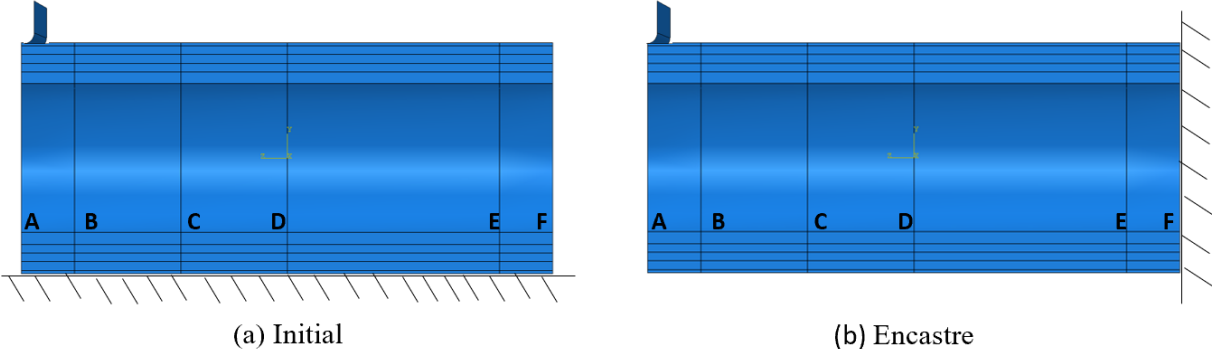


Figure 5.15: Assembly of the long pipe. ( $AD$  is equal to the initial pipe length).

The longer pipes were easily made by extruding the profile to its new length. Keeping the geometry as equal as possible,  $AD$  in Figure 5.15 is completely equal to the initial length. While the last half ( $DF$ ) was partitioned to have even coarser mesh. Bias meshing was used here as well, 36 – 72 and 72 – 36 for  $DE$  and  $EF$ , respectively, to minimize the number of elements in the model due to computational time. The total number of elements increased with 27% and 78.4% to 55 930 and 78 540 elements for the 2m and 4m length pipes, respectively. All elements in  $DF$  were assigned  $C3D8R$  elements, and the lengths are as follows;  $DE = 400\text{mm}$  which yields  $EF = 100\text{mm}$  for the 2m pipe, and  $DE = 1500\text{mm}$  and  $EF = 500\text{mm}$  for the 4m pipe. It should be noted that the general deformation of a cantilever beam includes bending for the whole beam (without the fixed end). Thus, the regions assigned with  $C3D8R$  element type (linear interpolated) will not accurately replicate the bending deformation. However, as the deformation in this study is very local (mostly in the  $AB$  region), the selected elements will capture the main trends with the new boundary condition, although the simulations were aborted a bit early. Defined by Jones and Birch and visualized in Figure 1.2 [18] the failure modes will for this pipe, be due to inelastic deformation and local failure. The steel will fail due to the former, while the coating below the indenter will fail due to the latter, see Figure 5.16b.

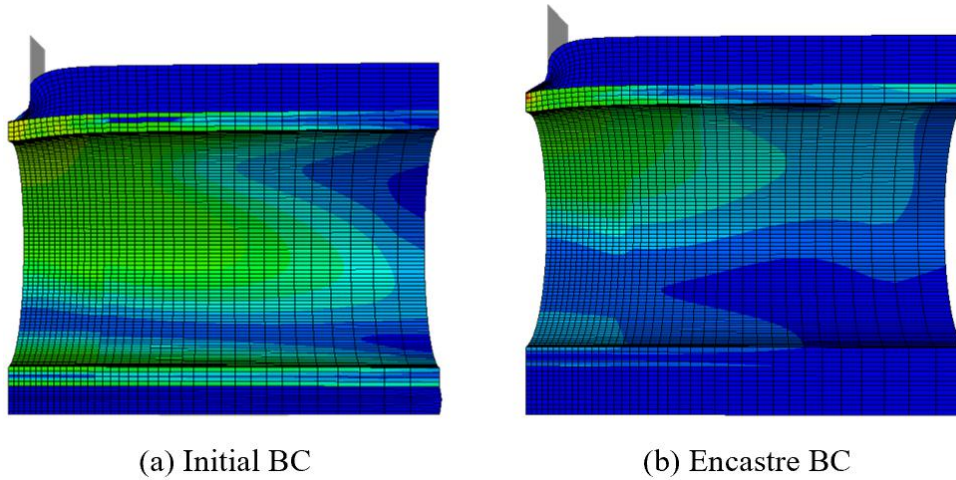


Figure 5.16: Difference in global deformation mode between (a) initial BC and (b) encastre BC.

Figure 5.16 visualizes the different deformations where the initial pipe model with a rigid plate as BC deforms much more globally compared to the pipe models with the fixed end. This can be seen from the difference in the compressed coating on the bottom of the pipe. The models with fixed ends have extremely local deformation directly beneath the indenter, and the well-known cantilever bending is also observed as the pipe's length is increased. Thus, the absorbed energy by the coating contributes far less for the fixed ended model compared to the experimental setup (initial model). This phenomenon can be seen in Figure 5.17 as the steel is engaged much later with the initial BC compared to the fixed end. All three simulations' force versus outer- and inner displacement (purple = 1m, green = 2m and light blue = 4m) are plotted in Figure 5.17 and Figure 5.18, respectively. For reference, simulations with the initial BC were also ran with the two new lengths of 2m and 4m, and are in the same plots marked with dotted red and yellow lines, respectively. Experimental data from *P1* is also included in the figure with dashed blue line (this data set corresponds to the baseline numerical model of the pipe).

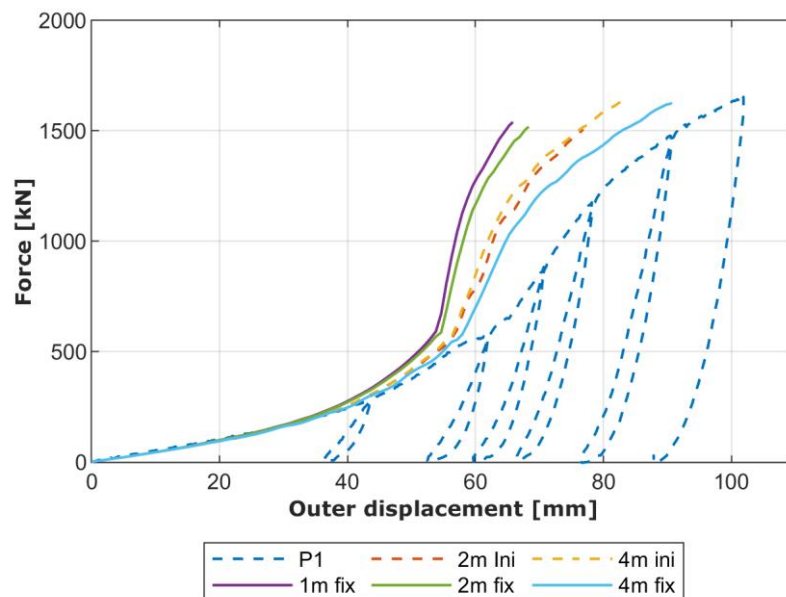


Figure 5.17: Force versus outer displacement for the boundary condition study. Two boundary condition studies are plotted along with *P1* experimental result.

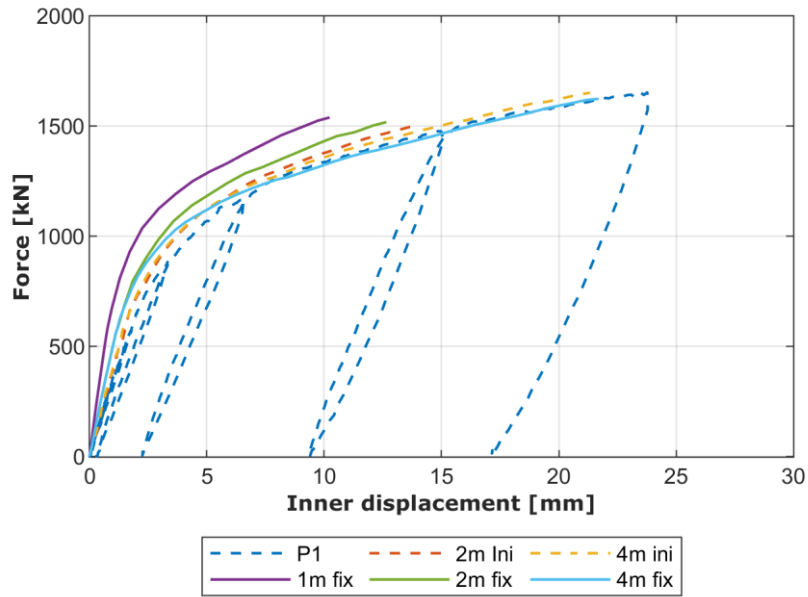


Figure 5.18: Force versus inner displacement for the boundary condition study. Two boundary condition studies are plotted along with P1 experimental result.

The trends considering the numerical models with fixed BC will be described first. It is seen that the response is highly dependent on the pipe's length. Geometrically, the 1m pipe is seen to only deform in the indentation zone with close to no cantilever-like bending, whereas this bending is seen to increase with increased pipe length. This phenomenon can be interpreted in Figure 5.17 and Figure 5.18 as the steel is locally engaged later with increasing pipe length. For the lengths simulated, the opposite trend is observed for the numerical models with initial BC regarding when the steel is engaged. Increasing the pipe's length for the model with the initial BC, the global deformation (crushing towards the rigid plate) decreases as the capacity to withstand crushing increases (increasing area). This phenomenon yields an even more local failure when the pipe is numerically dented to only be in the indentation zone. By combining the above findings, it is seen that increasing the pipe's length, the two boundary conditions start yielding more similar responses with respect to both force versus outer- and inner displacement.

Considering how the stress is distributed in the numerical models when being quasi-statically loaded by the indenter for inner displacement region [0 – 20][mm], the coating will contribute far more for the model with initial BC, as all load will be transferred towards the rigid plate. The fixed BC model will distribute the load towards the fixed end implying that the steel will contribute significantly. The steel's stiffness dominates the overall stiffness implying that the inner displacement with fixed BC will have a much higher elastic stiffness compared to the initial BC. This is easily observable in Figure 5.18 by the graphs' slope (steeper slope = higher elastic stiffness).

As the simulations did not complete, and 5% permanent dent depth of the outer diameter was not obtained for any of the simulations, a value of 5mm inner permanent dent depth is chosen to investigate the energy absorption for the different lengths and BCs. All values reported in Table 5.3 corresponds to this permanent inner displacement, and similar to the procedure described in Section 3.6, the elastic deformation was included. The table includes the force  $F$  needed to obtain a permanent inner displacement of 5mm and how the work done by the



indenter has been distributed. Work done by the indenter corresponds to the total work  $W_{\text{outer}}$ , while  $W_{\text{inner}}$  corresponds to the steel's work directly beneath the indenter and  $W_{\text{rest}}$  is the difference between the two. As the length is increased, it is not fair to assume that  $W_{\text{rest}}$  corresponds to the absorbed energy done by the coating as was assumed in Section 3.5.1. For the fixed BC, this work corresponds to the global bending of the pipe (cantilever-like bending). While for the longer pipes with initial BC this work is still mainly absorbed by the coating.

Table 5.3: All reported values correspond to the inner permanent displacement of 5mm.

Length BC	1m		2m		4m	
	Initial	Fixed	Initial	Fixed	Initial	Fixed
$F$ [kN]	1346	1456	1370	1392	1346	1281
$W_{\text{outer}}$ [kJ]	35.5	21.0	26.2	20.9	24.9	26.6
$W_{\text{inner}}$ [kJ]	10.3	9.1	9.6	9.1	10.0	8.8
$W_{\text{rest}}$ [kJ]	25.2	11.9	16.6	11.7	14.9	17.8

The following observations will all be with respect to Table 5.3 and obtaining an inner permanent displacement of 5mm. The first observation to be made is that  $W_{\text{inner}}$  is kept more or less constant for the different pipe lengths with equal BC. The initial BC indicates that the steel absorbs  $\sim 10$ kJ when the pipe has been permanently dented 5mm, while the fixed BC has absorbed in average 9kJ for the same permanent inner dent. This phenomenon is valid as the steel's capacity should be unchanged in this region when changing the pipe's length and the BC is the same.

The pipe's total absorbed energy is heavily reduced for the initial BC when the pipe length is increased while the needed force is kept approximately constant. This coincides well with the observed deformation of the pipe since the crushing is heavily reduced when the pipe's length is increased, as described earlier.

Lastly, for the pipe model with fixed BC, it is observed that the needed force to permanently obtain an inner dent of 5mm is reduced when increasing the pipe's length, while the total absorbed energy by the pipe is increased. The latter observation coincides well with the global bending seen in the deformation when the length is increased as the total displacement of the indenter increases ( $W_{\text{outer}} = Fu_o$ ). The former observations can be explained by the same argument since the shorter pipe will be stiffer with fully fixed end.

The numerical study presented in this section utilizes an extended numerical model of an inverse modelled pipe model fitted to the experiment described in Section 3.5.1. Thus, the results obtained should only be used as indicators on how the pipe will behave with more realistic length and boundary conditions. The findings obtained also suggests that experiments should be conducted with more realistic boundary conditions, and longer pipes to see how the mechanical response varies, and if the initial simulations done are non-conservative. The latter finding implies that the experiment conducted is non-conservative with respect to the coating's ability to absorb energy. In the following chapter, these observations will be discussed further.

## Chapter 6

### Discussion

How polyurethane coating behaves under quasi-static impact loading has been investigated in this thesis with the main experiment of denting polyurethane-coated pipes. Uniaxial tensile tests of the steel and uniaxial compression tests of the PU coating gave invaluable insight into the material properties, with special focus on mechanical behaviour. As the pipe is being dented and the PU coating in the indentation zone is being compressed, much of the coating will experience both bending and tension. Hence, it would have been beneficial with tension testing of the porous coating with the aim of obtaining knowledge on the coating's behaviour in this loading scenario. The outer PP layer should have been material tested as well since these material parameters are taken from literature and may not be accurate for the PP produced at Logstor.

The results from the XRMCT scans of the PU material specimens gave valuable insight into the pore morphology and how the relative density varies through the thickness of the coating. XRMCT scans could have been conducted post compression to investigate changes in relative density and pore morphology. Compared to the PP coating investigated in earlier works [1, 2, 3], the difference in pore morphology is significant as the PP contains fewer, but larger pores, and the relative density is much lower in the PU coating.

Quasi-static denting of the pipes was conducted with a similar setup as Vestrum [3]. The behaviour of the pipes during denting is also similar to the behaviour seen in PP pipeline designs in Vestrum [3]. However, the PU coating is seen to be much more brittle when subjected to compressive loads, which can be observed from the amount of fracturing in the PU especially, during both compression of the sandwich components and pipes. The retest with both indenters showed a significant reduction of the coating's ability to absorb energy due to the extensive cracking in the first test. The energy absorbed by the coating in the quasi-static impact load is significantly lower for the PU coating compared to the PP coating. This is expected as the PU coating has a much lower relative density as was described in Section 3.6.

Vestrum [3] reasoned that quasi-static denting of the PP pipes could map the local indentation caused by impact loads within a certain velocity range. There has not been conducted any dynamic experiments in this thesis on PU-coated pipelines, so it is unknown if this assumption is valid. It should be conducted dynamic testing to validate this assumption for porous PU. Also, for quasi-static loading, it was observed that the small indenter was most detrimental for a local region, while the big indenter deformed the pipe much more globally. This supports the findings that the retest with the big indenter had a higher reduction of absorbed energy compared to the small indenter.

For the denting, it has been assumed that the inner displacement in the steel pipe is approximately the same as the outer displacement of the steel pipe, such that the thickness is constant. This assumes the steel as incompressible, while steel is generally compressible since the Poisson's ratio is below 0.5. However, measures from the numerical analysis show that the

thickness of the steel beneath the indenter has not changed, hence the assumption seems to be valid. A datasheet validating the steel grade would have been beneficial, but the obtained material steel model fits well with earlier work done on X65 steel [22].

Subset DIC was used to find the area of the PU cylinders from the diameter since assumptions of non-isochoric deformation was used. This assumption is fair since foam materials will exhibit non-isochoric behaviour as the cells collapse and the material densifies. Even though the authors were extremely careful when utilising subset DIC, a small error accumulated in the obtained diameter throughout the DIC analysis yielding the measured area a few per cent below the actual area. This implies that the true stress versus true strain graph from each UCT of material specimen experiment was a bit hardened. The obtained area could have been improved by utilising edge-tracing (Section 3.4.1). However, the area error was relatively low and satisfactory for the purpose of this thesis.

Prediction of a coated pipeline's behaviour under quasi-static load utilising computation tools (herein Abaqus/Explicit) has been the second major part within this thesis. The steel was calibrated to the original Johnson-Cook constitutive model and validated with a simple numerical model using axisymmetric elements. This should have been conducted using the same element type as the component simulation to avoid unnecessary error. Three numerical models were modelled for the PU material specimens coinciding with the inner, middle and outer layer of the PU part established with the same element type as used in the component models. However, the size of the elements used was significantly smaller than in the component test for the same coating which could introduce some inaccuracy. For all three models, the polyurethane material model was calibrated to fit in the crushable foam model in Abaqus, which is based on Deshpande and Fleck's yield criterion [51]. Purely based on observations from the experiment, this material model included material softening as a remedy of extensive fracturing. For the purpose of this study, the material softening was accurate to reproduce the experimental PU material results. It was easily inserted into both component (sandwich and pipe model) studies and gave satisfying trends and results. However, calibration of a fracture criterion (i.e. Johnson-Cook damage as described in Section 4.4.4) would have yielded more realistic response with respect to geometrical deformation, and the force versus displacement could have been improved, and the overall behaviour of the material would be more realistic.

All numerical models have been established using Abaqus/Explicit software with realistic parameters and values, no subroutines have been used. The sandwich model was simplified with straight edges (no curvatures), thus easily modelled and partitioned with average geometrical measures assigned with established material models. This simplified geometry showed satisfying results as all deformation occurred in the polyurethane part, and this geometrical simplification seems valid. Further, the numerical simulations indicated that element distortion will arise a problem in the pipe model since the elements will be compressed significantly more.

Three main remedies were introduced in the pipe model to minimize element distortion as an issue and to improve the accuracy. The first remedy included a new partitioning of the part which reduced the layers consisting of polypropylene and thus increased the polyurethane parts. This remedy reduced distorted elements successfully. However, as the numerical model is no



longer exactly alike the physical pipe, some inaccuracy in the response is to be expected. The second remedy was introduced to compensate for the extensive fracturing observed in the experiment by combining two simulations as described in Section 5.3.1. This gave highly accurate results for the whole domain. Next remedy was introduced with the aim of obtaining higher accurate trends and results from the numerical simulation with the small indenter. The elements in the indentation zone were changed to the improved incompatible version of the linear interpolated element. This change improved the deformation in this region and the overall response of the stiffness significantly, and the result became very accurate for the whole domain with both indenters.

Lastly, numerical studies of the coating properties and boundary conditions were conducted and yielded interesting results. The former study illustrated how dependent the pipe's response is on the established polyurethane material models, and that the total response was best achieved when the PU part was sectioned into the three layers (*i*, *m*, *o*) used throughout this thesis. The boundary condition study exploited a more realistic quasi-static loading scenario where the pipe was modelled to distribute the impacting force into axial force. Due to this distribution, the absorbed energy by the coating was heavily reduced compared to the experimental result. Thus, this study suggests that the coating's ability to absorb energy obtained from experiments is non-conservative and should be further investigated by introducing other boundary conditions and longer pipes to see a more global response of the system. Initially, it was intended to model pinned boundary condition as this would be even more realistic, but then the elements at the end must include bending and this was not implemented in this region. However, the trends seen by introducing fixed BC implies that a more detailed study should be conducted to detect the PU's behaviour under more realistic impacting scenarios. Overall, the numerical study should be interpreted with great care as extending a numerical model based on inverse modelling of a special case might give rise to inaccuracy in the results which are hard to observe.



# Chapter 7

## Concluding remarks

The mechanical behaviour of polymer in coated steel pipelines are not well documented, but its capacity can be included when designing a pipeline if the capacity is documented [5]. Herein, polyurethane-coated pipelines have been experimentally tested, with both material and component tests, with the aim of determining the coating's behaviour under quasi-static load. Calibrated constitutive relations have been established with the aim of numerically simulate the experiments, and to which extent this can be extended. Some concluding remarks and suggestions for further work will be listed up in the following, solely based on the information found and given in the previous chapters.

### 7.1 Conclusions

#### 7.1.1 Investigation of the materials indicated that:

##### Steel

- is found to fit the steel grade X65 and is isotropic and homogeneous across the cross-section.
- was calibrated with Johnson-Cook plasticity with a curve fit to the Bridgman-LeRoy corrected true stress versus plastic strain which yielded sufficient accuracy.

##### Porous polyurethane

- shows varying relative density in the radial direction of the coating, where the lowest relative density is seen in the middle of the PU coating thickness.
- was seen to be extremely brittle and fractured easily when subjected to compression load.
- was calibrated to fit the pressure sensitive Desphande and Fleck yield criterion by softening the obtained true stress versus true strain relationship. The softening is solely based on observation for this problem and yielded accurate results in the component simulation as well.

##### Solid polypropylene

- is modelled using material parameters from earlier theses at NTNU and is assumed to behave elastic-perfectly plastic.

### 7.1.2 Experimental denting of pipe

- Extensive fracturing in the PU part of the pipe along with cracking in PP part beneath the indenter. These parts detached from each other in several places during the tests.
- The coating absorbs a significant amount of the indenter load for both indenter types, and is very dependent on the indenter geometry, where a smaller indenter more easily penetrates the coating.
- Inner deformation of the steel pipe is insignificant before the indenter hits the steel, and until this happens the coating has absorbed 41.2% or 25.6% of the maximum expected energy [5] of 40.5kJ, with big or small indenter, respectively.
- The permanent steel deformation (by QS load and big indenter) reads 4.1% of the steel's outer diameter when subjected to a total work of 40.5kJ, as being the reference work value [5], which is below the allowable permanent dent depth.
- The polyurethane-coated pipeline investigated herein shows a reduced capacity to absorb energy compared to the polypropylene-coated pipeline investigated by Vestrum [3].

### 7.1.3 Numerical denting of pipe

- Implementation of softened polyurethane as a remedy of fractured coating gave accurate results.
- Partitioning was a great remedy and reduced element distortion considerably.
- Incompatible linear interpolated elements gave a much better response as these include bending deformation (discontinuity between neighbouring elements).
- All in all, the numerical model reproduced the experiments with high accuracy.

## 7.2 Recommendations for further work

- A more extensive study of the porous polyurethane coating should be investigated to establish the pore morphology and dependency of temperature as these are important factors for an operational submerged pipeline.
- Testing with the aim of categorizing the polyurethane's fracturing and tensile behaviour along with strain-rate dependency.
- Experiments should be performed to explicitly establish necessary material parameters for the solid polypropylene, including fracture.
- Dynamic component tests should be carried out to check the PU-coated pipeline's ability to absorb dynamic energy compared to absorbed energy from quasi-static loads.
- The boundary condition study herein suggests that other boundary conditions should be tested, with varying pipe lengths.
- Exploring the possibilities of utilising Vestrum's non-destructive method [3] with the aim of establishing a constitutive model for the polyurethane coating. This method has been described in Section 1.2.

## Bibliography

- [1] N. L. Holm and E. T. Røshol, "Denting of coated and uncoated offshore steel pipes," Master's thesis, Norwegian University of Science and Technology, 2015.
- [2] S. Hammersvik og E. B. Kulsrud, «Impact against coated offshore steel pipes,» Master's thesis, Norwegian University of Science and Technology, 2017.
- [3] O. Vestrum, «Impact on porous polymer coated pipelines,» PhD thesis, Norwegian University of Science and Technology, 2020.
- [4] "Rørledningsskader - Skader og hendelser fra Petroleumstilsynets CODAM database," The Petroleum Safety Authority Norway, 2018. [Online]. Available: <https://www.ptil.no/contentassets/a13ec8ed3fc94e3a97b76aebb01bf6e3/roerledningsskader-2018-okt.pdf>. [Accessed 13 March 2020].
- [5] DNV-GL, «Interference between trawl gear and pipelines,» Recommended Practice DNV-RP-F111, 2017.
- [6] E. Gjertveit, J. O. Berge and B. S. Opheim, "The Kvitebjorn Gas Pipeline Repair," 2010. [Online]. Available: <https://www.onepetro.org/conference-paper/OTC-20814-MS>. [Accessed 2020].
- [7] K. Slåttedalen og A. Ørmen, «Impact against offshore pipelines,» Master's thesis, Norwegian University of Science and Technology, 2010.
- [8] J. Fornes and S. Gabrielsen, "Impact against offshore pipelines," Master's thesis, Norwegian University of Science and Technology, 2011.
- [9] V. Aune and M. S. Hovdelien, "Impact against offshore pipelines," Master's thesis, Norwegian University of Science and Technology, 2012.
- [10] T. I. Asheim and I. Mogstad, "Impact against offshore pipelines," Master's thesis, Norwegian University of Science and Technology, 2013.
- [11] E. Jakobsen, "Deformation of pressurized pipelines," Master's thesis, Norwegian University of Science and Technology, 2013.
- [12] E. Digerud and K. Lofthaug, "Bending of x65 offshore steel pipes," Master's thesis, Norwegian University of Science and Technology, 2014.
- [13] DNV-GL, "Risk assessment of pipeline protection," Recommended practice DNVGL-RP-F107, 2017.

- [14] DNV-GL, «Submarine Pipeline Systems,» Offshore standard DNV-OS-F101, 2013.
- [15] Gassco, "Pipelines," [Online]. Available: <https://www.gassco.no/static/transport-3/#/pipelines>. [Accessed March 2020].
- [16] Norsk petroleum, "Rørtransportsystemet," 2020. [Online]. Available: <https://www.norskpetroleum.no/produksjon-og-eksport/rortransportsystemet/>. [Accessed March 2020].
- [17] N. Jones, S. E. Birch, R. S. Birch, L. Zhu and M. Brown, "An Experimental Study on the Lateral Impact of Fully Clamped Mild Steel Pipes.," *Part E: Journal of Process Mechanical Engineering*, 206(2), 111-127, 1992.
- [18] N. Jones and R. S. Birch, "Influence of Internal Pressure on the Impact Behavior of Steel Pipelines," *ASME. J. Pressure Vessel Technol.*, 118(4): 464-471, 1996.
- [19] N. Jones and R. S. Birch, "Low-velocity impact of pressurised pipelines," *International Journal of Impact Engineering*, Volume 37, Issue 2, p: 207-219, 2010.
- [20] W. Q. Shen and D. W. Shu, "A theoretical analysis on the failure of unpressurized and pressurized pipelines," *Part E: Journal of Process Mechanical Engineering*, 216(3), 151-165, 2002.
- [21] A. Manes, R. Porcaro, H. Ilstad, E. Levold, M. Langseth and T. Børvik, "The behaviour of an offshore steel pipeline material subjected to bending and stretching," *Ships and Offshore Structures*, 7:4, 371-387, 2012.
- [22] M. Kristoffersen, "Impact Against X65 Offshore Pipes," PhD thesis, Norwegian University of Science and Technology, 2014.
- [23] I. J. Gibson and M. F. Ashby, *Cellular Solids: Structure and properties*, Cambridge Solid State Science Series. Cambridge University Press, 2nd edition, 1997.
- [24] E. Maire, A. Fazekas, L. Salvo, R. Dendievel, S. Youssef, R. Cloetens and J. M. Letang, "X-ray tomography applied to the characterization of cellular materials. Related finite element modeling problems," *Composites Science and Technology*, 63(16):2431-2443, 2003.
- [25] E. Maire and P. J. Withers, "Quantitative X-ray tomography," *International Materials Reviews*, 59:1, 1-43, 2014.

- [26] L. E. B. Dæhli, J. Faleskog, T. Børvik and O. S. Hopperstad, "Unit cell simulations and porous plasticity modelling for strongly anisotropic FCC metals," *European Journal of Mechanics - A/Solids*, Vol. 65, p:360-383, 2017.
- [27] V. S. Deshpande and N. A. Fleck, "Isotropic constitutive models for metallic foams," *Journal of the Mechanics and Physics of Solids*, Vol. 48, p:1253-1283, 2000.
- [28] Logstor, "Home page Logstor," [Online]. Available: [www.logstor.com](http://www.logstor.com). [Accessed 2020].
- [29] J. Johnsen, A. H. Clausen, F. Grytten, A. Benallal and O. S. Hopperstad, "A thermo-elasto-viscoplastic constitutive model for polymers," *Journal of the Mechanics and Physics of Solids*, Vol. 124, p:681-701, 2019.
- [30] A. Ghiotti, S. Fanini, S. Bruschi and P. F. Bariani, "Modelling of the Mannesmann effect," *CIRP Annals*, Vol. 58, p:255-258, 2009.
- [31] Logstor, "Production method of SinglePipe 120 SW," 2020. [Online]. Available: <https://www.logstor.com/oil-gas/products/singlepipe-120-sw/>. [Accessed April 2020].
- [32] A. Bryman, *Social Research Methods*, Oxford University Press, 5th edition, p:40, 50, 52, ISBN: 978-0-19-968945-3, 2016.
- [33] J. Als-Nielsen and D. McMorrow, *Elements of modern X-ray physics*, John Wiley & Sons, Ltd, 2nd edition, ISBN: 978-0-470-97394-3, 2011.
- [34] O. Vestrum, M. Langseth and T. Børvik, "Finite element modeling of porous polymer pipeline coating using X-ray micro computed tomography," *Composites Part B*, 172: 406-415, 2019.
- [35] Nikon, "XT H 225 ST - Industrial CT scanning," [Online]. Available: <https://www.nikonmetrology.com/en-gb/product/xt-h-225-st>. [Accessed March 2020].
- [36] Xactum, "Laser Micrometers for very high accuracy diameter measurement," [Online]. Available: [https://www.aeroel.it/images/pdf/datasheet/xls\\_xy\\_en.pdf](https://www.aeroel.it/images/pdf/datasheet/xls_xy_en.pdf). [Accessed March 2020].
- [37] S. Khoddam and P. D. Hodgson, "Advancing mechanics of Barrelling Compression Test," *Mechanics of Materials*, Vol. 122, p:1-8, 2018.
- [38] Instron, "Instron High Capacity Systems," [Online]. Available: <https://www.instron.us/-/media/literature-library/products/2019/05/high-capacity-servo-hydraulic-systems.pdf?la=en-US>. [Accessed March 2020].

- [39] K. M. Mathisen, "Lecture notes in TKT4197 - Nonlinear Finite Element Analysis," Norwegian University of Science and Technology, 2019.
- [40] A. Greensted, "Otsu Thresholding," 2010. [Online]. Available: <http://www.labbookpages.co.uk/software/imgProc/otsuThreshold.html>. [Accessed April 2020].
- [41] O. S. Hopperstad and T. Børvik, Material Mechanics Part I, Norwegian University of Science and Technology, Rev. 2017.
- [42] O. S. Hopperstad and T. Børvik, Materials Mechanics Part II, Norwegian University of Science and Technology, Rev. 2016.
- [43] O. S. Hopperstad and T. Børvik, Lecture notes in Impact Mechanics - Part 1: Modelling of plasticity and failure with explicit finite element methods, Norwegian University of Science and Technology, Rev. 2018.
- [44] E. Fagerholt, "eCorr Digital Image Correlation," [Online]. Available: <http://folk.ntnu.no/egilf/ecorr/doc/index.html>. [Accessed 2020].
- [45] BASF, "Home page BASF," [Online]. Available: <https://www.basf.com/global/en.html>. [Accessed 2020].
- [46] MathWorks, "Trapezoidal method in MATLAB," [Online]. Available: <https://se.mathworks.com/help/matlab/ref/trapz.html>. [Accessed 2020].
- [47] Shawcor, "Home page Shawcor," [Online]. Available: <https://www.shawcor.com/>. [Accessed 2020].
- [48] Z. L. Zhang, M. Hauge, J. Ødegård and C. Thaulow, "Determining material true stress strain curve from tensile specimens with rectangular cross-section," *International Journal of Solids and Structures*, Vol. 36, 3497-3516, 1999.
- [49] V. S. Deshpande and N. A. Fleck, "Multi-axial yield behaviour of polymer foams," *Acta Materiala*, Vol 49, p:1859-1866, 2001.
- [50] SIMULIA, "Abaqus analysis user's guide v6.14," [Online]. Available: <http://ivt-abaqusdoc.ivt.ntnu.no:2080/v6.14/books/usi/default.htm?startat=pt03ch12s09s02.html>. [Accessed May 2020].
- [51] SIMULIA, "Crushable foam plasticity models, Abaqus," [Online]. Available: <http://ivt-abaqusdoc.ivt.ntnu.no:2080/v6.14/books/usb/default.htm?startat=pt05ch23s03abm34.html>. [Accessed May 2020].



- [52] SIMULIA, "Defining a symmetry/antisymmetry/encastre boundary condition," [Online]. Available: <https://classes.engineering.wustl.edu/2009/spring/mase5513/abaqus/docs/v6.6/books/usi/default.htm?startat=pt03ch16s10h1b01.html>. [Accessed May 2020].



# Appendix

## A. Figures

### A.1 Figures to Chapter 2 (Experimental setups)

#### Application process of the coating system

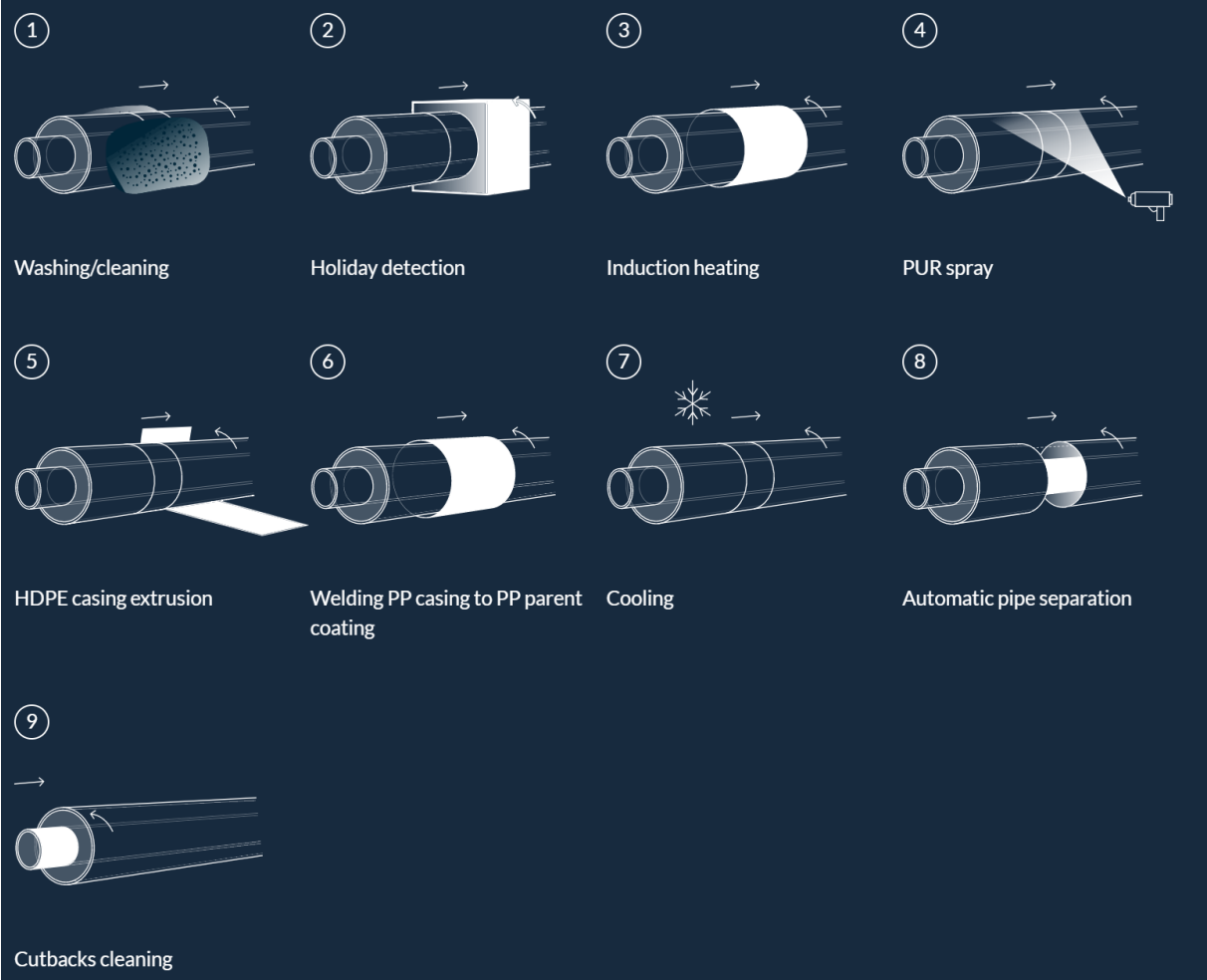


Figure A.1: Application process for the coating at Logstor [31].

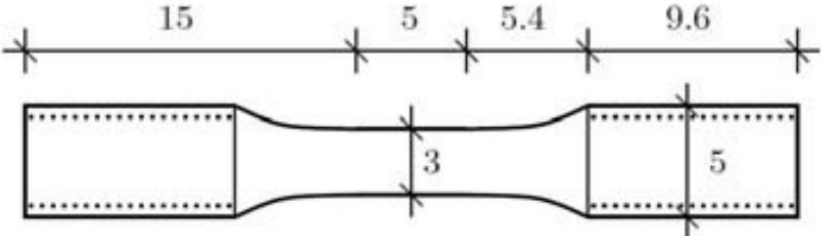


Figure A.2: Standard Split-Hopkinson tension bar specimen with measures in mm [1].

**Aligning the pipe-stubs to detect the same orientation**



Figure A.3: Aligning the pipe-stubs to define cross-sectional orientation equal for all of them.

**Indenter geometry**

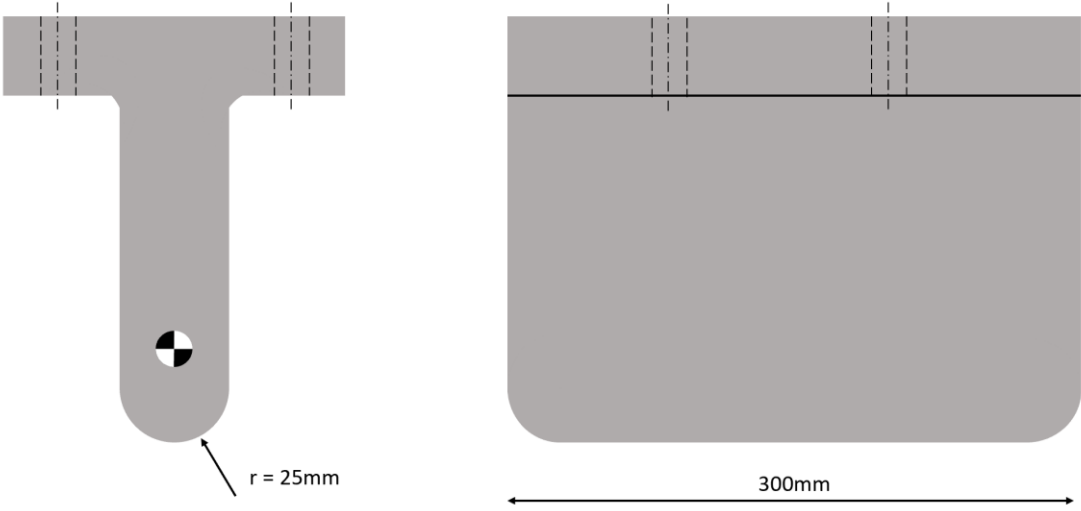


Figure A.4: Illustration of the big indenter.

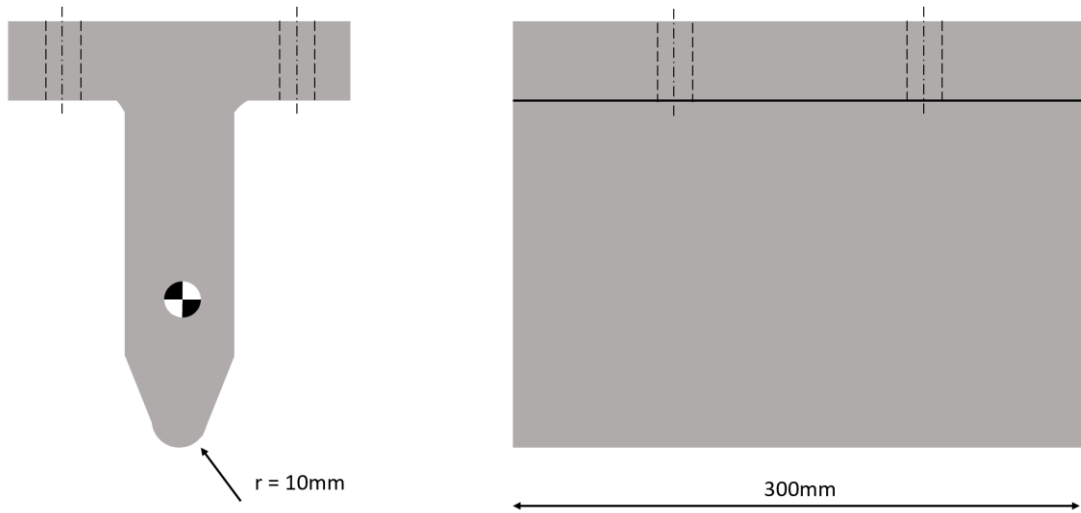


Figure A.5: Illustration of the small indenter.

## A.2 Figures to Chapter 3 (Experimental results)

### Relative density obtained from XRMCT for specimen 1

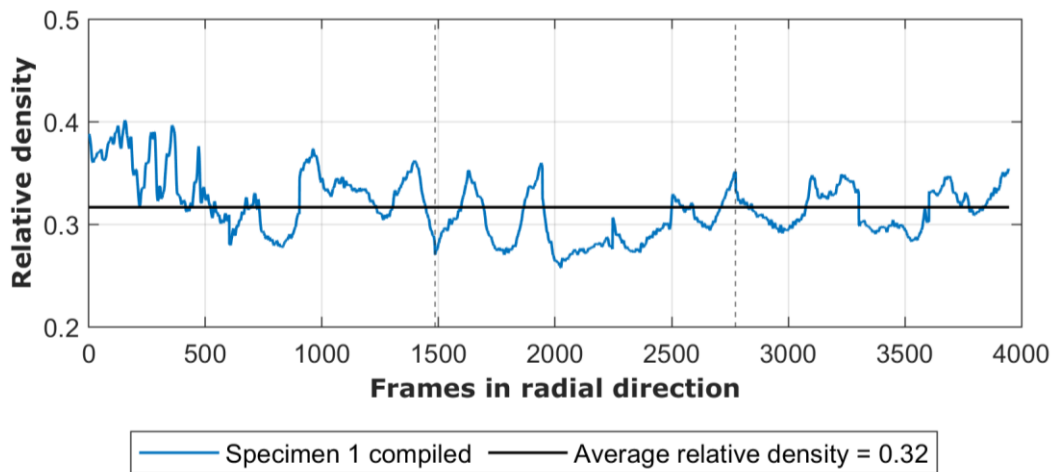


Figure A.6: Relative density plot of specimen 1 obtained from XRMCT along with its average value.

## A.3 Figures to Chapter 4 (Calibration of material models)

### Baseline for middle PU layer

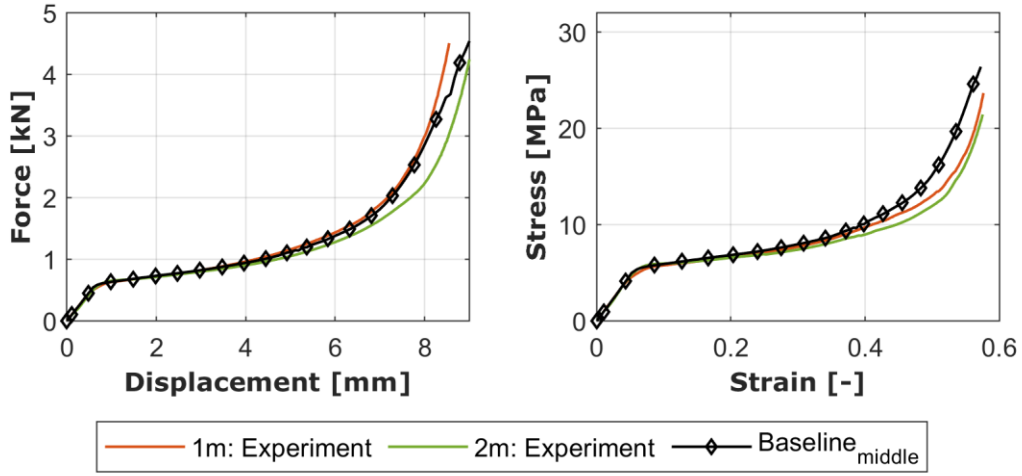


Figure A.7: Baseline for middle material specimens. (a) Force versus displacement and (b) stress versus strain.

Table A.1: Material and geometrical properties assigned in Abaqus for specimen 1m.

$ID$	$\sigma_0$ [MPa]	$\varepsilon_0$ [-]	$E$ [MPa]	$\nu_p$ [-]	$k$ [-]	$\alpha$ [-]	$\nu$ [-]	$\rho_{\text{measure}}$ [ $\frac{\text{ton}}{\text{mm}^3}$ ]	$h_0$ [mm]	$d_0$ [mm]
1m	5.1	0.066	93.3	0.12	1.51	1.75	0	0.321	10.97	11.81

\* $\rho_{\text{measure}}$  is scaled with  $10^9$  as factor.

### Baseline for outer PU layer

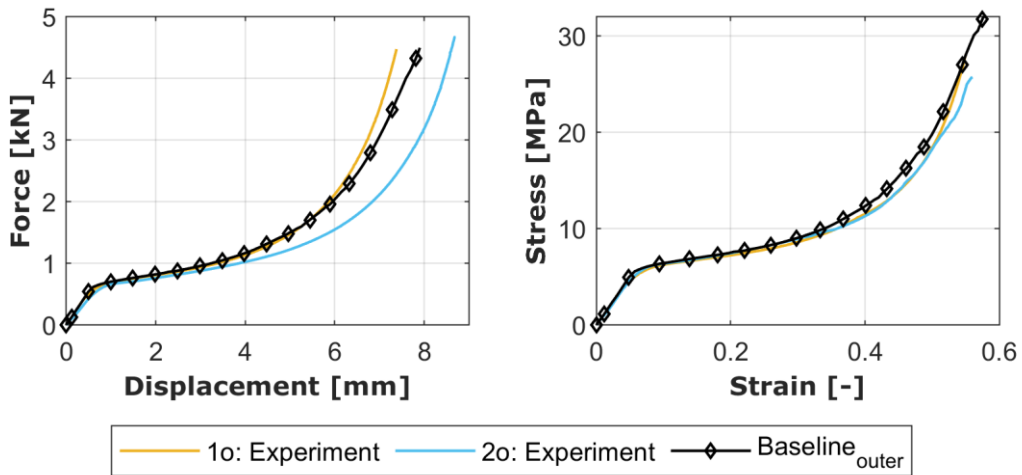


Figure A.8: Baseline for outer material specimens. (a) Force versus displacement and (b) stress versus strain.

Table A.2: Material and geometrical properties assigned in Abaqus for specimen 1o.

$ID$	$\sigma_0$ [MPa]	$\varepsilon_0$ [-]	$E$ [MPa]	$\nu_p$ [-]	$k$ [-]	$\alpha$ [-]	$\nu$ [-]	$\rho_{\text{measure}}$ [ $\frac{\text{ton}}{\text{mm}^3}$ ]	$h_0$ [mm]	$d_0$ [mm]
1o	5.4	0.066	96.2	0.12	1.51	1.75	0	0.335	10.06	11.82

\* $\rho_{\text{measure}}$  is scaled with  $10^9$  as factor.

### Plastic Poisson's ratio

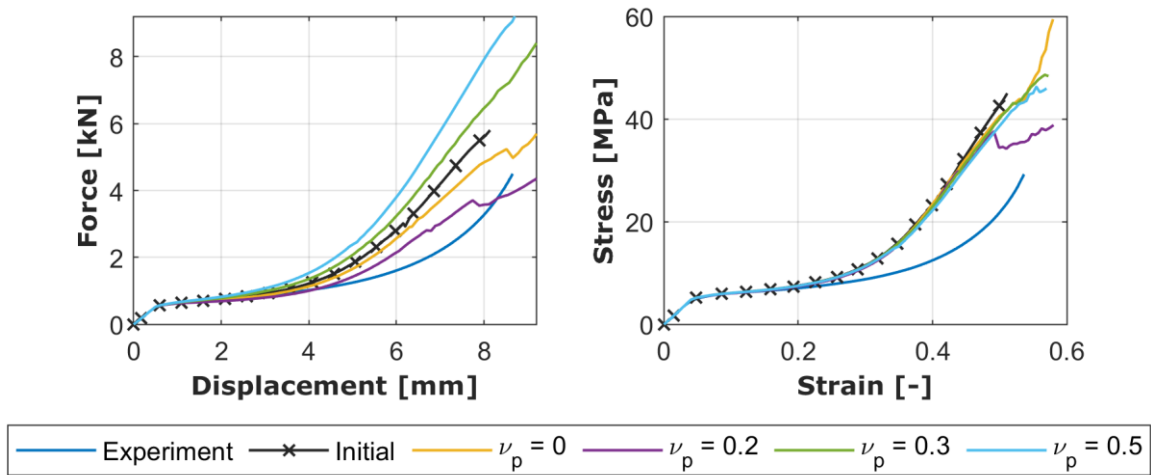


Figure A.9: Material study: Poisson's ratio.

### Friction study

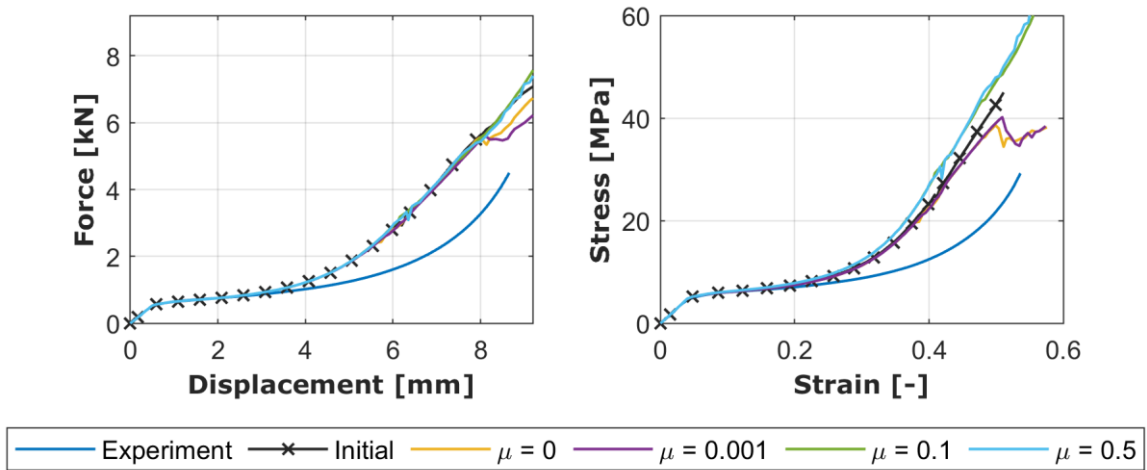


Figure A.10: Material study: Friction coefficient

### Mesh size

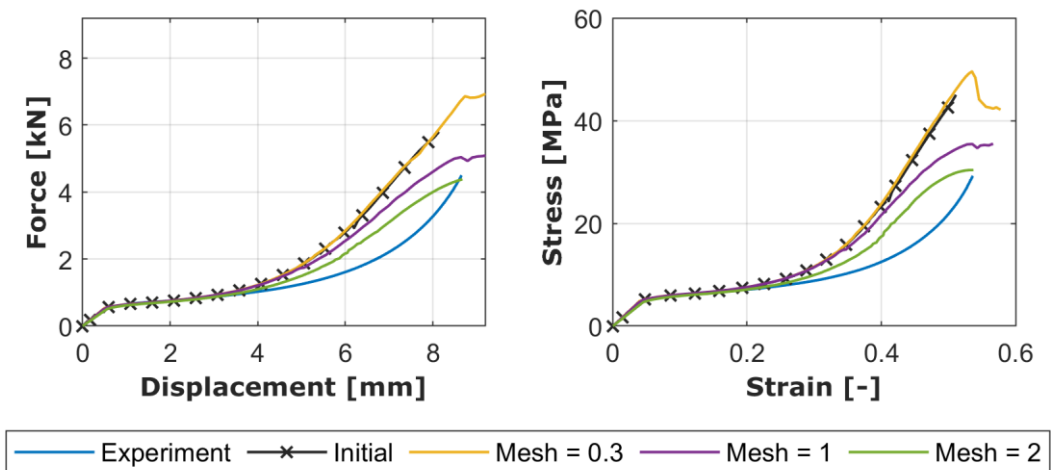


Figure A.11: Material study: Different mesh sizes.

## Fracture

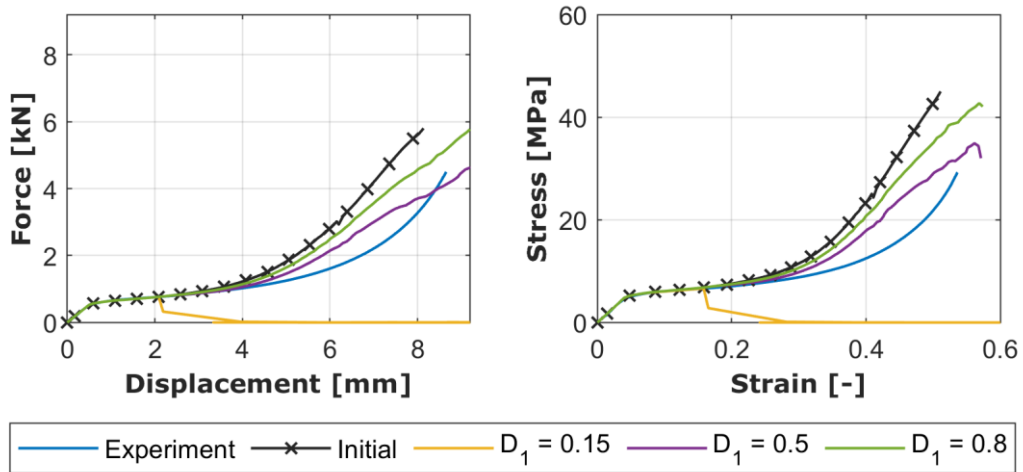


Figure A.12: Material stud: Johnson-Cook Damage.  $D_1$  - equivalent strain yields erosion of element.

## A.4 Figures to Chapter 5 (Numerical study)

### Small indenter: Numerical deformation

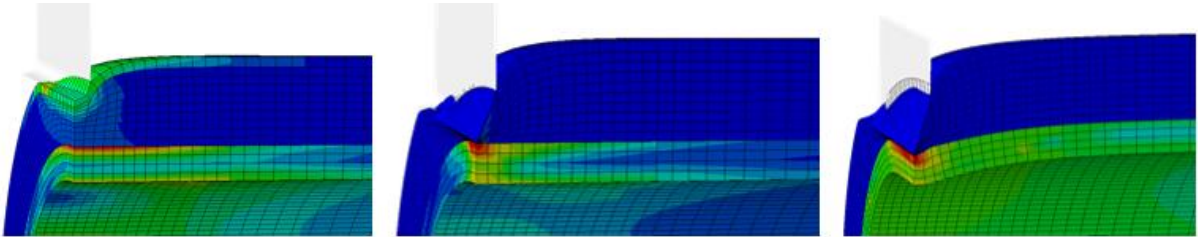


Figure A.13: Numerical deformation with incompatible modes for small indenter.

### Small indenter: Combined FD

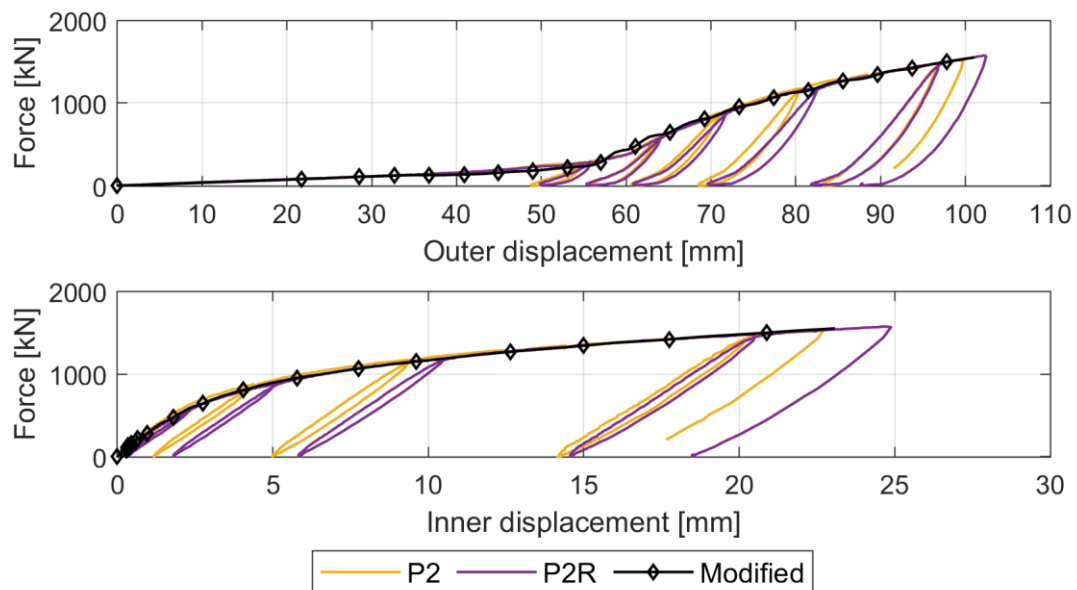


Figure A.14: Combined numerical simulations for small indenter with incompatible mode elements.



### Big indenter: Incompatible modes

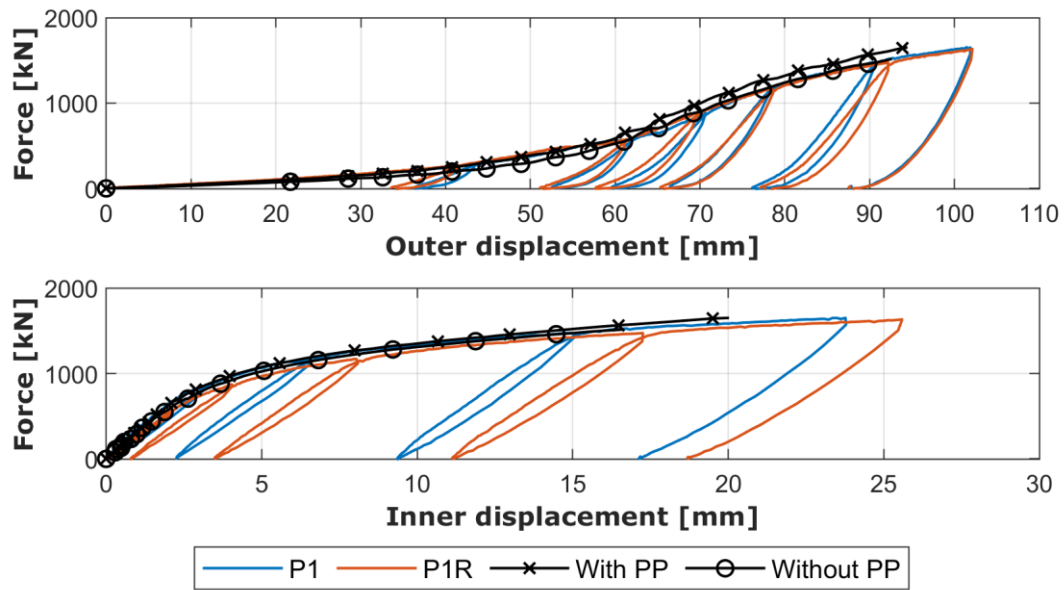


Figure A.15: Force versus displacement including incompatible modes and big indenter.

### Small indenter: Work done by indenter

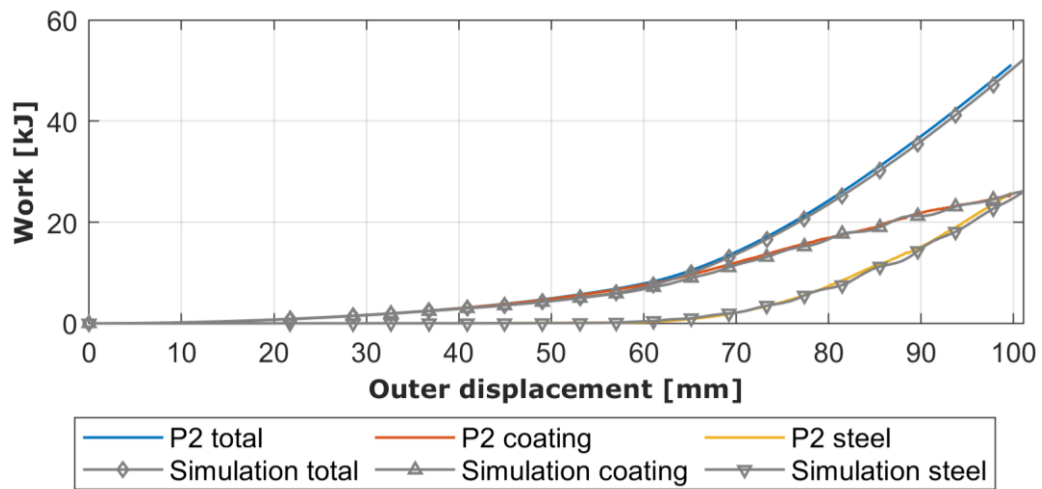


Figure A.16: (Small indenter) Combined work plot of P2 experiment and simulation.

### Coating study pipeline

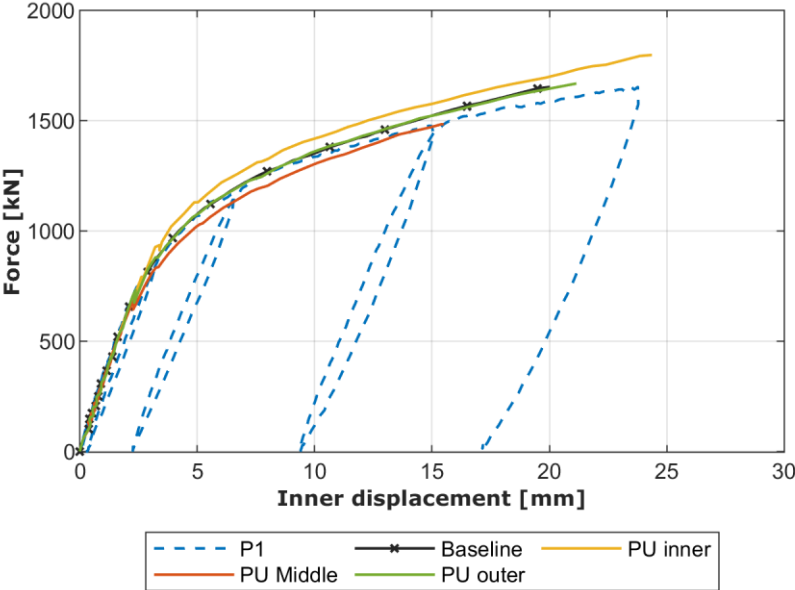


Figure A.17: Force versus inner displacement for coating study. Experimental result,

## B. Measures

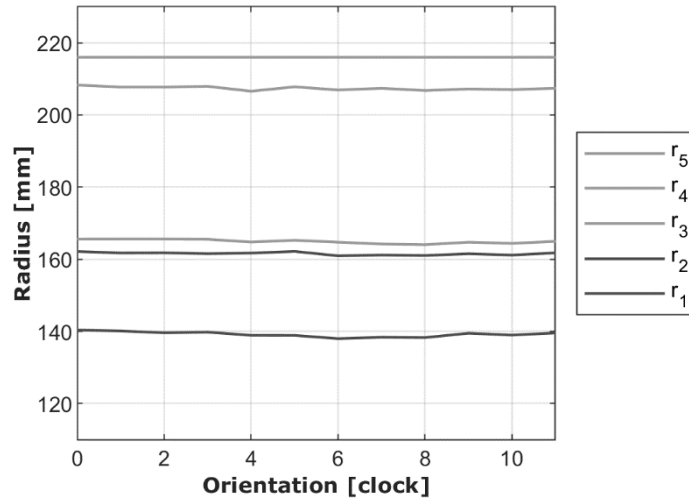


Figure B.1: Radial measures at every cross-sectional hour. Radiuses are defined as in Figure 2.1b.

Table B.1: Outer diameter measures of pipe 3 ring A (P3A).

Clock position	12 – 6	1 – 7	2 – 8	3 – 9	4 – 10	5 – 10	<i>avg</i>
$D_{\text{outer}}$ [mm]	432	432	432	432	432	432	432

Table B.2: Thickness measurements on ring A. See Figure B.2.

Ring	Clock	$t_{\text{steel}}$	$t_{\text{corrosion}}$	$t_{\text{PU}}$	$t_{\text{solid}}$	$t_{\text{coating}}$	$t_{\text{tot}}$
A	12	21.78	3.42	42.72	7.71	53.85	75.63
	1	21.62	3.84	42.15	8.27	54.26	75.88
	2	22.17	3.80	42.15	8.27	54.22	76.39
	3	21.75	3.99	42.40	8.07	54.46	76.21
	4	22.80	3.06	41.81	9.48	54.35	77.15
	5	23.28	3.09	42.54	8.20	53.83	77.11
	6	22.95	3.78	42.19	9.08	55.05	78.00
	7	22.80	3.05	43.17	8.61	54.83	77.63
	8	22.76	3.01	42.72	9.23	54.96	77.72
	9	22.04	3.20	42.48	8.80	54.48	76.52
	10	22.18	3.24	42.62	8.98	54.84	77.02
11	22.20	3.19	42.45	8.60	54.24	76.44	
<i>avg</i>		22.4	3.4	42.5	8.6	54.4	76.8

Table B.3: Width of specimen layers in hoop direction. See Figure B.2.

Ring	Clock	Steel	Lower PU	Upper PU	PP
A	12	42.93	42.78	42.53	42.75
	3	44.46	44.19	44.13	44.36
	6	42.92	42.65	42.66	43.24
	9	44.29	43.84	43.97	44.27
B	12	44.30	43.92	44.17	44.09
	3	44.44	44.23	44.26	44.39
	6	44.17	44.06	44.06	44.67
	9	45.01	44.90	44.77	44.93
C	12	43.04	42.64	42.46	42.71
	3	43.47	43.17	43.11	43.54
	6	44.06	43.80	44.13	44.66
	9	44.17	43.86	43.85	44.02
<i>avg</i>		43.9	43.7	43.7	44.0

Table B.4: Width of specimen layers in length direction. Figure B.2.

Ring	Clock	Steel	Lower PU	Upper PU	PP
A	12	45.01	45.06	45.01	44.70
	3	45.57	45.01	44.86	45.04
	6	45.37	44.69	39.04	45.00
	9	46.46	46.16	45.99	46.24
B	12	46.52	46.09	46.13	45.95
	3	45.25	44.85	44.80	45.07
	6	44.29	43.86	43.97	44.29
	9	44.83	44.63	44.64	45.27
C	12	45.40	44.8	44.65	44.71
	3	45.66	45.22	44.91	45.18
	6	47.10	46.73	46.62	46.45
	9	47.06	46.58	46.35	46.22
<i>avg</i>		45.7	45.3	44.7	45.3

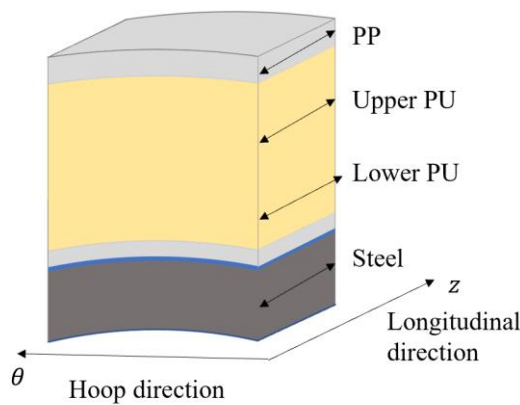


Figure B.2: Width measurements defined.

## C. Tables

*Table C.1: XRMCT setup for sandwich specimen scanning.*

Scan	Voltage [kV]	Current [ $\mu$ A]	Exposure time [s]	Reflective target
<i>CT-6B*</i>	148	121	1	Wolfram
<i>CT-9B</i>	130	154	1	Wolfram
<i>CT-12B</i>	130	154	1	Wolfram
<i>CT-3B</i>	130	154	1	Wolfram
<i>CT-5**</i>	130	154	1	Wolfram

\*One can notice a difference in configuration of the XRMCT scan CT-6B compared to the other scans. This was done to get better resolution for higher quality projections from the scans.

\*\*A scan was conducted with a smaller cut, where the width in both longitudinal and hoop direction was reduced to capture smaller pores.

*Table C.2: XRMCT setup for material specimen scanning.*

Scan	Voltage [kV]	Current [ $\mu$ A]	Exposure time [s]	Reflective target
<i>CT-1i</i>	155	95	1	Molybdenum
<i>CT-1m</i>	155	95	1	Molybdenum
<i>CT-1o</i>	155	95	1	Molybdenum
<i>CT-2i</i>	155	95	1	Molybdenum
<i>CT-2m</i>	155	95	1	Molybdenum
<i>CT-2o</i>	155	95	1	Molybdenum

## D. Theory

### D.1 Formulas to Chapter 3 (Experimental results)

#### Extended Cockcroft-Latham [43]

Extended Cockcroft-Latham proposed by Gruben et al.

$$\omega = \frac{1}{W_C} \int_0^p \left\{ \max \left[ \phi \frac{\sigma_I}{\sigma_{eq}} + (1 - \phi) \frac{\sigma_I - \sigma_{III}}{\sigma_{eq}}, 0 \right] \right\}^{\gamma} \sigma_{eq} dp$$

The Freudenthal criterion is obtained by setting  $\gamma = 0$  and tactically assuming  $0^0 = 1$ . Fracture is occurring when this work has accumulated, and  $\omega$  reaches unity.

$$\omega = \frac{1}{W_C} \int_0^p \sigma_{eq} dp$$

#### Standard deviation (STD)

$$STD_{\eta} = \sqrt{\frac{1}{n} \sum_{i=1}^n (\eta_i - avg)^2}$$

Here,  $\eta$  is used as a generic parameter which correlates to the parameters in the data set under consideration. *STD* depicts how the obtained values in a data set spreads out from the average value.

### D.2 Formulas to Chapter 4 (Calibration of material models)

#### Formulation [41, 42]

Second stress invariant,  $J_2$

$$J_2 = \frac{1}{2} \sigma'_{ij} \sigma'_{ij}$$

Deviatoric part of the Cauchy stress tensor,  $\sigma'_{ij}$

$$\sigma'_{ij} = \sigma_{ij} - \frac{1}{3} \sigma_{kk} \delta_{ij}$$

Kronecker delta,  $\delta_{ij}$

$$\delta_{ij} = \delta_{ji} = \begin{cases} 1 & \text{if } i = j \\ 0 & \text{if } i \neq j \end{cases}$$

Third stress invariant,  $J_3$

$$J_3 = (\sigma'_{ij} \sigma'_{jk} \sigma'_{ki})^{\frac{1}{3}}$$

Lamé constants,  $\mu$  and  $\lambda$

$$\mu = G = \frac{E}{2(1 + \nu)} \quad \text{and} \quad \lambda = \frac{\nu E}{(1 + \nu)(1 - 2\nu)}$$

Constitutive matrix (4<sup>th</sup> order tensor of elastic constants) for isotropic elastic material,  $\mathbf{C}$

$$\mathbf{C} = \begin{bmatrix} \lambda + 2\mu & \lambda & \lambda & 0 & 0 & 0 \\ \lambda & \lambda + 2\mu & \lambda & 0 & 0 & 0 \\ \lambda & \lambda & \lambda + 2\mu & 0 & 0 & 0 \\ 0 & 0 & 0 & \mu & 0 & 0 \\ 0 & 0 & 0 & 0 & \mu & 0 \\ 0 & 0 & 0 & 0 & 0 & \mu \end{bmatrix}$$

Strain tensor,  $\varepsilon'_{ij}$

$$\varepsilon'_{ij} = \varepsilon_{ij} - \frac{1}{3} \varepsilon_{kk} \delta_{ij}$$

Jaumann stress rate,  $\sigma_{ij}^{\Delta J}$ , constitutive equations of the hypoelastic-plastic models are expressed as

$$\sigma_{ij}^{\Delta J} = \dot{\sigma} - W_{ik} \sigma_{kj} - \sigma_{ik} W_{jk}$$

## Mathematics

Operation:  $trace(\mathbf{A}) = tr(\mathbf{A})$ .

Define  $\mathbf{A}$  as a square matrix and take the output of this operation is the sum of elements on the main diagonal.

## D.3 Definitions to Chapter 5 (Numerical study)

Definitions on symmetry, defined in Abaqus guide given in reference [52].

XSYMM: U1 = UR2 = UR3 = 0

ZSYMM: U3 = UR1 = UR2 = 0

ENCASTRE: U1 = U2 = U3 = UR1 = UR2 = UR3 = 0

## E. Datasheets

### E.1 IsoPMDI 92140

#### Technical Data Sheet

#### IsoPMDI 92140

Page 1 / 2  
Version 03/6l  
Date of issue: 17.03.2010

 **BASF**  
The Chemical Company

#### Application

IsoPMDI 92140 is principally used for the manufacture of insulating foams and higher density rigid foams. It is also used for the production of semi-rigid foams in the automotive industry and sound insulation as well as for packaging foams, casting materials, binders and adhesives.

#### Chemical Characteristics

IsoPMDI 92140 is a solvent-free product based on 4,4'-diphenylmethane diisocyanate (MDI) and contains oligomers of high functionality and isomers. The average functionality is approx. 2.7.

#### Supply

The type of supply for the components will be decided after consultation with our Sales Office.

#### Storage, Preparation

Polyurethane components are moisture sensitive. Therefore they must be stored at all times in sealed, closed containers. More detailed information should be obtained from the separate data sheet entitled "Information for in-coming material control, storage, material preparation and waste disposal" and from the component data.

#### Processing

For processing follow the information provided by our technical adviser.

#### Possible Hazards

Isocyanate irritates the eyes, respiratory organs and the skin. Sensitisation is possible through inhalation and skin contact. MDI is harmful by inhalation. On processing these, take note of the necessary precautionary measures described in the Material Safety Data Sheets (MSDSs). See also our separate information sheet "Safety- and Precautionary Measures for the Processing of Polyurethane Systems." Use our Training Programme "Safe Handling of Isocyanate."

#### Waste Disposal

More detailed information is provided in our country-specific pamphlet.

#### Consumer articles, medical products

There are national and international laws and regulations to consider if it is intended to produce consumer articles (e.g. articles that necessitate food or skin contact, toys etc.) or medical objects out of BASF Polyurethanes GmbH products. Where these do not exist, the current legal requirements of the European Union for consumer articles as well as medical products should be sufficient. Consultation with our Sales Office and our Ecology and Product Safety Department is strongly recommended.

*OK 26-10/2010  
RW*

 **PU Solutions  
Elastogran**



## IsoPMDI 92140

Page 2 / 2  
Version 03/bl  
Date of issue 17.03.2010

 **BASF**  
The Chemical Company

Component Data			
	Unit	Value	Method
NCO-content	%	31.5	ASTM D 5155-96 A
Acidity as HCl	mg/kg	100	ASTM D 1638-74
Viscosity (25 °C)	mPa·s	210	DIN 53 018
Density (20°C)	g/cm <sup>3</sup>	1.24	DIN 51 757
Specific heat (20 °C)	kJ/kg·K	1.4	-
Specific heat (80 °C)	kJ/kg·K	1.6	-
Shelf life	days	180	-
Appearance	-	brown liquid	-

The data contained in this publication is based on our current knowledge and experience. In view of the many factors that may affect processing and application of our product, these data do not relieve processors from carrying out their own investigations and tests; neither do these data imply any guarantee of certain properties, nor the suitability of the product for a specific purpose. Any descriptions, drawings, photographs, data, proportions, weights etc. given herein may change without prior information and do not constitute the agreed contractual quality of the product. It is the responsibility of the recipient of our products to ensure that any proprietary rights and existing laws and legislation are observed. (Date of publication).

BASF Polyurethanes GmbH  
Postfach 1140  
49440 Lemförde  
Germany

Tel.: +49 (0) 5443/12-0  
Fax: +49 (0) 5443/12-2474  
Mail: pu-hartschaum@basf.com  
Internet: www.pu.basf.eu

 **PU Solutions**  
Elastogran

## E.2 Elastopor® H 2100/59

### Technical Data Sheet



### Elastopor® H 2100/59

Page 1 / 3  
Version 02/r/s-Halwe-Bommelmann  
Date of issue: 30.03.2012

#### Application

Polyurethane system for the continuous production of heat-resistant rigid foam. The range of application comprises the insulation of district heating pipes using a spray process. Suitability must be examined by the user prior to commercial use.

#### Chemical Characteristics

**Polyol-Component:** mixture of polyetherpolyol, stabilizer, catalyst  
**Iso-Component:** polymeric diphenylmethane diisocyanate (IsoPMDI 92140)

#### Supply

The type of supply for the components will be decided after consultation with our Sales Office.

#### Storage, Preparation

Polyurethane components are moisture sensitive. Therefore they must be stored at all times in sealed, closed containers. The A-component (Polyol) must be homogenised by basic stirring before processing. More detailed information should be obtained from the separate data sheet entitled "Information for in-coming material control, storage, material preparation and waste disposal" and from the component data.

#### Processing

For processing follow the information provided by our technical adviser.

#### Possible Hazards

The B-component (isocyanate) irritates the eyes, respiratory organs and the skin. Sensitisation is possible through inhalation and skin contact. MDI is harmful by inhalation. On processing these, take note of the necessary precautionary measures described in the Material Safety Data Sheets (MSDSs). This applies also for the possible dangers in using the A-component (Polyol) as well as any other components. See also our separate information sheet "Safety- and Precautionary Measures for the Processing of Polyurethane Systems." Use our Training Programme "Safe Handling of Isocyanate."

#### Waste Disposal

More detailed information is provided in our country-specific pamphlet.

#### Consumer articles, medical products

There are national and international laws and regulations to consider if it is intended to produce consumer articles (e.g. articles that necessitate food or skin contact, toys etc.) or medical objects out of BASF Polyurethanes GmbH products. Where these do not exist, the current legal requirements of the European Union for consumer articles as well as medical products should be sufficient. Consultation with our Sales Office and our Ecology and Product Safety Department is strongly recommended.



20-4-2012  
Rt

# Elastopor® H 2100/59

Page 2 / 3  
Version 02/ms-Halwe-Bommelmann  
Date of Issue 30.03.2012



## Component Data

	Unit	Polyol-Comp	Iso-Comp.	Method
Density (20 °C)	g/cm <sup>3</sup>	1.03	1.24	G 133-08
Viscosity (20 °C)	mPa·s	1060	300	G 133-07
Shelf Life	days	90	180	AA S-10-03 22.011

## Processing Data

### Cup Test:

	Unit	Value	Method
Component temperature	°C	20	
Quantity	g	A = 139.4 B = 175.6	
Mixing ratio		A : B = 100 : 126	
Stirring time	s	10	
Cream time	s	16	G 132-01
String time	s	32	G 132-01
Rise time	s	46	G 132-01
Density, free rise	kg/m <sup>3</sup>	300	G 132-01



# Elastopor® H 2100/59

Page 3 / 3  
Version 02/ms-Halwe-Bommelmann  
Date of Issue 30.03.2012



Physical Properties			
	Unit	Measured value	Method
Specimen produced by using a lab stirrer.			
Density / core	kg/m <sup>3</sup>	300	DIN EN ISO 845
Compressive strength	N/mm <sup>2</sup>	5.0	DIN 53 421
Compression	%	10	DIN 53 421
Closed cells	%	93	ISO 4590

® = registered trade mark of BASF

The data contained in this publication is based on our current knowledge and experience. In view of the many factors that may affect processing and application of our product, this data does not relieve processors from carrying out their own investigations and tests; neither does this data imply any guarantee of certain properties, or the suitability of the product for a specific purpose. Any descriptions, drawings, photographs, data, proportions, weights etc. given herein may change without prior notice and do not constitute the agreed contractual quality of the product. It is the responsibility of the recipient of our products to ensure that any proprietary rights and existing laws and legislation are observed. (Date of publication).

BASF Polyurethanes GmbH  
Postfach 1140  
49440 Lemförde  
Germany

Tel.: +49 (0) 5443/12-0  
Fax: +49 (0) 5443/12-2474  
Mail: pu-hartschaum@basf.com  
Internet: www.pu.basf.eu

 PU Solutions  
Elastogran

*20 V-112  
10/12*

## E.3 Borcoat™ EA165E

11.03.2008 Ed.6



**Polypropylene**  
**Borcoat™ EA165E**  
Polypropylene compound for Steel Pipe Coating

### Description

**Borcoat EA165E** is an elastomer modified compound, based on a high molecular weight copolymer. The elastomer modification gives excellent low temperature impact resistance.

The product is self coloured.

### Applications

**Borcoat EA165E** is recommended for injection moulding of thick field joints used in:

Steel Pipe Coating

### Specifications

**Borcoat EA165E** is intended to fulfill following National and International standards, when appropriate industrial manufacturing standard procedures are applied and a continuous quality system is implemented and when used in combination with and a compatible powder epoxy.

Draft ISO 21809-2

### Special features

**Borcoat EA165E** The product is primarily used as an injection moulded coating for thick field joints.

### Physical Properties

Property	Typical Value	Test Method
Density	900 kg/m <sup>3</sup>	ISO 1183
Melt Flow Rate (230 °C/2,16 kg)	0,3 g/10min	ISO 1133
Flexural Modulus (2 mm/min)	800 MPa	ISO 178
Tensile Strain at Yield (50 mm/min)	4 %	ISO 527-2
Tensile Stress at Yield (50 mm/min)	18 MPa	ISO 527-2
Charpy Impact Strength, notched (0 °C)	75 kJ/m <sup>2</sup>	ISO 178/1eA
Charpy Impact Strength, notched (-20 °C)	65 kJ/m <sup>2</sup>	ISO 178/1eA
Hardness, Shore D	50	ISO 868

### Processing Techniques


The actual conditions will depend on the type of equipment used.

### Extrusion

Borcoat is a trademark of Borealis A/S, Denmark.

Borealis AG | Wagramerstrasse 17-19 | 1220 Vienna | Austria  
Telephone +43 1 224 00 0 | Fax +43 1 22 400 333  
FN 269858a | CCC Commercial Court of Vienna | Website [www.borealisgroup.com](http://www.borealisgroup.com)





# Polypropylene

## Borcoat EA165E

Cylinder	210 - 230 °C
Head	230 - 240 °C
Die	230 - 240 °C
Melt temperature	230 - 240 °C

Specific recommendations for processing conditions can be determined only when the application and type of equipment are known. Please contact your local Borealis representative for such particulars.

Borcoat EA165E can be applied by injection moulding.  
Specific recommendations for processing conditions can be determined only when the application and type of equipment are known.

### Storage

Borcoat EA165E should be stored in dry conditions at temperatures below 60°C and protected from UV-light. Improper storage can initiate degradation.


### Safety

The product is not classified as a dangerous preparation.

### Recycling

The product is suitable for recycling using modern methods of shredding and cleaning. In-house production waste should be kept clean to facilitate direct recycling.

Please see our Safety Data Sheet for details on various aspects of safety, recovery and disposal of the product, for more information contact your Borealis representative.



**Polypropylene**  
**Borcoat EA165E**

**Disclaimer**

**The product(s) mentioned herein are not intended to be used for medical, pharmaceutical or healthcare applications and we do not support their use for such applications.**

To the best of our knowledge, the information contained herein is accurate and reliable as of the date of publication, however we do not assume any liability whatsoever for the accuracy and completeness of such information.

**Borealis makes no warranties which extend beyond the description contained herein. Nothing herein shall constitute any warranty of merchantability or fitness for a particular purpose.**

**It is the customer's responsibility to inspect and test our products in order to satisfy itself as to the suitability of the products for the customer's particular purpose. The customer is responsible for the appropriate, safe and legal use, processing and handling of our products.**

No liability can be accepted in respect of the use of Borealis' products in conjunction with other materials. The information contained herein relates exclusively to our products when not used in conjunction with any third party materials.







